FBH Leibniz Ferdinand-Braun-Institut
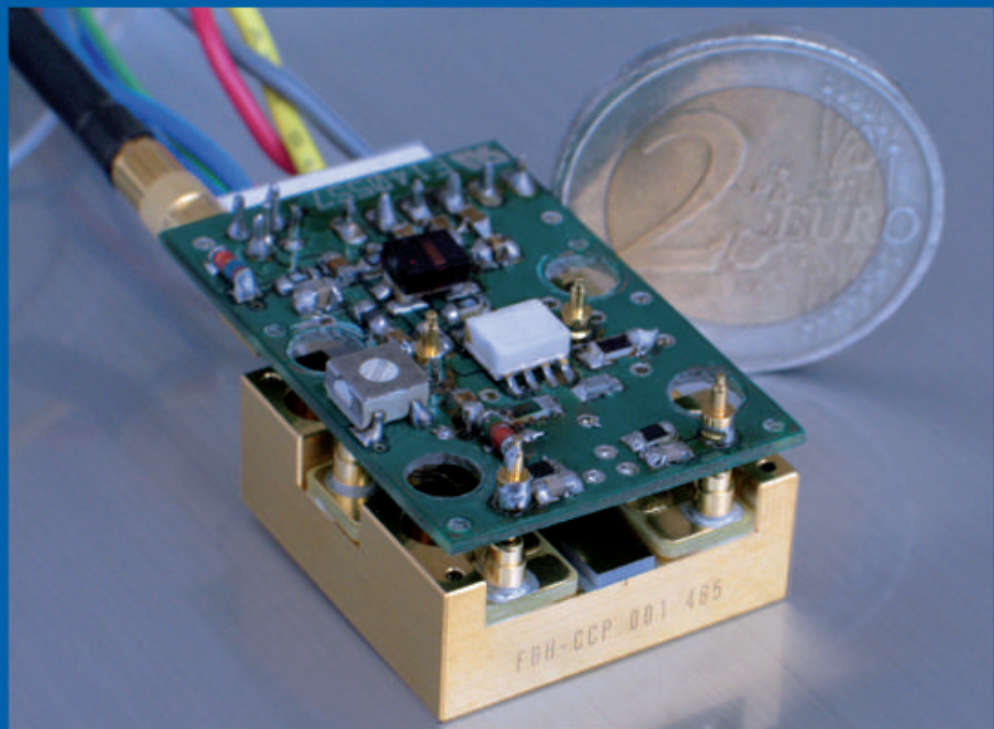
15

Innovationen mit Mikrowellen & Licht

Forschungsberichte aus dem Ferdinand-Braun-Institut Leibniz Institut für Höchstfrequenztechnik

Flexible Generation of Picosecond Laser Pulses in the Infrared and Green Spectral Range by Gain-Switching of Semiconductor Lasers

Sina Riecke

aus der Reihe:

Innovationen mit Mikrowellen und Licht

Forschungsberichte aus dem Ferdinand-Braun-Institut
Leibniz-Institut für Höchstfrequenztechnik

Band 15

Sina Riecke

Flexible Generation of Picosecond Laser Pulses in the Infrared and
Green Spectral Range by Gain-Switching of Semiconductor Lasers

Innovations with Microwaves and Light

Research Reports from the Ferdinand-Braun-Institut,
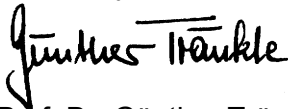**Leibniz-Institut für Höchstfrequenztechnik**

Preface of the Editors

Research-based ideas, developments and concepts are the foundation for progress and competitiveness, broadening the level of knowledge and technology as inventions. As innovative products and services a part of them eventually finds its way into daily routine.
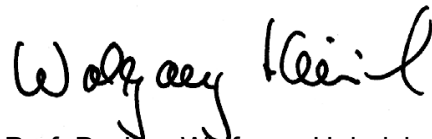
Accordingly, the *"Research Reports from the Ferdinand-Braun-Institut, Leibniz-Institut für Höchstfrequenztechnik"* series compile the institute's latest research and developments. We would like to make these results accessible and stimulate further discussions, not least to become as many developments as possible a part of our everyday life.

This report is on the generation of picosecond pulses with variable repetition rates which are particularly suitable for fluorescent lifetime spectroscopy, a technique used in bio-medical research. Therefore, an elaborate setup to generate laser pulses emitting in the green spectral region has been explored. Infrared lasers emitting near 1060 nm were manufactured and investigated at the FBH with respect to their gain-switching capabilities using drive electronics provided by the industrial partner PicoQuant. By means of second-harmonic generation, green optical pulses at a wavelength of 531 nm could be achieved with more than 5 W peak power. This result paves the way for industrial applications in bio-medical research.

We wish you an informative and inspiring reading

Prof. Dr. Günther Tränkle
Director

Prof. Dr.-Ing. Wolfgang Heinrich
Deputy Director

The Ferdinand-Braun-Institut

The Ferdinand-Braun-Institut researches electronic and optical components, modules and systems based on compound semiconductors. These devices are key enablers, that address the needs of today's society in fields like communications, energy, health and mobility. Specifically, FBH develops light sources from the visible to the ultra-violet spectral range: high-power diode lasers with excellent beam quality, UV light sources and hybrid laser systems. Applications range from medical technology, high-precision metrology and sensors to optical communications in space. In the field of microwaves, FBH develops high-efficiency multi-functional power amplifiers and millimeter wave frontends targeting energy-efficient mobile communications as well as car safety systems. In addition, compact atmospheric microwave plasma sources that operate with economic low-voltage drivers are fabricated for use in a variety of applications, such as the treatment of skin diseases.

The FBH is a competence center for III-V compound semiconductors and has a strong international reputation. FBH competence covers the full range of capabilities, from design to fabrication to device characterization.

In close cooperation with industry, its research results lead to cutting-edge products. The institute also successfully turns innovative product ideas into spin-off companies. Thus, working in strategic partnerships with industry, FBH assures Germany's technological excellence in microwave and optoelectronic research.

Flexible Generation of Picosecond Laser Pulses in the Infrared and Green Spectral Range by Gain-Switching of Semiconductor Lasers

vorgelegt von
Diplom-Physikerin
Sina Riecke
aus Nordenham

Von der Fakultät II – Mathematik und Naturwissenschaften
der Technischen Universität Berlin
zur Erlangung des akademischen Grades
Doktor der Naturwissenschaften
– Dr. rer. nat. –
genehmigte Dissertation

Promotionsausschuss:

Vorsitzender:	Prof. Dr. Andreas Knorr, TU Berlin
Berichter:	Prof. Dr. Michael Kneissl, TU Berlin
	Prof. Dr. Gerald Kell, Hochschule Brandenburg
	Prof. Dr. Günther Tränkle, TU Berlin

Tag der wissenschaftlichen Aussprache: 6. 1. 2011

Berlin, 2011
D 83

Abstract

The objective of this thesis is the development of a reliable and intense green picosecond laser source for fluorescence lifetime spectroscopy. This versatile method from the life sciences requires excitation laser pulses with a duration of less than 200 ps and a pulse energy of around 100 pJ. In order to adjust the pulse interval to the fluorescence lifetime or for interleaving of excitation pulses at different wavelengths, pulses are required on-demand and at variable repetition rates in the megahertz range.

In the red and blue spectral range, such pulses can be readily generated by gain switching of single ridge-waveguide laser diodes. Green excitation sources are equally required, but directly green emitting laser diodes so far exist only as laboratory samples with limited lifetime. Therefore, second harmonic generation (SHG) is the method of choice for the generation of green picosecond pulses. As the fundamental beam, this requires spectrally narrow infrared laser pulses with a peak power of several watts.

This thesis consists of three parts. The first part studies the generation of spectrally narrow picosecond pulses by gain switching of distributed-feedback (DFB) laser diodes. The second part treats the amplification of these laser pulses, while the third part is concerned with the generation of green picosecond pulses using SHG.

As a first step toward the development of a compact and flexible green pulse source, the gain switching behavior of infrared ridge-waveguide distributed-feedback laser diodes is studied. When tuning the wavelength of the gain maximum by changing the device temperature, the same laser shows qualitatively different dynamic spectral behavior. If the Bragg wavelength is longer than the wavelength of the gain maximum, laser emission begins with a broad multimode spectrum during the first relaxation oscillation. An increase of the device temperature improves the overlap of the Bragg wavelength and the gain spectrum and allows the generation of spectrally narrow picosecond pulses which are excellently suited for SHG.

A temperature- and wavelength-dependent rate-equation model for the mode-competition in DFB lasers is developed which achieves excellent agreement with these observations. A systematic optimization of laser diode design parameters shows that the generation of spectrally narrow high-power picosecond pulses requires a trade-off regarding the coupling coefficient: While a dynamic single-mode spectrum needs a high DFB coupling coefficient, this leads to reduced out-coupling and in turn to a lower pulse peak power. Close to the optimum, pulses with a peak power above 1 W and more than 95% of the pulse energy emitted at the Bragg wavelength are generated.

Several technologies for the amplification of these pulses to peak powers above 15 W are studied. Semiconductor amplifiers show the highest potential for miniaturization, and due to their short upper-state lifetime of approximately 1 ns, their gain is independent of the seed pulse repetition rate. In contrast, Ytterbium-doped fiber amplifiers are scalable to higher total powers but typically show a repetition-rate dependent gain.

Two concepts of miniaturization are compared, a hybrid integrated semiconductor master-oscillator power amplifier (MOPA) and a monolithic semiconductor MOPA for the generation of picosecond pulses, both with a footprint of less than $5 \times 25 \, mm^2$. Compared to continuous wave operation, the suppression of parasitic amplifier lasing is critical in these devices.

Using the semiconductor MOPAs as the fundamental source, the second harmonic generation of green picosecond pulses is studied. Both with a bench-top and a monolithic fundamental source, pulse energies above 250 pJ at 531 nm have been obtained. Due to pulse shaping both during amplification and during SHG, the green pulse shape is nearly independent of the seed input signal. The deconvoluted peak power of 10 W exceeds previous realizations by more than an order of magnitude. The high pulse energy combined with their excellent extinction ratio makes these pulses ideally suited for fluorescence lifetime spectroscopy.

Zusammenfassung

Die Zielstellung dieser Doktorarbeit besteht in der Entwicklung einer zuverlässigen und intensiven grünen Pikosekunden-Laserquelle für die Fluoreszenz-Lebensdauer-Spektroskopie. Diese vielseitige Messmethode aus den Lebenswissenschaften benötigt zur Anregung Laserpulse mit einer Länge von unter 200 ps und einer Pulsenergie um 100 pJ. Um die Pulsintervalle an die Fluoreszenz-Lebensdauer anzupassen oder abwechselnd Anregungspulse bei verschiedenen Wellenlängen zu verwenden, müssen diese auf ein Auslösungssignal hin kontrolliert erzeugt werden. Typische Wiederholraten sind im Megahertz-Bereich.

Im roten und blauen Spektralbereich können solche Pulse leicht durch die Gewinnschaltung einzelner Rippenwellenleiter-Laserdioden erzeugt werden. Grüne Anregungspulse werden ebenso benötigt, aber direkt grün emittierende Laserdioden existieren bislang nur als Labormuster mit begrenzter Lebensdauer. Daher ist Frequenzverdopplung (*second harmonic generation*, SHG) die Methode der Wahl für die Erzeugung grüner Pikosekundenpulse. Als fundamentalen Strahl benötigt man dafür infrarote Laserpulse mit einer Spitzenleistung von einigen Watt.

Die vorliegende Doktorarbeit gliedert sich in drei Teile. Der erste Teil befasst sich mit der Erzeugung von spektral schmalbandigen Pikosekundenpulsen durch die Gewinnschaltung von Laserdioden mit verteilter Rückkopplung (*distributed feedback*, DFB). Im zweiten Teil werden diese Laserpulse optisch verstärkt, der dritte Teil behandelt die Erzeugung von grünen Pikosekundenpulsen durch SHG.

Als ersten Schritt der Entwicklung einer kompakten und flexiblen grünen Pulsquelle wird die Gewinnschaltung von infraroten DFB Laserdioden mit Rippenwellenleiter untersucht. Wenn der Laser erwärmt wird, ändert sich die Wellenlänge des Gewinnmaximums und es zeigen sich qualitative Unterschiede in der spektralen Dynamik des selben Lasers. Wenn die Bragg-Wellenlänge länger ist als die Wellenlänge des Gewinnmaximums, beginnt die Laser-Emission während des ersten Relaxationspulses spektral breitbandig. Eine Erhöhung der Temperatur verbessert den Überlapp zwischen der Bragg-Wellenlänge und dem Gewinn-Spektrum und ermöglicht die Erzeugung spektral schmalbandiger Pikosekunden-Pulse, die hervorragend für die Frequenzverdopplung geeignet sind.

Ein temperatur- und wellenlängenabhängiges Ratengleichungs-Modell für den Modenwettbewerb in DFB-Lasern wird entwickelt, das eine hervorragende Übereinstimmung mit diesen Beobachtungen erreicht. Eine systematische Optimierung des Laserdioden-Designs zeigt, dass die Erzeugung spektral schmalbandiger Pikosekundenpulse mit hoher Spitzenleistung einen Kompro-

miss erfordert: Während ein hoher DFB-Koppelkoeffizient nötig ist, um ein dynamisch einmodiges Spektrum zu gewährleisten, führt er gleichzeitig zu verminderter Auskopplung und damit zu einer geringeren Pulsspitzenleistung. Nahe am Optimum werden Pulse mit einer Spitzenleistung von über $1\,\text{W}$ erzeugt, die mehr als 95% der Energie in der Bragg-Mode abstrahlen.

Verschiedene Technologien zur Verstärkung dieser Pulse auf Spitzenleistungen über $15\,\text{W}$ werden untersucht. Optische Halbleiterverstärker haben das höchste Potential für die Miniaturisierung und ihr Gewinn ist unabhängig von der Signal-Wiederholrate, da sie eine sehr geringe Inversionslebensdauer von ca. $1\,\text{ns}$ haben. Im Gegensatz dazu sind Ytterbium-dotierte Faserverstärker zu höheren Leistungen skalierbar, aber ihr Gewinn hängt von der Signal-Wiederholrate ab.

Zwei Konzepte zur Miniaturisierung des Laser-Verstärker-Systems (*master oscillator-power amplifier*, MOPA) werden untersucht, ein hybrid integrierter und ein monolithischer MOPA für die Erzeugung von Pikosekundenpulsen. Beide haben eine Grundfläche von weniger als $5 \times 25\,\text{mm}^2$. Verglichen mit dem Dauerstrichbetrieb ist die Unterdrückung von parasitärem Lasen des Verstärkers bei diesen Bauteilen entscheidend.

Ausgehend von den Halbleiter-MOPAs als Fundamentalquelle wurde die Erzeugung von grünen Pikosekundenpulsen durch Frequenzverdopplung untersucht. Sowohl mit einem Laboraufbau auf einem optischen Tisch, als auch mit einem monolithischen MOPA wurden Pulsenergien über $250\,\text{pJ}$ bei $531\,\text{nm}$ erreicht. Durch Verbesserungen der Pulsform bei der Verstärkung und der Frequenzverdopplung ist die grüne Pulsform fast unabhängig vom Eingangssignal des Verstärkers. Die entfaltete Spitzenleistung von $10\,\text{W}$ übertrifft vorherige Ergebnisse um mehr als eine Größenordnung. Durch ihre hohe Energie und ihr exzellentes Auslöschungsverhältnis sind diese Pulse hervorragend für die Fluoreszenzspektroskopie geeignet.

Acknowledgments

First of all, I would like to express my sincere gratitude to my supervisor, Professor Dr. Michael Kneissl, for his constant support and many valuable discussions that helped me to structure my work and appreciate which points warranted further inquiry.

I am sincerely grateful to Professor Dr. Gerald Kell and Professor Dr. Günther Tränkle for agreeing to act as referees for my thesis.

Professor Tränkle is the director of Ferdinand-Braun-Institut, Leibniz Institut für Höchstfrequenztechnik, where I carried out the experimental part of my thesis work. I wish to express my deep gratitude to him for giving me the chance to be a visiting scientist at his institute and carry out my dissertation in a cooperation project with PicoQuant GmbH. Moreover, I am very grateful for his support and encouragement. He graciously shared with me many ideas and insights which helped me in important points of this thesis.

I owe my sincere thanks to Rainer Erdmann, CEO of PicoQuant GmbH, for giving me the opportunity to work at his company in a joint project with Ferdinand-Braun-Institut. This experience is exceedingly valuable to me because it allowed me to keep my thesis work relevant to a wider audience and to gain insight in the processes and requirements of industrial research and development. In particular, I would like to thank Mr. Erdmann for his flexibility and accommodation regarding my work schedule.

My warm and sincere gratitude is due to Dr. Katrin Paschke of Ferdinand-Braun-Institut, whose constant availability to provide advice and support made this thesis possible. Her cheerful attitude and excellent technical insight shape the atmosphere of productivity and teamwork in the group "Hybride Diodenlaser-Systeme".

I would like to express my sincere thanks to Kristian Lauritsen, head of laser development at PicoQuant GmbH, for his prompt technical advice and support, particularly in questions of electronics. Without his support in the design and customization of the electrical pump drivers, my gain switching experiments would not have been possible.

I am deeply grateful to Dr. Götz Erbert, head of the optoelectronics department at Ferdinand-Braun-Institut for many technical discussions in which he shared with me his exceptional knowledge of diode lasers and his remarkable detail memory of past results obtained in his department.

I owe my sincere thanks to Dr. Hans Wenzel of Ferdinand-Braun-Institut, whose help with laser diode simulations and with choosing the devices for my experiments has been vital to this work.

I warmly thank my colleagues at Ferdinand-Braun-Institut, from whom I have learned many aspects of experimental measurement and analysis. I am

Contents

Chapter 1

Introduction

When Theodore Maiman demonstrated the first laser in 1960 [1], the device was famously called "a solution looking for a problem" by his assistant Irnee D'Haenens. Since then, lasers have been developed at a multitude of wavelengths and power levels, and plenty of applications have been found, each requiring specific laser parameters. Often, the improvements of laser sources and applications have gone hand in hand, and the development of tailored light sources is an important direction of industrial and academic research even today.

The requirements of different applications vary greatly. Material processing, for example, demands high power density at low thermal load – this is typically realized via pulsed laser sources with a peak power of at least several kilowatts and a low duty cycle. A high beam quality is required in order to achieve a tight focus on the work piece [2]. Telecommunications, on the other hand, works with low average powers in the milliwatt range, but the transmission of ever increasing data rates requires lasers with stable and narrow wavelength spectra and very high modulation frequencies [3]. Another important application of lasers is in analysis and sensing. This encompasses a variety of methods, such as evanescent sensing of trace gasses [4] or the measurement of velocities, for example in road traffic [5].

The goal of this thesis is in the development of a pulsed laser source for time-domain fluorescence lifetime spectroscopy [6, 7]. In this method, a picosecond pulsed laser is used to excite fluorescence in biological samples. In combination with a fast and sensitive single photon counting system, this allows the measurement of the fluorescence decay lifetime, which is on the order of a few nanoseconds. For many fluorophores, this lifetime depends on properties of the molecule's environment, such as pH-value or Na^{2+} concentration [8]. In general, fluorescence lifetime spectroscopy allows the real-time monitoring of biological processes in living cells.

In order to add spatial resolution, the excitation light is often directed onto the sample through a confocal microscope, which at the same time is used to
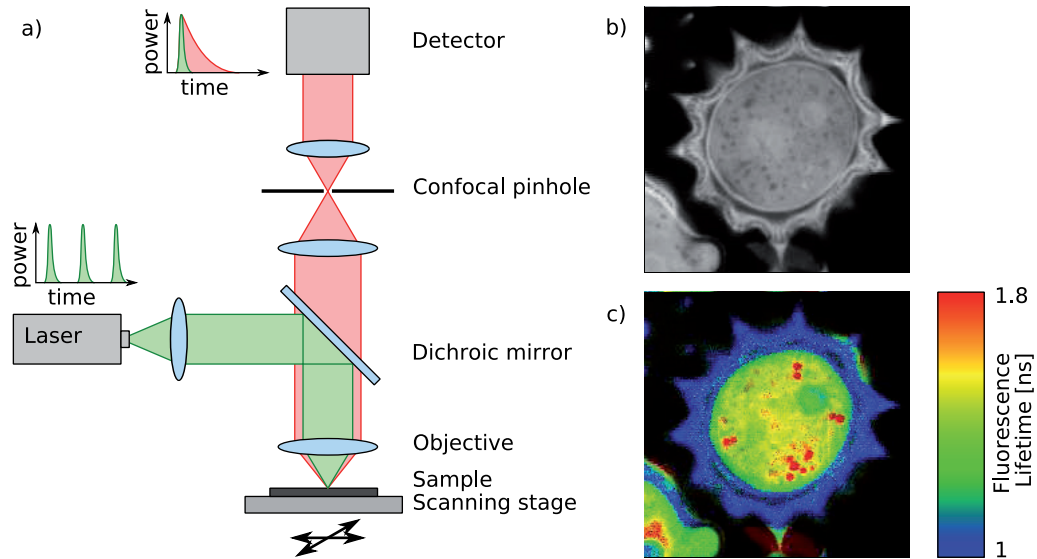
Figure 1.1: a) Confocal fluorescence microscope setup. b) Fluorescence intensity image and c) fluorescence lifetime image of a daisy pollen. The chloroplasts are visible only in the lifetime image (red) but not in the intensity image. Fluorescence images courtesy of PicoQuant GmbH.

collect the fluorescence signal (Fig. 1.1 a). A two-dimensional fluorescence lifetime image can be generated by scanning the probe relative to the beam. Compared to light microscopy or fluorescence intensity microscopy using continuous excitation, fluorescence lifetime imaging microscopy (FLIM) offers enhanced image contrast and the possibility to directly measure biological parameters [6] (Fig. 1.1 b and c).

A related method, Förster resonant energy transfer (FRET) involves energy transfer between two fluorophores. This enables the measurement of distances between single molecules on the nanometer scale, and thus allows the monitoring of molecular interactions [9]. It has been applied, for example, in order to determine the molecular mechanism of muscle contraction [10].

For optimum fluorescence lifetime measurements, the excitation pulse length has to be much shorter than the fluorescence decay time, typically below 200 ps, while the pulse intervals have to be much larger. In order to adjust the repetition rate to different lifetimes and to avoid damaging the sample by excessive illumination, variable excitation pulse repetition rates in the megahertz range are preferred [7]. For advanced methods, like pulse-interleaved excitation [11], freely triggerable excitation pulses are needed. Required pulse energies are between 20 and 100 pJ.

Since the fluorescence has to be detected in the intervals between the excitation pulses, a high extinction ratio of typically above 40 dB is required in order to remain below the dark count rate of the detector.

Laser pulses meeting these specifications can be readily provided in the red and blue spectral range using single gain switched laser diodes [12]. However, so far, no systematic study of the parameter-dependence of the gain switching behavior exists, especially for narrow-linewidth laser diodes. Furthermore, the generation of green picosecond pulses requires a more complex setup, including the frequency-doubling of a gain switched infrared laser diode.

In this thesis, the gain switching behavior of single distributed feedback lasers is studied and the laser diode design is optimized for the generation of particularly intense narrow-band picosecond pulses. In a second step, these will be optically amplified and converted into the green spectral range. Different technologies and miniaturized setups are evaluated. The peak power of the resulting green picosecond pulses surpasses that of previous realizations with flexible repetition rate by an order of magnitude.

Chapter 2

Gain-Switching of Distributed Feedback Laser Diodes

2.1 Distributed Feedback Lasers

In comparison to other lasers, diode lasers are distinguished by their compact size, high efficiency, and robustness. They can be economically mass-produced and are maintenance-free. Therefore, laser diodes are ubiquitous in modern information technology, for example in optical drives and optical data transmission. Increasingly, they also find application where higher output powers are required, for instance in material processing or as pump sources for solid-state lasers.

Lasers with narrow and stable emission spectra are utilized in fields as diverse as spectroscopy, atom cooling, telecommunications and nonlinear wavelength conversion. In Raman spectroscopy, for example, a narrow-linewidth laser is needed in order to distinguish the weak Raman signal from the scattered excitation light [13]. In telecommunications, wavelength division multiplexing and wavelength conversion require narrow-band signals [14].

This section gives an introduction into the function and processing of laser diodes with a focus on lasers with integrated optical gratings for emission at a single longitudinal mode.

2.1.1 Fundamentals of Laser Diodes

2.1.1.1 Optical Gain in Semiconductor Structures

Since the demonstration of the first laser diode consisting of a p-n monojunction in 1962 [15], semiconductor optoelectronics has advanced enormously. The first laser diodes had very low efficiency and were limited to pulsed operation at cryogenic temperatures due to heat dissipation problems. Today, modern quantum well diode lasers have the smallest size (only a few cubic
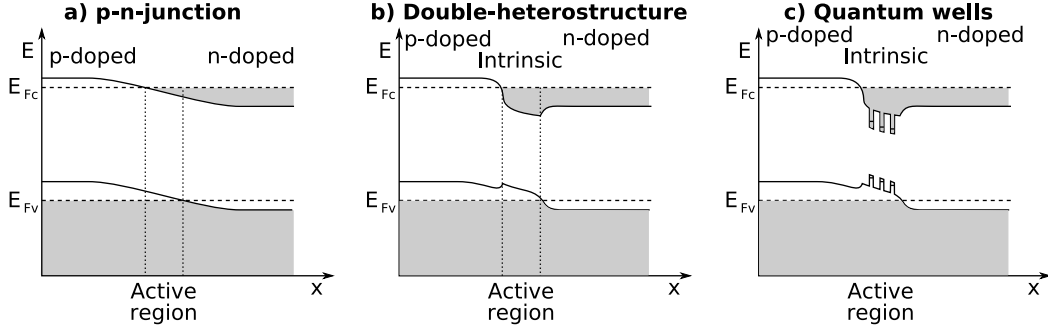
Figure 2.1: Electron energy and occupation in the active zone of a laser diode. a) p-n-monojunction, b) double-heterostructure, c) triple quantum well layout

millimeters including housing), highest efficiency (above 50%), and longest lifetime of all lasers.

In a semiconductor laser, optical gain is generated by recombination of electrons in the conduction band with holes in the valence band. Therefore, all laser diodes consist of direct bandgap semiconductors, in order to enable efficient recombination. Positive gain develops in an *active region*, where there is a large occupation probability for both the electrons in the conduction band and the holes in the valence band.

In the simplest case of a p-n monojunction, this inversion condition is fulfilled at high forward bias (Fig. 2.1a). While across an unbiased p-n junction, the Fermi energy E_F is constant, a forward bias reduces the band bending and causes the Fermi level to split up into different *quasi-Fermi levels E_{Fc}* and E_{Fv} for the conduction and valence bands [16]. When the bias voltage approximately equals the inbuilt voltage, the depletion zone disappears and an inversion region forms, where both electrons and holes are majority carriers [17].

A drastic improvement in semiconductor laser performance was achieved with the introduction of the *double heterostructure* [17, 18] (Fig. 2.1b). It enables higher electron and hole densities and therefore higher recombination efficiencies. In a double-heterostructure laser, an intrinsic material with lower bandgap is inserted between the p- and n-doped regions.

A further increase in laser efficiency and output power can be achieved using an active region containing a *quantum well (QW)* structure [19] (Fig. 2.1c). Here, the layers of the low-bandgap material are so thin that the momentum of electrons and holes becomes quantized in the direction perpendicular to the quantum well layer. The required layer thickness for this charge carrier confinement is typically between 5 and 20 nm. Such thin layers can be grown with considerable lattice mismatch, extending the feasible wavelength range.
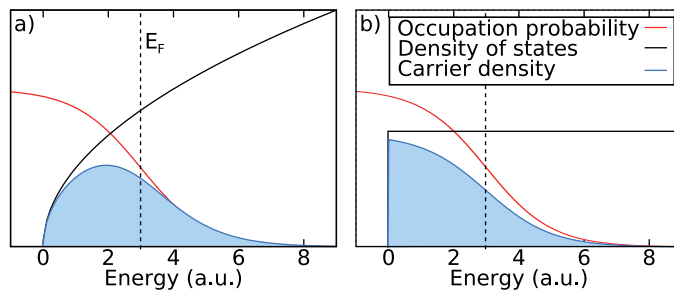
Figure 2.2: Density of states, occupation probability, and resulting carrier density in the conduction band for a) a bulk semiconductor and b) a quantum well. All energies are normalized to the band-gap energy.

The strain introduced by the lattice mismatch is also used as an engineering parameter to further improve the laser performance [20–22].

The momentum quantization in a QW qualitatively changes the density of states compared to a bulk semiconductor device [22,23] (Fig. 2.2). While in a bulk device, the density of states shows a square-root dependence on energy, it is constant for a quantum well, as long as only the lowest energy level is occupied. The optical gain g is proportional to the product of the density of states ρ and the inversion probability [24]

$$g \sim \rho \left\{ f_e(E)\, f_h(E) - \left(1 - f_e(E) \right)\left(1 - f_h(E) \right) \right\},$$

where f_e and f_h are the Fermi functions for electrons and holes, respectively. Therefore, the density of states directly influences the gain spectrum. Quantum well lasers achieve a higher peak gain with reduced sensitivity on temperature than bulk diode lasers. The quantum well gain, however, increases only logarithmically with the carrier density, while in bulk devices, that dependence is linear [24].

2.1.1.2 Optical Confinement and Resonator Design

In the framework of complex electrical field amplitudes, refractive index and gain can be understood as the real and imaginary parts of the electrical permittivity, respectively. According to the Kramers-Kronig relation, the refractive index of a semiconductor thus depends on the carrier density [22, 25]. Therefore, in a laser diode, the refractive index is locally increased in the active zone. This *gain guiding* [18,26] naturally leads to optical confinement. However, due to the narrow active zone, the guided mode necessarily has a small mode area. The resulting high power densities limit the achievable output power before material damage occurs.
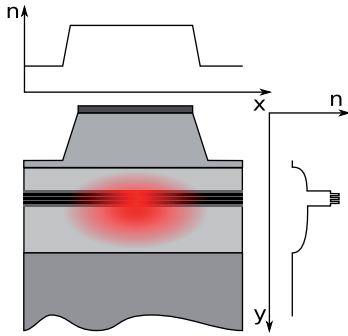
Figure 2.3: View of a QW laser diode along the optical axis. In vertical direction, optical confinement is provided by a graded index separate confinement heterostructure (GRINSCH), in lateral direction, a ridge waveguide is implemented

In order to spread out the optical field while keeping the carriers confined to a narrow structure, a *separate confinement heterostructure (SCH)* [18, 26] (Fig. 2.3) can be formed by high-refractive index layers surrounding the active zone. This method is called *index guiding* and is particularly useful in quantum well lasers with their narrow active region.

In the lateral direction, both gain and index guiding are utilized in modern lasers. In broad-area [26] and tapered lasers [27], gain guiding dominates and the lateral dimension of the laser diode is defined by the shape of the metal pump contact.

For a waveguide with only a single lateral mode, the lateral width must not exceed a few micrometers. Due to current spreading, this cannot be achieved with gain guiding alone and a further index contrast is required. It is usually implemented via a *ridge waveguide (RW)* [18, 28] (Fig. 2.3). Even though the ridge trenches typically do not cut into the vertical waveguide, they influence the evanescent waves. The presence or absence of semiconductor material above the waveguide therefore alters the effective refractive index inside the waveguide, leading to lateral confinement.

Laser action requires not only a good overlap of the optical mode and the gain medium but also optical feedback. In a monolithic laser diode, sufficient reflectivity ($R \approx 30\%$) can be provided by the cleaved facets of the semiconductor device. In modern high-power laser diodes, however, the facet reflectivities are typically optimized using dielectric coatings with a high reflectivity at the rear facet and a low reflectivity (down to 1%) at the front facet. Furthermore, the facets are passivated to protect them from optical damage and degradation [26, 29]. This setup with two plane parallel resonator mirrors is called a *Fabry-Pérot (FP) resonator* [18].

2.1.2 Bragg Gratings for Spectral Selectivity

The mirrors of a Fabry-Pérot cavity typically have a constant reflectivity over a fairly wide spectral range. Combined with the broad gain spectrum
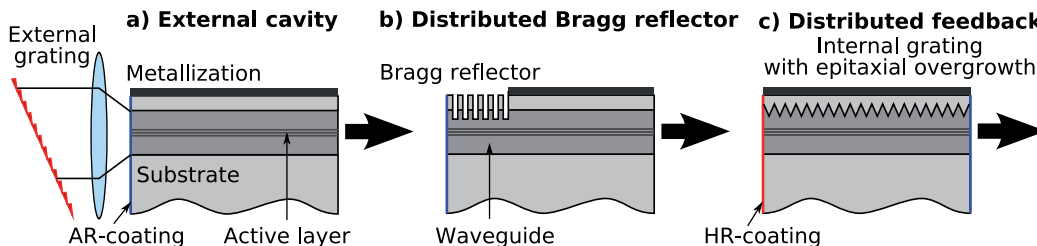
Figure 2.4: Schematic layout of a) an external cavity laser, b) a distributed Bragg-reflector (DBR) laser and c) a distributed feedback (DFB) laser viewed from the lateral direction.

of a diode laser [24], this leads to very similar lasing thresholds for multiple longitudinal resonator modes. This compromises the spectral quality: In high power devices, gain inhomogeneities can lead to multimode lasing [28]. Even at low output power, mode jumps appear when the pump current is ramped up [18,30]. In order to select a single longitudinal mode, cavity losses have to be made wavelength sensitive. This is typically implemented via an optical grating providing wavelength-selective feedback according to the Bragg condition [31,32].

Using a generic diode laser, a grating can be introduced as an external cavity mirror, for example in the *Littrow configuration* [33] (Fig. 2.4a). Such a setup can even be wavelength-tunable when the grating is rotated. If fiber-coupled output is desired, a fiber Bragg grating can be used for frequency stabilization without extra effort [34]. However, external cavity lasers require high mechanical stability and have a longer resonator than monolithic devices. This is problematic for the generation of short narrow-band pulses, since the grating can only act on the spectrum over multiple resonator roundtrips. For example, if the cavity has a length of 2 cm, the roundtrip time is more than 100 ps. If shorter pulses are generated in such a cavity, their spectrum cannot be influenced by the grating, and they will be spectrally broad.

However, wavelength stabilization of short pulses with an external grating is possible when the repetition rate is fixed to the cavity roundtrip time and subsequent pulses overlap in the gain medium [35].

In order to avoid these disadvantages, Bragg gratings can be monolithically integrated into edge-emitting laser diodes. In a *distributed Bragg-reflector (DBR)* [36–38] laser, the grating is separate from the gain section and acts as a passive resonator mirror (Fig: 2.4b). Therefore, the grating section does not require an electrical contact for pumping. This enables the implementation of the grating by surface etching, in the same process step as the etching of the ridge waveguide. Since the index contrast between air and semiconductor
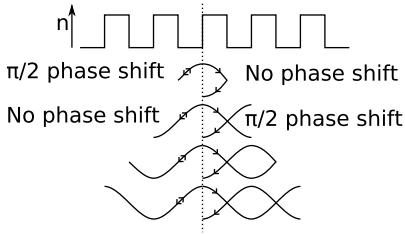
Figure 2.5: Starting from an arbitrary point in the center of a DFB laser (dotted vertical line), reflections from the left-hand half and the right-hand half of the grating destructively interfere at the Bragg wavelength. This leads to the formation of a spectral stopband.

is high, relatively short gratings provide a high reflectivity [36, 37]. With *i*-line stepper lithography, a minimum feature size of 480 nm can be achieved. At a lasing wavelength around 1060 nm, only gratings of order five or higher can be implemented. At such high grating orders, etch depth and duty cycle have to be fabricated to a very high precision in order to achieve a high total reflectivity [36, 38]. The maximum reflectivity of a distributed Bragg reflector is located at the *Bragg wavelength* λ_B [39].

On the other hand, in a *distributed feedback (DFB)* laser, the Bragg grating covers the whole resonator length and consequently needs to be electrically pumped (Fig. 2.4c). Therefore, the Bragg grating is typically buried in-between epitaxy layers or placed on the side of the ridge waveguide. Since both cavity mirrors are formed by the same Bragg grating, the counter-propagating waves interfere destructively exactly at the Bragg wavelength, and the reflectivity is at a minimum [40] (Fig. 2.5). This spectral feature is called the *stopband* of the DFB laser, and the highest reflectivity is found at adjacent wavelengths.

The precise wavelength dependence of the reflectivity is sensitively affected by the facet reflectivities R_L and R_R and the grating phases φ_L and φ_R at the facets. If the facets are perfectly anti-reflecting, the two modes on either side of the stopband experience the same reflectivity, compromising the spectral selectivity of the laser. However, in real devices, R_L and R_R are finite, and the back facet typically is highly reflective. The shape of the stop band then mainly depends on the grating phase φ_R at the back facet, and generally, one preferred mode develops [41–43] (Fig. 2.6).

The occurrence of a stopband and the associated equal modes can be avoided altogether if a defect is introduced into the Bragg grating at the center of the laser resonator. The most common such layout is the *quarter wave shifted grating* [40, 43, 44]. It selects a single mode independent of the grating phases at the facets, but fabrication is much more complicated and time-consuming than for a homogeneous Bragg grating. While the latter can be written holographically [45], quarter-wave-shifted gratings are typically written with an electron beam, which has a low throughput volume.
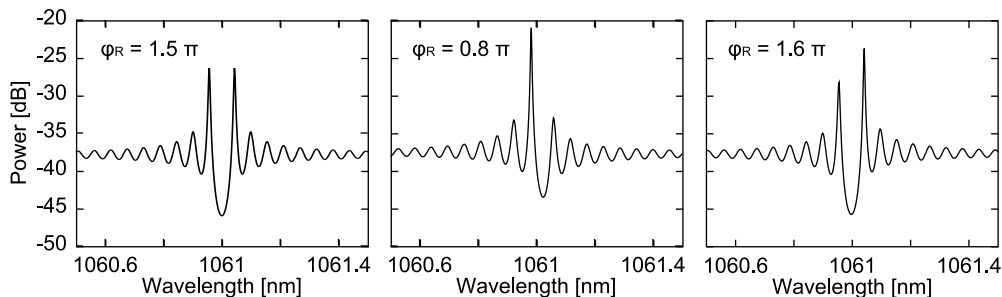
Figure 2.6: Simulated DFB laser spectra below threshold including spectral stop-bands for $R_L = 0$, $R_R = 0.95$, $\varphi_L = 0$. For $\varphi_R = 1.5\,\pi$, the modes on either side of the stopband have equal intensity. For all other values of φ_R, one mode is preferred.

Another engineering parameter is the *grating order q*, defined as

$$\frac{q}{2}\frac{\lambda_B}{n} = \Lambda,$$

where Λ is the grating period and n the effective refractive index. Higher-order gratings can reach reflectivities similar to first-order gratings and are easier to manufacture due to their longer grating period. However, higher-order gratings introduce a coupling between guided modes and radiation modes which leads to radiative photon loss (Sec. 2.3.1.1). The strength of this loss increases with the grating coupling constant κ.

2.1.3 Device Layout and Processing

The DFB lasers discussed in this thesis were grown by metal-organic vapor phase epitaxy (MOVPE) [46–48] on a precisely aligned GaAs (100) substrate. The active region consists of three compressively strained InGaAs quantum wells (QWs) embedded in a 3.6 μm thick super-large optical cavity waveguide [47] consisting of AlGaAs.

First, a buffer layer of GaAs is grown on the bare wafer. This is followed by an AlGaAs cladding layer and the 1800 nm thick AlGaAs n-waveguide with a graded refractive index (GRIN) profile. The InGaAs quantum wells are separated by GaAsP barriers and covered by the first part of the p-waveguide, consisting of 600 nm of AlGaAs [49] (Fig. 2.7.1).

Due to the high affinity of aluminum to oxygen, an aluminum containing surface exposed to air can hardly be overgrown in a conventional MOVPE reactor [42]. Therefore, the Bragg grating is formed in an aluminum-free InGaP – GaAs – InGaP layer sequence. The second-order grating with a

1) 1st epitaxy: waveguide and active zone

2) Application and exposure of photoresist

3) Development of photoresist, etching of Bragg grating

4) 2nd epitaxy: upper cladding and contact layer

5) Application and patterning of photoresist

6) Etching of ridge waveguide

7) Application and patterning of insulator

8) Metalization

9) Cleaving of laser bars, facet coating
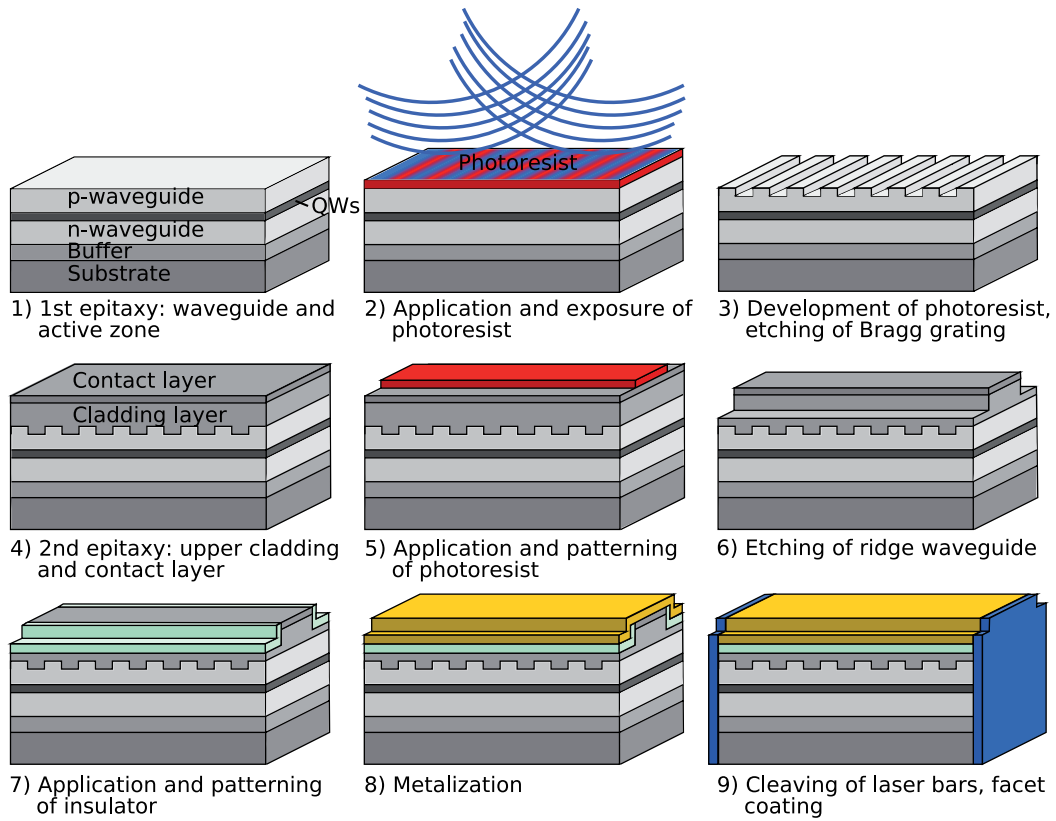
Figure 2.7: Schematic of processing steps of a DFB laser.
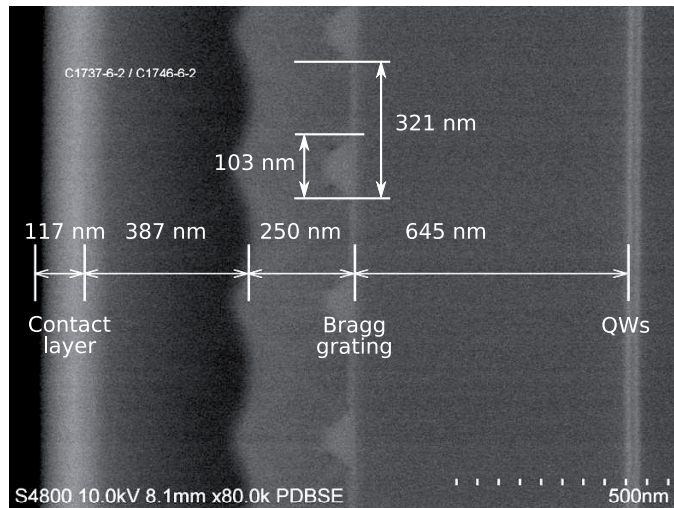
Figure 2.8: Scanning electron microscopy image of a second-order DFB Bragg grating for 1060 nm

period of approximately 330 nm is formed by holographic photolithography in the Lloyd setup [45, 47] and wet-chemical etching [50, 51] (Fig. 2.7.2–3 and 2.8). Due to the three different epitaxial layers, a three-step etching-process is required.

In a second epitaxy step, the remainder of the AlGaAs p-waveguide as well as the cladding and contact layers are grown (Fig. 2.7.4).

Since the Bragg grating is located in the p-waveguide well away from the quantum wells, *index coupling* is realized. The grating introduces a variation of the real refractive index only, with only weak modulation of gain or loss.

Lateral optical confinement is provided by a 2.2 μm wide ridge-waveguide (RW) fabricated by reactive ion etching (RIE) [36, 52] (Fig. 2.7.5–6). In order to restrict current flow to the ridge-waveguide, the wafer is covered in insulating SiN, which is selectively removed on the top of the RW by RIE (Fig. 2.7.7). Subsequently, a Ti/Pt/Au layer is applied as the p-electrode, covered by a thick gold layer (Fig. 2.7.8). Finally, the wafer is thinned and the n-electrode (Ni/Ge/Au) and a reinforcement layer (Ti/Pt/Au) are applied to the back side.

The lasers were cleaved to a cavity length of 1.5 mm. The front and rear facets were passivated with ZnSe and coated for zero and high reflectivity, respectively [26, 29].

2.1.4 Continuous-Wave Characteristics

In continuous-wave (CW) operation, DFB RW lasers show excellent performance regarding narrow linewidth, good beam quality, and high output power. A linewidth of 3.6 kHz at 55 mW has been reported with a corrugation-pitch modulated DFB laser [53]. With a homogeneous DFB laser, an intrinsic linewidth of 22 kHz at 150 mW was measured [54].

An output power of 970 mW has been reached with a 3 mm long device at 980 nm, with kink-free power-current (PI) characteristics up to 700 mW [55]. The beam quality [56] typically is nearly diffraction limited with $M^2 < 1.5$ (second moments) in both lateral and vertical direction [57].

In this work, PI-characteristics were measured with a Ulbricht integrating sphere and a Newport 818-SL Silicon photodetector. The accuracy is approximately ±10%, precision is higher at ±3%. Wavelength spectra were measured with an Advantest Q8384 spectrometer with a resolution of 10 pm.

The DFB single emitters investigated in this thesis have been manufactured at Ferdinand-Braun Institute on wafers C1336-6-3 and C1340-6-3. For both laser types, example PI-characteristics and CW spectra are shown in Fig. 2.9. The laser types mainly differ in the Bragg coupling coefficient κ, with $\kappa \approx$ 0.9 cm^{-1} for wafer C1336-6-3 and $\kappa \approx 2.2$ cm^{-1} for wafer C1340-6-3. Since the
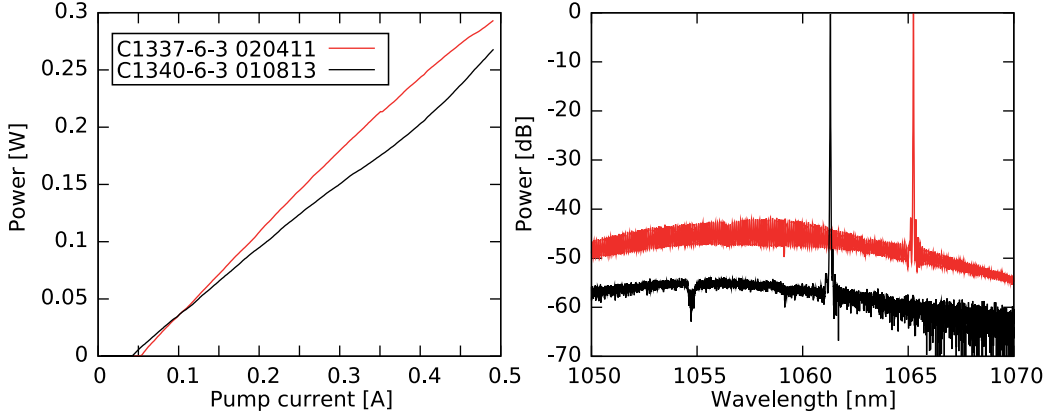
Figure 2.9: Example CW PI-characteristics and spectra of the lasers used in this work. T=25°C, spectra at I =100 mA

Wafer	C1336-6-3	C1340-6-3			C1336-6-3	C1340-6-3
Geometry				Reflectivities		
Length		1.5 mm		R_{L}		10^{-4}
RW width		2.2 µm		R_{R}		0.95
Quantum wells		3		κ	0.9 cm^{-1}	2.2 cm^{-1}
Thickness		8 nm each		λ_B	1065.05 nm	1060.99 nm
Vert. waveguide		2.4 µm				
Gain and Loss				CW Characteristics		
Modal gain	830 cm^{-1}	700 cm^{-1}		I_{th}	53.2 mA	44.7 mA
Internal loss	11 cm^{-1}	13 cm^{-1}		m	0.77 W/A	0.61 W/A

Table 2.1: Parameters of DFB single emitters at 330 K and threshold carrier density

gratings are of second order, a higher coupling also introduces higher radiative losses. This explains the observed PI-characteristics: At 300 K, lasers from wafer C1336-6-3 have a higher threshold current ($I_{\mathrm{th}} = (53.2 \pm 1.6)$ mA) and a higher slope ($m = (0.77 \pm 0.02)$ W/A) than lasers from wafer C1340-6-3 ($I_{\mathrm{th}} = (44.7 \pm 1.5)$ mA, $m = (0.61 \pm 0.04)$ W/A). All measurements were averaged over at least four devices.

Lasers from both wafers show a clean single-mode spectrum in CW operation with a side-mode suppression ratio (SMSR) greater than 40 dB. In the spectrum of laser C1336-6-3 020411, the residual Fabry-Pérot modes are visible in the spectral background. These are more strongly suppressed in lasers from wafer C1340-6-3 due to the stronger grating reflectivity. For an overview

of the CW properties at 300 K and design parameters of both laser types, see Tab. 2.1. For the determination of modal gain and internal losses see Sec. 2.3.2 and 2.4.1, respectively.

To summarize, distributed-feedback laser diodes are compact, robust and economical light sources with excellent beam characteristics. Ultra-narrow linewidth and CW emission close to 1 W have been demonstrated at nearly diffraction limited beam quality. Spectral selectivity is achieved via a Bragg grating which covers the whole resonator length. In manufacture, this requires multiple etching steps and two epitaxy runs.

2.2 Gain Switching

In recent years, picosecond light sources have found a diversity of applications in fields like material processing [58–60], remote sensing, and fluorescence spectroscopy [61–63]. Particularly the compact and economical light sources based on gain switched diode lasers have increased the popularity of picosecond pulses as a versatile analysis tool [12]. In contrast to other pulse generation methods, gain switched pulses can be generated at arbitrary repetition rates or on demand, as required for several applications. For example, pulse bursts allow for superior cut edges in material processing [64], while adjustable repetition rates help to avoid photo bleaching in fluorescence spectroscopy [61].

2.2.1 Basic Principle

Solid-state lasers and most diode lasers operate in class B regime, in which the upper-state lifetime is longer than the cavity damping time. When such a laser is disturbed during operation, for example by a change in pump power, its output power does not transition smoothly to the new steady state. Instead, the laser exhibits *relaxation oscillations*, damped oscillations of the output power and the inversion density leading to the new steady-state value [65,66].

Particularly pronounced relaxation oscillations appear when the pump power is suddenly switched on. For low damping, as in solid-state lasers, the first couple of spikes can take the form of separate laser pulses with a high extinction ratio. Diode lasers have much shorter upper-state lifetimes and typically exhibit strongly damped relaxation oscillations that reach the steady state within a few nanoseconds (Fig. 2.10a).

Gain switching exploits the overshoot of the optical power during the first relaxation oscillation for the generation of short optical pulses. For this, the pump power is quickly switched off after the first optical relaxation peak has been emitted (Fig. 2.10b). This yields a single optical pulse whose peak power can be many times higher than the laser's steady-state output power. If the pump pulse amplitude is increased, the first relaxation oscillation appears after a shorter delay [65]. It is followed by a characteristic optical afterpulse, as the output power follows the remainder of the pump pulse (Fig. 2.10c) [67]. In order to obtain both a symmetric optical pulse shape and a high peak power, shorter pump pulses are required [66].

Within the single-pulse regime, an increased pump pulse amplitude not only leads to a higher optical peak power, but also to a decreased optical pulse duration [68–70].
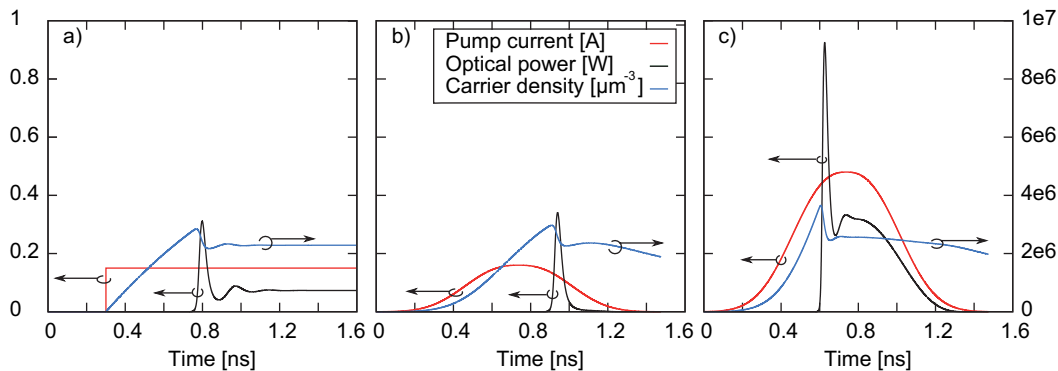
Figure 2.10: Simulation of a gain switched laser diode showing the pump current, carrier density ($\hat{=}$ inversion) and optical output power. a) Sudden switch-on of a DC pump current, b) and c) pumping with a short current pulse. For low pump pulse amplitudes (b), a single optical pulse is emitted. For higher pump pulse amplitudes (c), the optical pulse exhibits an afterpulse that follows the pump pulse shape. For details of the simulation, see Sec. 2.3.1.2.

2.2.2 Gain-Switched Diode Lasers

Gain-switching is particularly popular for diode lasers, which require sub-nanosecond current pulses for pumping. These can be generated in a variety of setups, and a large parameter space has been explored.

If high pulse repetition rates are desired, a suitable pump source consists of a *sine-modulated current*. While the electronic setup is fairly simple, the pump pulse length is inversely proportional to the repetition rate. Therefore, the method is only suitable for repetition rates in the low GHz range. For lower repetition rates, the long pump pulses cause a degradation of the optical pulse shape. The upper cutoff frequency is similar to the small-signal modulation bandwidth [71] and is given by the intrinsic time constants of the laser [72,73].

However, using a sine-modulated pump current, one gives up a major advantage of gain switching: the possibility to generate arbitrary pulse sequences. In order to implement variable repetition rates between single-shot and the upper MHz range, *single current pulses* can be generated by avalanche circuits [65, 66, 74]. This allows the optimization of the pump pulse duration independently of the pulse repetition rate. While shorter pump pulses generate shorter and more symmetric laser pulses, they are also harder to generate at variable repetition rates from a single driver circuit.

In any pump setup, the pump power needs to return below the lasing threshold in between the gain switching pulses in order to exploit the optical relax-

ation oscillation. A below-threshold DC bias can however be beneficial as it leads to a decreased optical pulse width and higher peak power [68,69,74]. On the other hand, negative bias voltages can also cause pulse shortening [75].

In addition to detailed studies of the pump parameters, efforts have been made to optimize the quantum well structure [67,76] or the resonator geometry [77] of laser diodes for gain switching operation. Pulses as short as 2 ps with a minimum pulse interval of 16 ps have been demonstrated [76].

2.2.3 Other Pulse Generation Methods

Alternative methods for the generation of optical picosecond pulses include mode-locking [78] and Q-switching [79–82]. Each method has a specific set of advantages [83] (Tab. 2.2) that make it suitable for particular applications.

In *mode-locking*, laser pulses are generated by the coherent superposition of many longitudinal laser modes. They add up to a single optical pulse circulating in the laser resonator. This fixes the pulse repetition rate to the resonator roundtrip time. Compared to the other pulse generation methods, mode-locking allows the generation of the shortest laser pulses, and pulse durations below 2 ps FWHM have been demonstrated [78, 84]. Moreover, very high pulse repetition rates of several GHz and low timing jitters are possible [78, 85], making mode-locked diode lasers ideally suited for optical telecommunications.

For an implementation in a monolithic semiconductor laser, a layout with at least two resonator sections is necessary [78]. Beside the gain section, a reverse bias section acting as a saturable absorber is required. An additional phase section can provide stability at lower repetition rates. While such a multi-section laser diode is rugged and compact, it has to be custom-built, making availability low and expensive, especially if several wavelengths are required.

On the other hand, mode-locked semiconductor lasers can be implemented using an external resonator with a saturable absorber and a generic laser diode as the gain medium [86]. However, external resonators are mechanically less stable and have a larger footprint than monolithic diode lasers.

In *Q-switching*, the resonator quality Q is modulated at constant material gain in order to generate a laser pulse. While the resonator loss is high, energy is stored in the active medium. This is suddenly released in the form of a short laser pulse when the resonator is switched to its low-loss state. If the quality increase is triggered externally (*active Q-switching*), a variation of the repetition rate is possible [80]. *Passive Q-switching* can occur in any laser resonator that contains a saturable absorber. Here, no external control of the pulse repetition rate is possible, unless the gain is also modulated [81].

	Gain-switching	Q-switching	Mode-locking
Typ. pulse duration	20–100 ps	20–100 ps	2–20 ps
Typ. pulse energy	<100 pJ	100–500 pJ	20–50 pJ
Typ. pulse peak power	<1 W	1–10 W	1–5 W
Repetition rate	variable 0–5 GHz	variable >0.5 GHz	fixed >5 GHz
Timing jitter	>5 ps	>5 ps	<1 ps
Cavity sections	1	2	≥2

Table 2.2: Typical pulse parameters of gain switched, Q-switched, and mode-locked monolithic diode lasers

Q-switching is particularly popular with solid-state lasers whose upper-state lifetimes are long, allowing the storage of large amounts of energy in the active medium. Q-switched semiconductor lasers can store less energy, but their short resonators enable high repetition rates above 10 GHz and short pulse durations below 50 ps [79, 81, 82]. High peak powers of up to 45 W in a single transverse mode have been realized [81]. Similar to mode-locked diode lasers, Q-switched diode lasers have either an external cavity or a monolithic multi-section layout to implement the required absorber.

In conclusion, gain switching generates neither the highest peak powers nor the shortest pulses, but it has two major advantages. Firstly, pulses can be generated at arbitrary repetition rates from single-shot to several GHz. Secondly, generic single-section laser diodes can be used, making gain switched laser pulse sources particularly compact and economical. These features make gain switched diode lasers a popular choice for analytical methods where moderate intensities and flexible pulse trains are required.

2.3 Modeling of Diode Laser Dynamics

Accurate models of diode lasers can significantly reduce time and resources needed in device optimization. They also help in the design of experiments by allowing the prediction of novel behaviors and operation regimes. The variation of individual parameters can furthermore increase physical understanding, in particular if these parameters cannot be modified individually in experimental systems.

For all of these applications, a close match between the simulated laser characteristics and the experimental data is vital. For each task, the required level of complexity needs to be balanced against computational effort. For example, a discussion of the beam quality of a broad area laser will require a spatially resolved simulation of heat generation and dissipation, which can generally be neglected in ridge-waveguide devices. A simulation of gain switching, on the other hand, needs picosecond time resolution and the ability to describe a laser both above and below threshold.

2.3.1 Dynamic Models of Distributed Feedback Lasers

Over the years, multiple large-signal models of distributed-feedback lasers have been proposed. In addition to the traveling wave equations (Sec. 2.3.1.1), *transfer matrix models* have been suggested. They essentially divide the laser resonator longitudinally into many slabs, describing the amplification and distributed reflectivity through transfer matrices between the slabs. This has the advantage of being conceptually and mathematically simple and allows the description of longitudinal inhomogeneities such as spatial hole burning. However, computational effort increases severely with the number of slabs, which in practice limits the spacial resolution. Moreover, intricate iteration procedures are necessary in order to include laser dynamics [87, 88].

Transfer matrix methods have been frequently used in combination with the traveling wave equations by using few large sections each described by the traveling wave equations. The connections between the segments are described by transfer matrices [89, 90]. This is particularly useful for lasers with inhomogeneous gratings.

2.3.1.1 The Traveling Wave Equations

Since their formulation by Kogelnik in 1972 [91], the *traveling wave equations (TWE)* have enjoyed large popularity and are the most common model of DFB lasers today [27, 92–96].

Their derivation starts from the Helmholtz equation for the complex electric field amplitude E

$$\frac{\partial^2 E}{\partial z^2} + \frac{\omega^2 \tilde{n}^2}{c_0^2} E = 0, \tag{2.1}$$

where ω is the light frequency, c_0 is the vacuum velocity of light, and

$$\tilde{n} = n + \frac{1}{2} i \frac{c_0}{\omega} g \tag{2.2}$$

the complex refractive index. This definition gives us the complex propagation constant $k = \beta + \frac{1}{2} i g$, where $\beta = \omega n / c_0$ is the ordinary propagation constant and g is the optical net intensity gain. With the assumption of small gain, $g \ll \beta$, the constant in the Helmholtz equation is

$$\frac{\omega^2 \tilde{n}^2}{c_0^2} = k^2 \approx \frac{\omega^2 n^2}{c_0^2} + i g \frac{\omega n}{c_0}.$$

In the case of index coupling, the Bragg grating is modeled as a periodic variation of the refractive index, expressed as a Fourier series along the direction z of the optical axis:

$$n = n_0 + \sum_{\mu \neq 0} n_\mu \exp(i \mu \beta_{\mathrm{g}} z),$$

where $\beta_{\mathrm{g}} = 2\pi n_0 / \Lambda$ is the wavenumber of the grating. With the approximations of low gain ($g \ll \beta_0$) and low index fluctuations ($n_{\mu \neq 0} \ll n_0$), this yields

$$k^2 \approx \beta_0^2 + i \beta_0 g + 2 \beta_0 \frac{\omega}{c_0} \sum_{\mu \neq 0} n_\mu \exp(i \mu \beta_{\mathrm{g}} z),$$

with the average propagation constant $\beta_0 = 2\pi n_0 / \lambda$.

Now, a solution to the Helmholtz equation 2.1 is required with this z-dependent propagation constant. Solutions occur close to each Bragg order. For a grating of order q, one therefore makes the ansatz

$$E = R^-(z) \exp(-i \tfrac{q}{2} \beta_{\mathrm{g}} z) + R^+(z) \exp(+i \tfrac{q}{2} \beta_{\mathrm{g}} z)$$

for a single transverse mode with wavenumber $\frac{q}{2} \beta_{\mathrm{g}}$. $R^-(z)$ and $R^+(z)$ are the complex amplitudes of the forward and backward propagating waves, respectively. These contain a phase factor describing the wavelength difference to the Bragg wavelength.

When this ansatz is plugged into the Helmholtz-equation 2.1, the left-hand side only contains the exponentials $\pm i \frac{q}{2} \beta_{\mathrm{g}} z$, while on the right-hand side, all multiples of $i \beta_{\mathrm{g}} z$ are present. Light waves with wavenumbers $|\mu \beta_{\mathrm{g}}| > \frac{q}{2} \beta_{\mathrm{g}}$,

$\mu \in \mathbb{Z}$, cannot exist close to the Bragg frequency, since the guided mode from the ansatz runs along the z-axis. Terms with wavenumbers $|\mu\beta_{\mathrm{g}}| < \frac{q}{2}\beta_{\mathrm{g}}$ represent radiative modes that run at an angle to the optical axis [31]. Therefore, no radiative modes exist for a first-order grating and it only couples the counterpropagating modes with wavenumber $\pm i\frac{q}{2}\beta_{\mathrm{g}}z$. In the general case, the coupling between the guided modes is provided by the Fourier component $n_{\pm q}$, which needs to be maximized in the design of higher-order gratings.

By comparing terms with equal exponentials, differential equations for R^- and R^+ are obtained. In the slowly-varying-envelope approximation ($\frac{\partial^2 R^\pm}{\partial z^2} \approx 0$), these are the well-known traveling wave equations

$$-\frac{\partial R^-}{\partial z} + \left(\tfrac{1}{2}g - i\delta\beta\right) R^- = i\kappa R^+,$$
$$\frac{\partial R^+}{\partial z} + \left(\tfrac{1}{2}g - i\delta\beta\right) R^+ = i\kappa R^-,$$

with the coupling coefficient $\kappa = \beta_0 n_q/n_0$ and the frequency deviation

$$\delta\beta = \frac{1}{2}\frac{n_0}{c_0}\left(\frac{q}{2}\omega_g - \omega\right),$$

where ω_g is the angular frequency of the grating.

This formalism can be readily expanded to gain- or loss-coupled gratings by a modification of the coupling constant κ [91]. The radiative loss caused by higher-order gratings can be subsumed in the net gain and a slight wavelength shift [92–94].

In order to describe DFB lasers close to threshold, a model for the spontaneous emission needs to be included. This is commonly done by adding a source in the form of stochastic Langevin functions $f_\omega^\pm(z)$ [27, 31, 97]:

$$-\frac{\partial R^-}{\partial z} + \left(\tfrac{1}{2}g - i\delta\beta\right) R^- - i\kappa R^+ = f_\omega^-(z),$$
$$\frac{\partial R^+}{\partial z} + \left(\tfrac{1}{2}g - i\delta\beta\right) R^+ - i\kappa R^- = f_\omega^+(z). \tag{2.3}$$

The ensemble averages of the Langevin noise functions vanish, $\langle f_\omega^\pm(z)\rangle = 0$, and the correlation functions are non-zero only at identical parameters,

$$\left\langle f_\omega^+(z)f_{\omega'}^+(z')\right\rangle = \left\langle f_\omega^-(z)f_{\omega'}^-(z')\right\rangle = \hbar\omega g n_{\mathrm{sp}}\delta(z - z')\delta(\omega - \omega'),$$

where n_{sp} is the factor between stimulated and spontaneous emission.

These extended traveling wave equations 2.3 can be used to simulate the amplified spontaneous emission (ASE) of DFB lasers [27] (Fig. 2.6). Fitting

Figure 2.11: ASE spectrum of laser C1336-6-3 020408 at 300 K and 40 mA pump current. Measurement with Advantest Q8384 with 10 pm resolution, simulation of traveling wave equations with fitted values for the coupling coefficient $\kappa = 1.0\,\mathrm{cm}^{-1}$ and the grating phases $\varphi_\mathrm{L} = 0.56\,\pi$, $\varphi_\mathrm{R} = 0.15\,\pi$ at the facets.
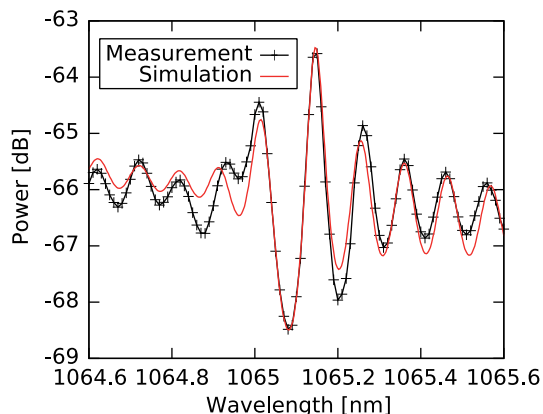
the simulated ASE spectra to measurement data allows the determination of the coupling coefficient κ and the grating phases at the facets (Fig. 2.11). In this work, the existing implementation by Wenzel et al. [27] was used for this purpose.

2.3.1.2 The Rate Equation Model

The *rate equations* are a set of balance equations for the average photon density S and the average carrier density N in the laser cavity. Their numerical solution and physical interpretation are straightforward, and they are widely used in the simulation of Fabry-Pérot lasers [69, 70, 72, 74, 76, 98, 99]. Forward- and backward-running waves are not distinguished, and the facet losses are treated as a constant loss rate. This means that the rate equations are only applicable for dynamic processes on time scales longer than the resonator roundtrip time. Due to the lack of spatial resolution, distributed feedback cannot be modeled directly using the rate equations. However, good agreement with experimental measurements can be achieved using an effective photon lifetime (Sec. 2.4.1).

In order to derive the rate equations, consider light circulating in a laser resonator with length L and mirror reflectivities R_L and R_R, where net modal gain g_net is assumed to be spatially constant and temporally constant on the timescale of one resonator roundtrip. The first assumption is valid in many semiconductor lasers with cleaved facets but not for very low facet reflectivities [100] or for lasers with strong spatial hole burning such as $\lambda/4$-shifted DFB lasers. Then, the light intensity $P(2L)$ after one roundtrip is

$$P(2L) = P(0)R_\mathrm{L}R_\mathrm{R}\exp(g_\mathrm{net}2L) + P_\mathrm{sp},$$

where $P(0)$ is the light intensity at the start of the roundtrip and P_sp is the light that is spontaneously emitted into the lasing mode.

23

The net gain consists of the modal gain g_m and the internal losses α, $g_\mathrm{net} = g_\mathrm{m} - \alpha$. In analogy, the facet losses are defined as [101]

$$\frac{1}{\tau_\mathrm{R}} = \frac{c}{2L} \log\left(\tfrac{1}{R_\mathrm{L} R_\mathrm{R}}\right), \tag{2.4}$$

where c is the velocity of light in the medium, and write

$$P(2L) = P(0) \exp\left(2L\left(g_\mathrm{m} - \alpha - \frac{1}{c\tau_\mathrm{R}}\right)\right) + P_\mathrm{sp}. \tag{2.5}$$

In effect, this means that the mirror reflectivity is distributed over the whole resonator length. This approximation is valid on time scales longer than the round-trip time.

Similar to the gain, the spontaneous emission rate is considered to be constant, so that $P_\mathrm{sp} = n_\mathrm{sp} R_\mathrm{sp} \frac{2L}{c}$, where R_sp is the total spontaneous emission rate of the active medium and the spontaneous emission factor β_sp is the fraction of spontaneously emitted photons that enter the lasing mode.

Going from the intra-cavity power to the photon density S and from the modal gain to the material gain $g(N)$, Eq. 2.5 becomes

$$S(z) = S(0) \exp\left(z\left(\Gamma g(N) - \frac{1}{c\tau_S}\right)\right) + \Gamma \beta_\mathrm{sp} R_\mathrm{sp} \frac{z}{c}, \tag{2.6}$$

where the confinement factor Γ is the ratio between the mode volume and the volume of the active zone and

$$\tau_S := \frac{1}{c\alpha + \frac{1}{\tau_\mathrm{R}}} \tag{2.7}$$

is the total photon lifetime.

The total spontaneous emission rate can be calculated according to Einstein [102] by considering a piece of active medium in thermal equilibrium and evaluating the balance equation of all forms of carrier recombination. The dependence on the carrier density is approximately quadratic [103], $R_\mathrm{sp} = BN^2$.

The rate equation for the photon density is the time derivative of Eq. 2.6,

$$\frac{\mathrm{d}S}{\mathrm{d}t} = \left(c\Gamma g(N) - \frac{1}{\tau_\mathrm{S}}\right)S + \beta_\mathrm{sp} BN^2, \tag{2.8}$$

where Γ was absorbed into β_sp.

During stimulated and spontaneous emission, one electron-hole pair recombines for each photon that is generated. Therefore, one term in the rate equation for the carrier density is

$$\frac{\mathrm{d}N}{\mathrm{d}t} = -cg(N)S - BN^2.$$

The confinement factor does not enter into this formula, as the charge carriers are confined to the active zone.

In addition, terms for non-radiative recombination, R_{nr}, and a pump term $I/(eV)$ are included, which contains the assumption that every injected electron creates one electron-hole pair. Writing $R(N) = R_{\mathrm{nr}} + R_{\mathrm{sp}}$, the final rate equation for the carrier density is

$$\frac{\mathrm{d}N}{\mathrm{d}t} = \frac{I}{eV} - cg(N)S - R(N). \tag{2.9}$$

Several processes contribute to the non-radiative carrier recombination. The major ones are recombination at lattice defects and Auger recombination. Lattice defects and impurities can give rise to mid-bandgap energy levels that can temporarily trap an electron before releasing it into the valence band (Shockley-Read-Hall recombination). For high injection, its contribution is linear in N [104].

Auger recombination is essentially the collision between two electrons which makes one electron drop to the valence band while the other is excited to a higher-energy state. It involves two electrons and one hole (or two holes and one electron) and is proportional to N^3 for lightly doped regions [104]. The nonradiative recombination thus can be written as

$$R(N) = N/\tau_N + BN^2 + CN^3, \tag{2.10}$$

where typical values of the coefficients for a laser wavelength of 1060 nm are [88, 96, 105, 106]

$$\tau_N \approx 2\,\mathrm{ns}, \quad B \approx 10^{-10}\,\mathrm{cm}^3\,\mathrm{s}^{-1}, \quad C \approx 10^{-29}\mathrm{cm}^6\,\mathrm{s}^{-1}.$$

Many authors have experimentally observed a decrease of gain at high photon densities and have added a phenomenological *gain compression factor* ε to the gain term of the rate equations [98, 107–110],

$$g(N)S \to g(N)\frac{S}{1 - \varepsilon S}.$$

Many physical explanations have been put forward, and the dominating mechanisms for near-IR laser diodes seem to be spectral hole burning and carrier heating [108, 110].

In order to apply the rate equation model to DFB lasers, the effective photon lifetime τ_S has to be determined for a given coupling coefficient κ and facet phases φ_{L} and φ_{R}. Considering the steady state of Eq. 2.8 shows that τ_S is closely related to the threshold gain g_{th}, $1/\tau_S = \Gamma g_{\mathrm{th}}$. For a DFB laser, the latter can be calculated analytically from the traveling wave equations [95].
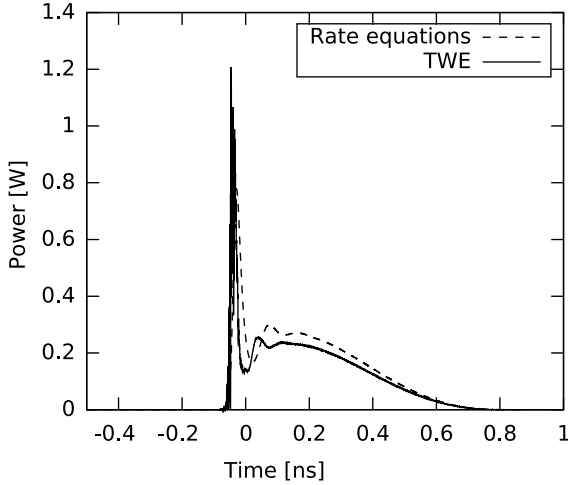
Figure 2.12: Simulation of a gain switched laser pulse using the traveling wave equations (TWE) (simulated using LDSL [96]) and the single-mode rate equations for a 1.5 mm long laser diode. As expected, the rate equations do not reproduce features on time scales below the resonator roundtrip time of 30 ps.

Even though the rate equations do not spatially resolve the DFB Bragg grating, remarkable agreement to the traveling wave equations can be reached (Fig. 2.12). For this comparison, the parameters of wafer C1340-6-3 at 300 K (Tab. 2.3) were used with a logarithmic gain model [96]. For the simulation of the traveling wave equations, the commercial tool LDSL [96] was utilized. The single-mode rate equations were solved using the Euler method. As expected, the rate equations do not include features on time scales below the resonator round trip time (here: 30 ps for a 1.5 mm long diode laser), but the pulse envelope is in good agreement for both methods. The shorter rise time in the traveling wave equations model is due to the inclusion of multiple longitudinal modes. The lower power in the pulse tail is due to longitudinal spatial hole burning. However, this can be corrected by choosing slightly different parameters for the pump pulse. Therefore, it seems justified to use the rate equation model for simulations of DFB gain switching.

2.3.2 The k·p-Model of Gain in Semiconductors

The determination of the optical gain spectrum in a semiconductor device starts with the calculation of the bulk band structure. The k·p-model is the most widely used method for this and is based on perturbation theory starting from the zone-center with $\vec{k} = 0$.

Due to the lattice periodicity, all energy eigenstates $|\varphi_{n\vec{k}}\rangle$ in a bulk semiconductor crystal take the Bloch form

$$\left\langle \vec{r} \,\middle|\, \varphi_{n\vec{k}} \right\rangle = \exp(i\vec{k} \cdot \vec{r}) \left\langle \vec{r} \,\middle|\, n\vec{k} \right\rangle,$$

where n is the band index, $\vec{k}$ the electron wave vector, and $\langle \vec{r} | n\vec{k} \rangle$ the lattice

periodic function. By plugging this into the Schrödinger equation

$$\left(\frac{\vec{p}}{2m_0} + V_0(\vec{r}) \right) \left| \varphi_{n\vec{k}} \right\rangle = E_{n\vec{k}} \left| \varphi_{n\vec{k}} \right\rangle,$$

where m_0 is the free electron mass and $V_0(\vec{r})$ is the periodic crystal potential, the k·p equation [21, 111]

$$H_{\text{k·p}} \left| n\vec{k} \right\rangle := \left(\frac{\vec{p}^2}{2m_0} + \frac{\hbar \vec{k} \cdot \vec{p}}{m_0} + V_0(\vec{r}) \right) \left| n\vec{k} \right\rangle = \left(E_{n\vec{k}} - \frac{\hbar^2 \vec{k}^2}{2m_0} \right) \left| n\vec{k} \right\rangle \quad (2.11)$$

is obtained.

Group theoretical considerations and experimental measurements show the symmetry of the energy eigenstates at $\vec{k} = 0$ [111]. Disregarding spin, the conduction band state is non-degenerate with s-like symmetry. The top states in the valence band are threefold degenerate and have p-like symmetry.

The energy eigenstates can now be expressed for general $\vec{k}$ as a linear combination of the $\vec{k} = 0$ eigenstates, and find the coefficients via perturbation theory. For this, the Hamiltonian is split up as

$$H_0 = \frac{\vec{p}^2}{2m_0} + V(\vec{r}), \quad H_1 = \frac{\hbar \vec{k} \cdot \vec{p}}{m_0}.$$

Perturbation theory readily yields the (only spin-degenerate) eigenstates and effective masses of the conduction band [21]. For the valence band with three degenerate states, matters are a bit more complicated. In order to determine the energy corrections to second order, one needs to decouple the degenerate subspace from all other states to first order. This can be achieved by the method of infinitesimal basis transformations [112]. Including spin, this yields a 8×8 Hamiltonian matrix whose eigenvalues are the desired valence band energies to second perturbation order (see [21, 111, 113] for the matrix elements).

The deviations from the ideal, infinite crystal in multilayer semiconductor devices can be expressed as an external potential $V_{\text{ext}}(\vec{r})$ that does not have the lattice periodicity. Therefore, the solutions to the full Hamiltonian are no longer Bloch functions. However, a sufficiently weak potential can be treated by perturbation theory starting from the full k·p Hamiltonian as H_0 [21]. This is called the *envelope function approximation*, because the new eigenstates (the envelope functions) vary only slowly across one lattice unit cell.

The inclusion of quantum well strain leads to another perturbation to the k·p Hamiltonian which also has k·p form [21, 113].

Since the only $\vec{k}$-dependence of the k·p-Hamiltonian is of the form $\vec{k}\cdot\vec{p}$, the momentum matrix elements can be calculated via the $\vec{k}$-derivative of the energy matrix elements [113, 114],

$$\vec{p}_{nm} = \frac{m_0}{\hbar}\vec{\nabla}_{\vec{k}}\langle\psi_n\,|\,H_{\text{k·p}}\,|\,\psi_m\rangle\,,$$

where m, n are band indexes and $|\psi_{n,m}\rangle$ are $\vec{k}$-independent envelope states.

The material gain g is given by the imaginary part of the optical susceptibility χ. This can be calculated from the electric polarization P:

$$g = -\frac{k}{2}\Im(\chi) = -\frac{k}{2}\Im\left(\frac{P}{\varepsilon_0 E}\right),$$

where E is the electrical field. Quantum mechanically, the polarization is proportional to the expectation value of the position of the electrons,

$$\vec{P}_{ij} \sim \langle\psi_i\,|\,\vec{r}\,|\,\psi_j\rangle\,.$$

According to Heisenberg's equation of motion, this can be expressed via the momentum matrix element,

$$\langle\psi_i\,|\,\vec{r}\,|\,\psi_j\rangle = \frac{i\hbar}{m_0(E_i - E_j)}\vec{p}_{ij}.$$

Taking into account the occupation probabilities for valence and conduction band, the gain spectrum can finally be calculated as [114]

$$g(\omega) = \frac{\pi\hbar q^2}{\varepsilon_0 m_0^2 n_r c_0 d_{QW}}\sum_{i,j}\int \mathrm{d}^2 k_\parallel \frac{1}{(2\pi)^2}\frac{\vec{p}_{ij}\vec{e}}{E_i - E_j}$$
$$f_e(E_i)\big(1 - f_h(E_j)\big)\left(1 - \exp\left(\frac{\hbar\omega - (E_{Fc} - E_{Fv})}{k_B T}\right)\right),$$

where q is the electron charge, n is the refractive index, d_{QW} is the quantum well thickness and $\vec{e}$ is the light polarization.

To model energy and phase relaxation, the calculated gain spectra and energy levels have to be broadened by convolution with a smooth lineshape function [114–116].

This k·p-model of optical gain accurately reproduces experimental quantum well gain spectra [115, 117, 118], especially the blue-shift of the gain maximum with increasing carrier density and the red-shift with increasing temperature. However, the quality of the agreement does depend on the details of the gain model [115–117].

In this thesis, an existing implementation by Wenzel et al. [119] is used, where the gain is spectrally broadened by a sech-function with an intra-band relaxation time of 66 fs. Band gap renormalization is included by means of an approximate formula derived by Zimmermann for bulk systems [120]. A linear dependence of the band gap on the temperature is assumed ($\mathrm{d}E_g/\mathrm{d}T = -4.5 \times 10^{-4}\,\mathrm{eV/K}$).

In summary, this section has provided short sketches of several theoretical models which are widely used in the simulation of laser diode dynamics. First, the traveling wave equations for DFB lasers were derived from the Helmholtz equation. Next, the spatially averaged rate equations were introduced. While these are commonly used for Fabry-Pérot laser diodes, good agreement with the traveling wave equations can be achieved for single-section DFB lasers. Both dynamic models require the separate simulation of the semiconductor gain spectrum. This starts with the calculation of the band structure in a strained quantum well in the k·p model. From this, the semiconductor gain spectrum can be calculated by linear response theory. In agreement with experimental data, the gain maximum shifts toward shorter wavelength with increasing carrier density and toward longer wavelengths with increasing device temperature.

2.4 Gain-Switching of Distributed Feedback Laser Diodes

Gain-switching of DFB laser diodes is a robust and economical way to produce spectrally narrow picosecond pulses (Sec. 2.2) that has been commercially exploited for a number of years. Still, the detailed study of the spectral dynamics and the parameter dependence of the pulse performance is worthwhile. It allows an in-depth understanding of the dynamical processes in DFB laser diodes and enables the optimization of the laser design and the operating conditions for the generation of pulses with peak powers greater than 1 W.

In the past, a number of theoretical and experimental studies have been performed on the spectral dynamics of gain switched Fabry-Pérot lasers [67, 76, 99, 121]. Pulses generally begin with a broad spectrum with a large number of modes, before the spectrum gradually narrows down to few modes similar to the lasers' CW spectrum. This has been explained by mode competition, where the decay time of the side modes is inversely proportional to the net gain difference to the dominant mode [99]. Furthermore, the spectral position of the gain maximum shifts dynamically with the carrier density, favoring shorter-wavelength modes during the first relaxation peak [67, 76, 121]. Numerically, the mode competition can be modeled by multi-mode rate equations [76, 99, 121] that describe each longitudinal mode by a separate rate equation. The accurate reproduction of the spectral shift, requires a realistic model of the optical gain spectrum and its dependence on carrier density.

On the other hand, only a few authors have investigated the spectral dynamics of DFB lasers. A first experimental study [122] led to the conclusion that for spectrally narrow pulse generation, the Bragg wavelength should be on the shorter-wavelength side of the gain maximum in order to avoid emission on residual Fabry-Pérot (FP) modes. Other studies focused on chirp [88, 123, 124] or linewidth broadening [88] of individual lasing modes during gain switching of DFB lasers.

This section presents a detailed investigation of the longitudinal mode dynamics in gain switched DFB lasers. The spectral dynamics during the first few relaxation oscillations are studied, including both the Bragg modes close to the stop band and the residual Fabry-Pérot modes. As in Fabry-Pérot lasers, the spectral dynamics are dominated by mode competition. Accordingly, the spectral quality of the first relaxation peak strongly depends on the net gain difference between Bragg and FP modes. This is determined both by the grating strength and by the wavelength difference $\Delta\lambda$ between gain maximum and Bragg wavelength, which can be tuned by changing the device temperature.

2.4.1 An Extension of the Rate-Equation Model to Mode Competition

The model presented in this section aims to simulate the mode competition between the Bragg-mode and the residual Fabry-Pérot modes during switch-on of a DFB laser. A common dynamic model for DFB lasers consists of the traveling-wave-equations [105] (Sec. 2.3.1.1). It allows the simulation of longitudinal inhomogeneities like spatial hole-burning. However, common implementations [96] assume that the whole lasing spectrum is close to a single reference wavelength. This assumption is not valid for the residual FP-modes.

Instead, a rate-equation model is used, treating the Bragg-mode (index B) and the Fabry-Pérot modes (index FP) as two species of photons S_i which interact with a single species of charge carriers N:

$$
\begin{aligned}
\frac{\mathrm{d}S_\mathrm{B}}{\mathrm{d}t} &= \Gamma c g_\mathrm{B}(N)\frac{S_\mathrm{B}}{1+\varepsilon S_\mathrm{B}} - \frac{S_\mathrm{B}}{\tau_{S_\mathrm{B}}(N)} + K_\mathrm{B}\beta_\mathrm{sp}BN^2, \\
\frac{\mathrm{d}S_\mathrm{FP}}{\mathrm{d}t} &= \Gamma c g_\mathrm{FP}(N)\frac{S_\mathrm{FP}}{1+\varepsilon S_\mathrm{FP}} - \frac{S_\mathrm{FP}}{\tau_{S_\mathrm{FP}}(N)} + K_\mathrm{FP}\beta_\mathrm{sp}BN^2, \quad (2.12) \\
\frac{\mathrm{d}N}{\mathrm{d}t} &= \frac{I}{eV} - R(N) - \frac{c g_\mathrm{B}(N)S_\mathrm{B}}{1+\varepsilon S_\mathrm{B}} + \frac{c g_\mathrm{FP}(N)S_\mathrm{FP}}{1+\varepsilon S_\mathrm{FP}}.
\end{aligned}
$$

A numerical comparison shows good agreement with the traveling-wave equations for the single-mode case (Fig. 2.12). This indicates that for the parameter range relevant to this study, realistic simulation results can be reached with a rate equation model.

$\Gamma c g_i(N)$ describes the modal gain, where Γ is the confinement factor and $c = c_0/n_g$ is the effective group velocity of the lasing mode. The model for the material gain g_i bases on the computation of the subbands and oscillator strengths using an eight-band k·p Hamiltonian taking into account all possible transitions in the quantum well (QW) [119] (Sec. 2.3.2).

The gain for the Bragg mode was calculated at wavelengths $\lambda_B(T)$, taking into account the slight shift of the Bragg wavelength with temperature. The FP-modes, on the other hand, are assumed to develop around the gain maximum, whose wavelength λ_FP depends on temperature and carrier density (Fig. 2.13). The wavelength difference $\Delta\lambda_0 = \lambda_\mathrm{B} - \lambda_\mathrm{FP}$ between Bragg wavelength and gain maximum at $T = T_0 = 300\,\mathrm{K}$ and $N = N_\mathrm{th}$ is determined from the CW emission spectrum above threshold. These spectra consist of a strong DFB line and an ASE background that is suppressed by at least $30\,\mathrm{dB}$ (Fig. 2.9). The gain maximum is assumed to be located at the maximum of the ASE background. Due to gain clamping, the carrier density is fixed to the threshold value N_th during CW emission. If $\Delta\lambda_0$ is negative (Bragg
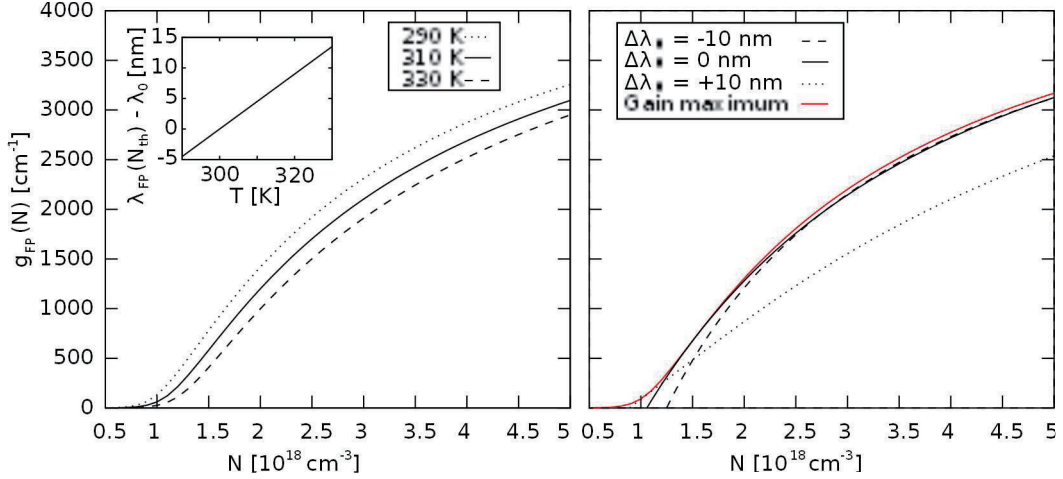
Figure 2.13: Simulated gain as a function of carrier density. Left: Peak gain (g_{FP}) for different temperatures. Inset: wavelength of gain maximum at threshold carrier density as a function of temperature. Right: Gain at 300 K at fixed wavelengths (see Fig. 2.22), and at gain maximum.

wavelength shorter than wavelength of gain maximum), the gain at the Bragg wavelength approaches the maximum gain for high carrier densities. If $\Delta\lambda_0$ is positive, the Bragg gain is close to the gain maximum at low carrier densities.

The photon lifetime τ_{S_i} depends on both the internal loss $\alpha(N)$ and the reflector loss $\tau_{R,i}$ (Eq. 2.7). α is dominated by free carrier absorption and therefore is a function of temperature T and carrier density:

$$\alpha(N) = \alpha_0 \left(f_n \frac{T}{T_0} + f_p \left(\frac{T}{T_0} \right)^2 \right) N$$

with $T_0 = 300$ K, $f_n = 4 \cdot 10^{-18}$ cm^2 and $f_p = 12 \cdot 10^{-18}$ cm^2 [106]. The reflector losses $\tau_{R,FP}$ for the FP-modes depend only on the residual facet reflectivities R_i (Eq. 2.4). For the Bragg-mode, however, the reflectivity of the optical grating increases the effective photon lifetime $\tau_{S,B}$, which can be calculated from the steady-state solutions of the traveling wave equations (Sec. 2.3.1.2). It was averaged over all grating phases at the facet to enable a comparison with measurements averaged over multiple laser diodes. Furthermore, Bragg- and FP-modes differ by the longitudinal Petermann factor K_i [125]. This correction factor for the stimulated emission depends on the longitudinal inhomogeneity of the photon density of the considered mode. In keeping with the assumptions made in the formulation of the rate equations (Sec. 2.3.1.2),

Param.	C1336-6-3	C1340-6-3	Param.	C1336-6-3	C1340-6-3
Carrier Recombination			Geometric Parameters		
τ_N	1.5 ns		length	1.5 mm	
B_0	$10^{-10}\,\mathrm{cm^3\,s^{-1}}$		width	5.1 μm	
C_0	$4 \cdot 10^{-30}\,\mathrm{cm^6\,s^{-1}}$		thickness	27 nm	
K_FP	117		Γ	0.04	
K_B	18.5	4.46	n_g	3.38	
β_sp	$15.5 \cdot 10^{-7}$				
ε	$6 \cdot 10^{-17}\,\mathrm{cm^3}$				
Photon Losses			Bragg Wavelength		
R_L	10^{-4}		$\Delta\lambda_0$	7.5 nm	5.8 nm
R_R	0.95		Pump Parameters		
κ	$0.9\,\mathrm{cm^{-1}}$	$2.2\,\mathrm{cm^{-1}}$	FWHM	610 ps	
α_0	0.80	1.05	I_max	470 mA	

Table 2.3: Simulation Parameters

the distributed Bragg reflectivity is modeled as two Fabry-Pérot mirrors with an effective reflectivity, which completely determines the Petermann factor.

Non-radiative carrier recombination is assumed to be cubic (Eq. 2.10), where $B = B_0 \frac{T}{T_0}$ and $C = C_0 \exp(\frac{E_0}{k_B T_0} - \frac{E_0}{k_B T})$ depend on temperature ($E_0 = 0.1\,\mathrm{eV}$) [106].

A phenomenological term $(1 + \varepsilon S_i)^{-1}$ for the gain compression has been introduced. While more complex schemes have been evaluated good agreement with the experimental data is found using a single gain compression factor ε.

For the simulation of gain switching, the electrical pump pulse shape is modeled as super-Gaussian with an exponent of 2.5. This produces a good fit to the tail of the measured pulse shape.

In order to determine the simulation parameters (Tab. 2.3), the DFB coupling coefficients κ and the group refractive index n_g are obtained from a fit of the amplified spontaneous emission (ASE) spectrum (Sec. 2.3.1.1). This allows the calculation of the photon lifetime for the Bragg mode $\tau_\mathrm{S,B}$ (Sec. 2.3.1.2) and the longitudinal Petermann factor [125].

The facet reflectivities R_L and R_R and the length and thickness of the active zone are set to their design values (Tab. 2.1). The confinement factor Γ is determined from a simulation of the transverse resonator modes. The parameters τ_N, B_0, C_0, and β_sp are set to literature values [88, 96, 105, 106].
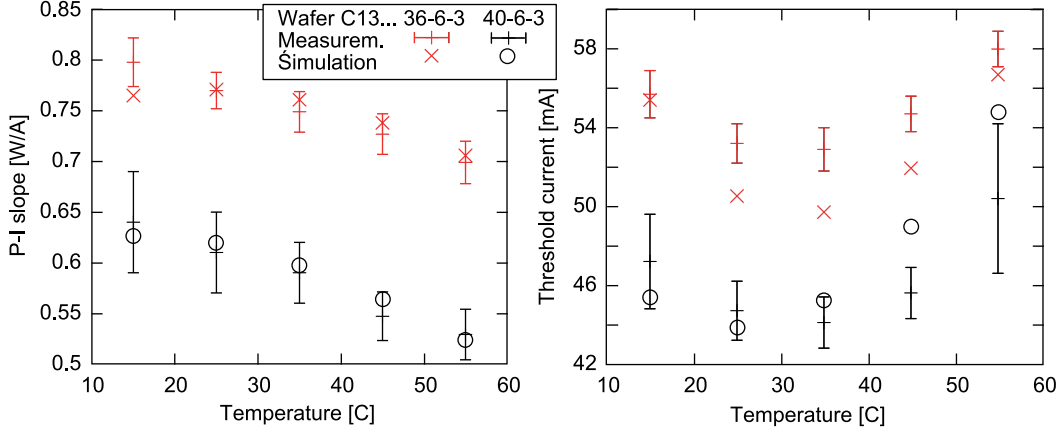
Figure 2.14: CW slope $\Delta P/\Delta I$ and threshold current I_{th}; measured data (average over 4 devices) and simulation

The steady-state solution of the rate equations(Eq. 2.12) gives us the threshold carrier density N_{th}, the threshold current I_{th}, and the slope m of the P-I-characteristics:

$$g_{\text{B}}(N_{\text{th}}) = \frac{1}{\tau_{S_{\text{B}}}\Gamma c},$$

$$I_{\text{th}} = eV \left(\frac{N_{\text{th}}}{\tau_N} + BN_{\text{th}}^2 + CN_{\text{th}}^3 \right), \tag{2.13}$$

$$m = \frac{hc_0}{\lambda e} \frac{1}{c\alpha(N)\tau_{\text{R,B}} + 1}, \tag{2.14}$$

assuming that the CW threshold of the Bragg mode is lower than that of the residual Fabry-Pérot modes at all temperatures.

The intra-cavity loss α_0 includes radiative losses from the second-order grating (Sec. 2.3). The value for each laser type is determined by fitting Eq. 2.14 to the measured P-I-slope (Fig. 2.14). Similarly, a fit of Eq. 2.13 to the measured CW threshold currents allows us to determine the effective width of the active zone, which is broadened due to current spreading.

The gain compression parameter ε cannot be obtained from the lasers' CW behavior. Furthermore, the effective pump pulse duration and amplitude are not known precisely since they sensitively depend on parasitics in the laser diode and its mount. These parameters are determined by fitting the simulated gain switched pulse shape to the measured one in single-mode regime (wafer C1340-6-3 at 310 K).
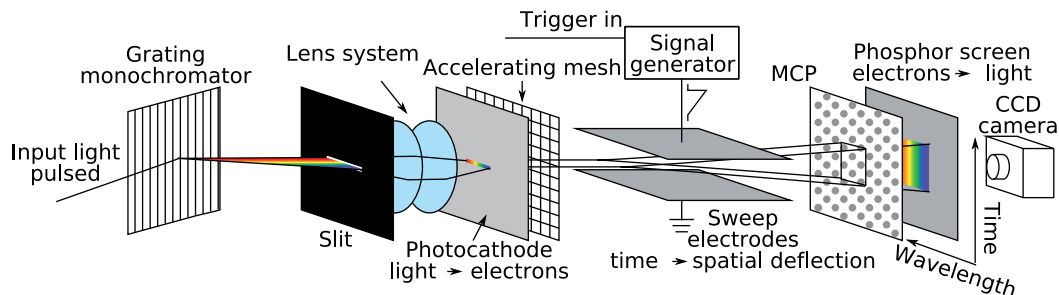
Figure 2.15: Schematic setup of a streak camera. First, the wavelength information is converted into spatial deflection in a grating monochromator. Then, the temporal information is converted into spatial deflection in the perpendicular direction in the streak camera. To do this, the light is converted to electrons in a photocathode, these are deflected by a ramped electric field. The multi-channel plate (MCP) serves to amplify the electron signal.

2.4.2 Device and Measurement Setup

For the present gain switching experiments, DFB lasers of wafers C1336-6-3 and C1340-6-3 (device layout: Sec. 2.1.3, CW characteristics: Sec. 2.1.4) are mounted p-side up on a C-mount and attached to a Peltier-cooled heat sink. They are pumped with short current pulses at a repetition rate of 10 MHz.

Laser emission spectra are measured on a logarithmic scale using an Advantest Q8384 spectrum analyzer with a resolution of 10 pm. Pulse shapes are measured on a relative scale using a fast photodiode (New Focus 1434) and a sampling oscilloscope (LeCroy WaveExpert NRO9000) with a total impulse response time of 25 ps FWHM. Pulse lengths and peak powers stated in this thesis are as measured without deconvolution with the instrument response function.

The average laser output power is measured using an Ulbricht integrating sphere and a Newport 818-SL Silicon photodetector. Its accuracy is approximately $\pm 10\%$, precision is higher at $\pm 3\%$. The pulse energy E_{p} is obtained by deviding the avarage power by the repetition rate. From the pulse energy and the measured pulse shape, the pulse peak power P_{max} is determined.

Direct measurements of the spectral dynamics are done with a streak camera (Hamamatsu C5680) with spectroscope (Fig. 2.15), allowing a temporal resolution of 33 ps and a spectral resolution of 150 pm at the selected settings. Images were averaged over 1000 laser pulses. Independent measurements of the time-averaged spectrum over a high dynamic range allow for a precise estimate of the energy content E_{B} of the Bragg mode.

Figure 2.16: Streak camera images of the picosecond pulses generated from a gain switched DFB laser diode (C1336-6-3 020410) at different temperatures. The coupling coefficient of this device is $\kappa = 0.9\,\mathrm{cm}^{-1}$.

2.4.3 Mode Competition and Spectral Dynamics

To experimentally study the spectral dynamics of DFB lasers under gain switching operation, the time-dependent spectra at different device temperatures are measured directly using a streak-camera with spectroscope (Fig. 2.16 and 2.17).

When the heat-sink temperature is increased, the gain maximum shifts toward longer wavelengths by approximately $0.48\,\mathrm{nm/K}$. Simultaneously, the Bragg wavelength shifts by $0.08\,\mathrm{nm/K}$ due to the temperature dependence of the refractive index. Since the investigated laser diodes were optimized for high-power CW operation, the gain maximum λ_{FP} is on the shorter-wavelength side of the Bragg wavelength at room temperature and threshold carrier density ($1057.6\,\mathrm{nm}$ for wafer C1336-6-3 and $1055.2\,\mathrm{nm}$ for C1340-6-3). As the device is warmed up, the gain maximum shifts toward the Bragg wavelength by $0.40\,\mathrm{nm/K}$ and the material gain at the Bragg wavelength increases.

Thus, pulse measurements at different heat sink temperatures show qualitatively different dynamic spectra. At $290\,\mathrm{K}$, lasers from wafer C1336-6-3 ($\kappa = 0.9\,\mathrm{cm}^{-1}$) show broadband emission over the whole pulse duration, with less than 20% of the pulse energy contained in the Bragg mode (Fig. 2.16, top). In contrast, at $330\,\mathrm{K}$, the same lasers emit more than 95% of the pulse energy at the Bragg-wavelength, with a time-averaged side-mode suppression ratio of about $35\,\mathrm{dB}$ (Fig. 2.16, bottom). At this setting, the pulse duration is $(68\pm3)\,\mathrm{ps}$ and the peak power is $(1.05\pm0.06)\,\mathrm{W}$, which makes these pulses excellently suited for second harmonic generation (SHG).
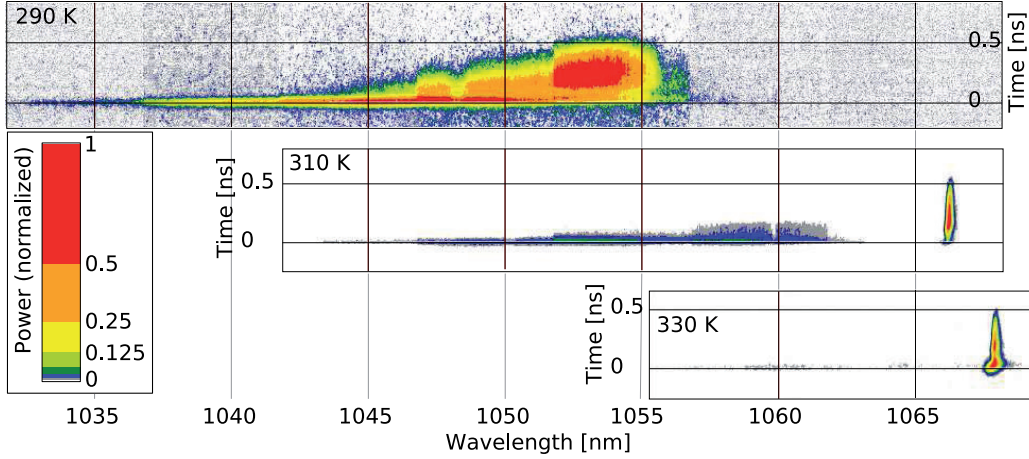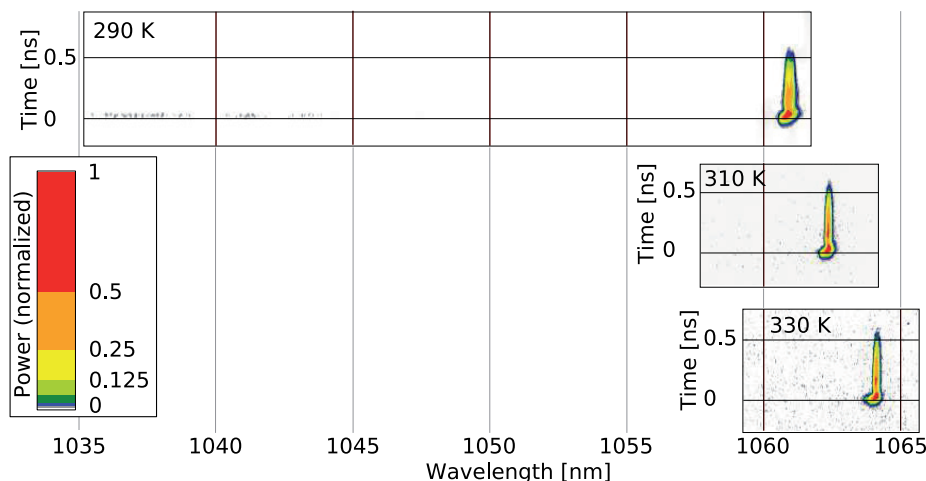
Figure 2.17: Streak camera images of the picosecond pulses generated from a gain switched DFB laser diode (C1340-6-3 010813) at different temperatures. The coupling coefficient of this device is $\kappa = 2.2\,\mathrm{cm}^{-1}$.

An example of the intermediate spectral behavior can be found at 310 K, where the pulse peak is dominated by the broadband Fabry-Pérot modes, while the afterpulse is emitted at the Bragg wavelength (Fig. 2.16, center). In the temporal average, $(73 \pm 3)\%$ of the pulse energy is contained in the Bragg mode. Still, these laser pulses are poorly suited for second harmonic generation because the high-power pulse peak is spectrally broad.

Lasers from wafer C1340-6-3 have a stronger DFB grating ($\kappa = 2.2\,\mathrm{cm}^{-1}$) and perform better at low temperatures. At 290 K, they already emit $(89\pm4)\%$ of the pulse energy at the Bragg wavelength (Fig. 2.17, top), this rises to more than 99% at temperatures above 305 K. At all temperatures between 290 K and 330 K, these lasers have an average side-mode suppression ratio of more than 30 dB under gain switching operation, making them excellently suited for SHG.

However, the improved spectral discrimination comes at a cost: At the same device temperature and pump conditions, lasers from wafer C1340-6-3 generate pulses with lower peak power than those of wafer C1336-6-3. At 330 K, both laser types emit essentially in a single longitudinal mode. Here, lasers from wafer C1336-6-3 emit pulses with a peak power of $(1.05 \pm 0.06)\,\mathrm{W}$ while the pulses generated by lasers from wafer C1340-6-3 have a peak power of only $(0.59 \pm 0.04)\,\mathrm{W}$ (Fig. 2.18).

This is well reproduced by the two-species rate equation model (Eq. 2.12, Fig. 2.18). Modification of single parameters reveals the cause of the power difference: Lasers from wafer C1340-6-3 have higher intra-cavity losses α and
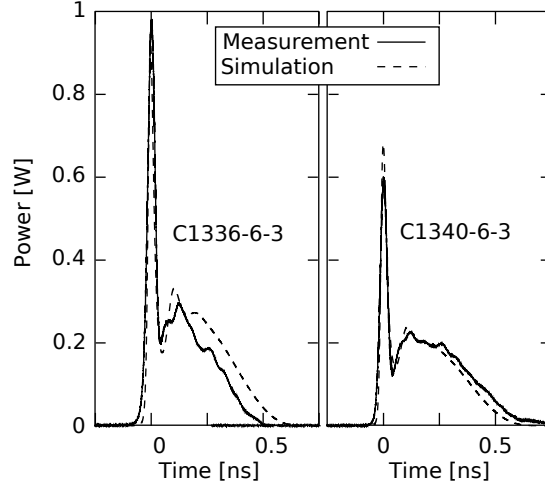
Figure 2.18: Spectrally integrated pulse shapes of gain switched DFB lasers at 330 K; photodiode measurement and simulated pulse shape (sum of Bragg and FP contributions). At these settings, both laser types emit more than 95% of the pulse energy at the Bragg wavelength.

lower facet losses $\tau_{R,B}^{-1}$, both caused by the higher DFB coupling coefficient. This redistribution of losses reduces the amplitude of the first relaxation oscillation, even at nearly constant total photon lifetime ($\tau_{S_B} = 3.1$ ps for wafer C1336-6-3 and $\tau_{S_B} = 3.4$ ps for wafer C1340-6-3). Therefore, the higher spectral selectivity and the reduced pulse peak power of the latter are indeed caused by the same underlying design feature, the stronger DFB coupling.

The competition between Fabry-Pérot and Bragg modes is also reproduced well by the presented model. (Fig. 2.19). The presented experimental pulse shapes for wafer C1336-6-3 are spectral integrals of the streak camera images of Fig. 2.16, with the FP-modes and the Bragg mode integrated separately. At 290 K, both the experimental and the simulated laser pulses consist only of Fabry-Pérot modes. At 310 K, the FP-modes are restricted to the first relaxation oscillation, with the after-pulse dominated by the Bragg mode. At 330 K, the Bragg mode dominates over the whole pulse duration. For a more detailed listing of measured and simulated pulse peak powers P_{max} and percental energy in the Bragg mode E_B/E_p see Tab. 2.4.

The simulated energy fraction in the Bragg mode shows a stronger temperature dependence than observed experimentally. However, this behavior is very sensitive on slight parameter variations, and even neighboring laser diodes from the same wafer show significant variation in the crossover region.
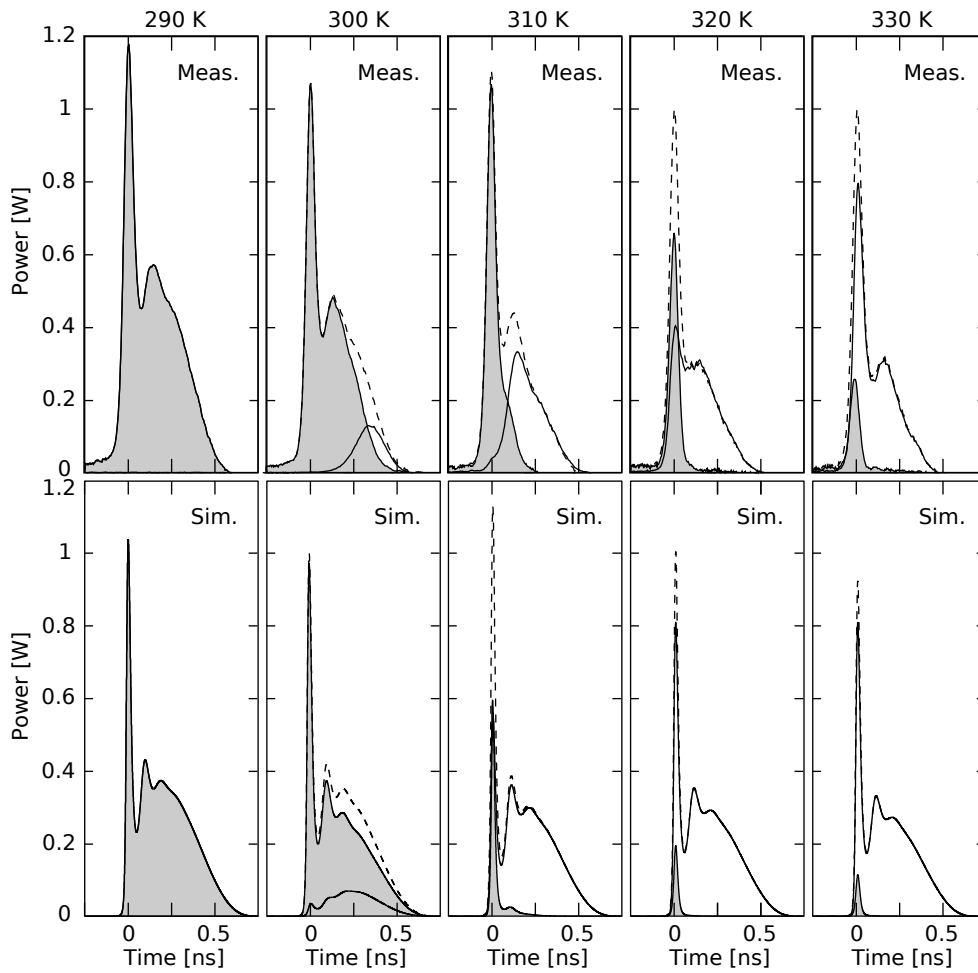
Figure 2.19: Pulse shapes of laser C1336-6-3 020410 at different heat sink temperatures. shaded: FP-modes, empty: DFB-modes, dashed: total pulse shape. Top: Pulse shapes measured with streak camera, bottom: simulation

T		C1336-6-3		C1340-6-3	
		Meas.	Sim.	Meas.	Sim.
290 K	P_{max} [W]	1.17 ± 0.06	1.03	0.85 ± 0.04	0.94
	$E_{\mathrm{B}}/E_{\mathrm{p}}$	0.11 ± 0.10	0.00	0.89 ± 0.04	0.49
300 K	P_{max} [W]	1.07 ± 0.05	1.00	0.86 ± 0.04	0.97
	$E_{\mathrm{B}}/E_{\mathrm{p}}$	0.52 ± 0.08	0.15	0.98 ± 0.01	0.91
310 K	P_{max} [W]	1.11 ± 0.06	1.13	0.77 ± 0.04	0.78
	$E_{\mathrm{B}}/E_{\mathrm{p}}$	0.73 ± 0.03	0.86	0.99 ± 0.01	0.99
320 K	P_{max} [W]	1.05 ± 0.05	1.00	0.71 ± 0.04	0.73
	$E_{\mathrm{B}}/E_{\mathrm{p}}$	0.89 ± 0.03	0.95	1.00 ± 0.00	1.00
330 K	P_{max} [W]	1.05 ± 0.05	0.97	0.59 ± 0.03	0.68
	$E_{\mathrm{B}}/E_{\mathrm{p}}$	0.97 ± 0.01	0.97	1.00 ± 0.01	0.99

Table 2.4: Simulated and measured pulse peak powers and fraction of the pulse energy in the Bragg mode for several device temperatures

2.4.4 Numerical Optimization of Distributed Feedback Lasers for Gain-Switching

The good agreement between the presented model and the experimental picosecond dynamics of gain switched laser diodes allows predictions regarding the optimum laser design for this application. Starting from the parameters for wafer C1340-6-3, the influence of the Bragg coupling coefficient κ is investigated at 300 K (Fig. 2.20). This leads to a simultaneous variation of the Petermann factor K and the internal photon losses α. The latter was estimated from the presented experiments to be $\alpha_0 \approx 0.32 + 0.092\kappa$. As expected, lasers with higher coupling coefficient generate pulses with higher spectral purity, but a lower peak power.

A variation of the resonator length at constant κ and constant peak current density gives a similar result (Fig. 2.21). Longer laser diodes show higher output power but lower spectral purity, even though κL increases. This leads to lower facet losses for the Bragg mode. However, according to Eq. 2.4, the facet losses for the Fabry-Pérot modes also decrease with resonator length. For long laser diodes, the photon lifetime is therefore dominated by internal losses and becomes more similar for the two photon species (Eq. 2.7). This favors the FP-modes, since they have the higher modal gain. As shown experimentally, the wavelength difference $\Delta\lambda_0$ between Bragg-wavelength and gain maximum decisively influences the dynamic spectrum of gain switched DFB lasers. Our model easily allows the variation of the Bragg wavelength at constant device temperature (Fig. 2.22). For $\kappa = 2.2\,\mathrm{cm}^{-1}$ a high spec-
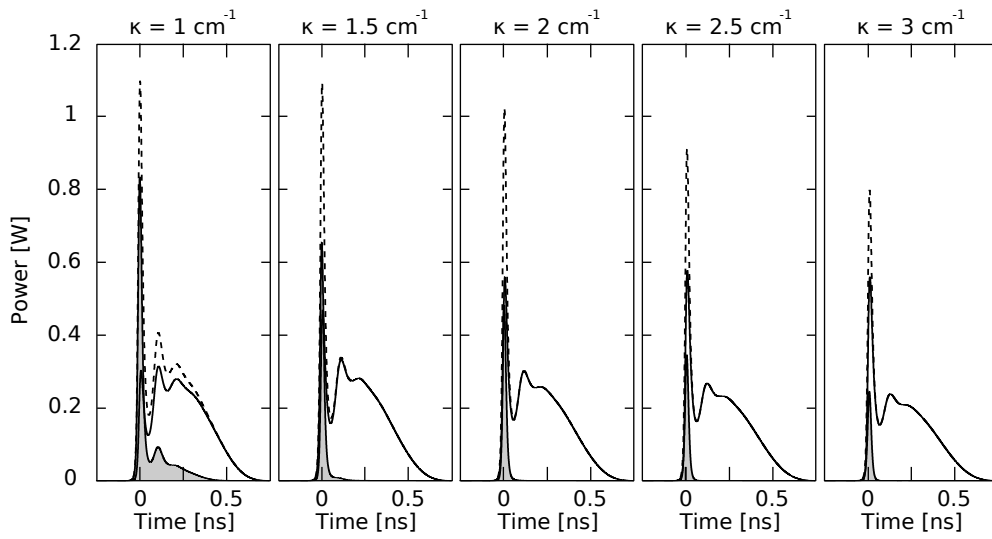
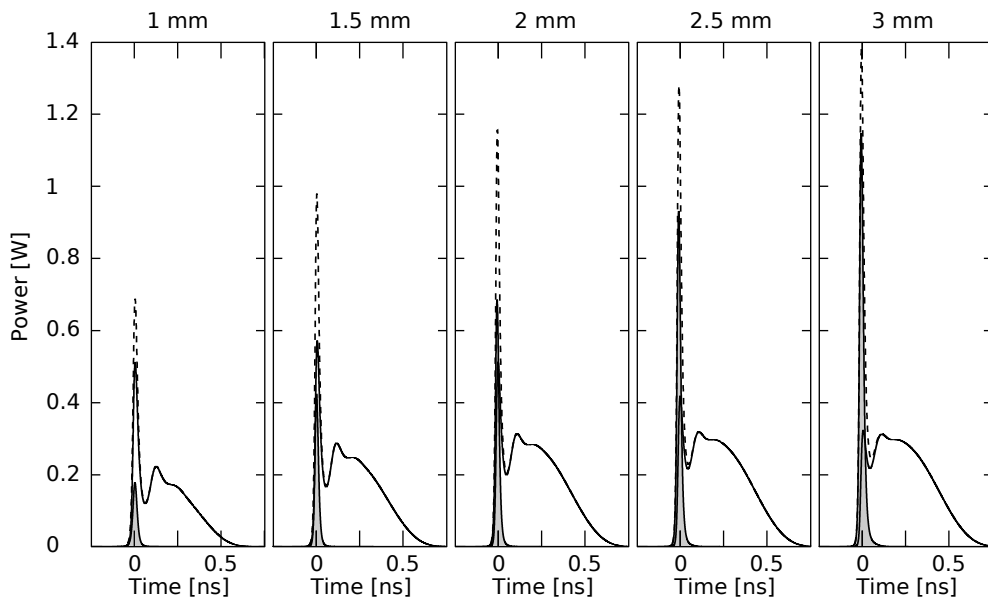Figure 2.20: Simulation of gain switching at various coupling coefficients, K and α_0 were varied accordingly.

Figure 2.21: Simulation of gain switching with various diode lengths. $I_{\max}$ was varied to keep the peak current density constant at $6140\,\mathrm{A\,cm^{-1}}$.
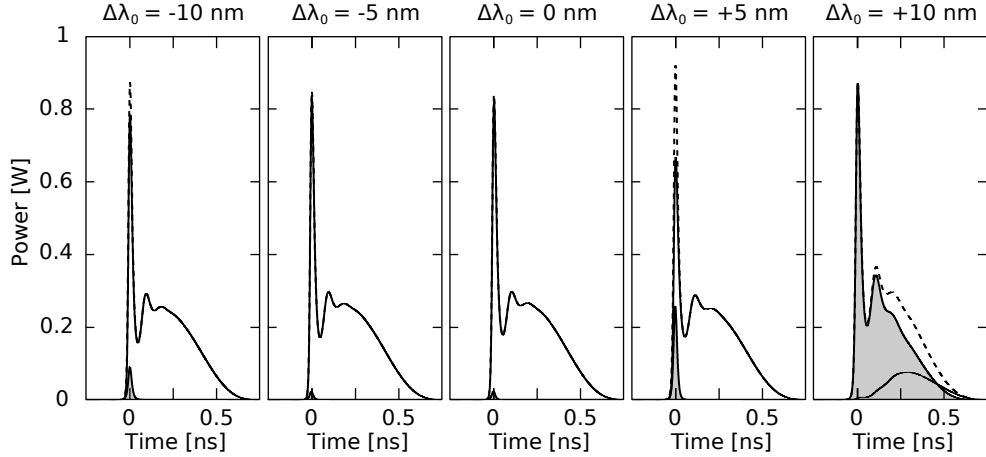
Figure 2.22: Simulation of gain switching at various wavelength differences between Bragg-wavelength and gain maximum. For $\Delta\lambda_0 > 0$, the Bragg wavelength is longer than the wavelength of maximum gain.

tral purity of $E_{\mathrm{B}}/E_{\mathrm{p}} \geq 0.98$ is obtained for -10 nm$< \Delta\lambda_0 <$0 nm, when the Bragg wavelength is shorter than the wavelength of the gain maximum. This is in good agreement with previously published experimental results [122]. At $\Delta\lambda_0 = -5$ nm, a small coupling coefficient of $\kappa = 1.2$ cm^{-1} suffices to ensure the desired spectral purity of $E_{\mathrm{B}}/E_{\mathrm{p}} = 0.98$, and a peak power of 1.02 W is reached in our simulation.

In this section, the picosecond spectral dynamics of gain switched DFB lasers has been studied both experimentally and theoretically. In the experiment, the influence of the device temperature has been investigated for CW-optimized laser diodes. For a low coupling coefficient of $\kappa L = 0.14$, qualitatively different spectral dynamics is found at different temperatures. At room temperature, the pulse is dominated by residual Fabry-Pérot modes with a broad spectrum. A high spectral purity with 95% of the pulse energy in the Bragg mode is only reached at a temperature of 330 K. At this setting, pulses with a duration of less than 70 ps and a peak power of more than 1 W have been generated.

Lasers with higher coupling coefficient of $\kappa L = 0.33$ emit dynamically single-mode at much lower temperatures. However, they also have a significantly reduced peak power due to the higher facet reflectivity and higher radiation losses from the second-order grating. At room temperature, the peak power is 0.86 W at a spectral purity of $E_{\mathrm{B}}/E_{\mathrm{p}} = 0.98$.

All these features are successfully simulated using a rate-equation model. The excellent agreement enables the use of the model for further optimization

of DFB lasers for the generation of intense narrow-band picosecond pulses. Optimum values for the coupling coefficient ($\kappa = 1.2\,\text{cm}^{-1}$), the resonator length ($L = 1.5\,\text{mm}$), and the wavelength difference between gain maximum and Bragg line ($\Delta\lambda_0 = -5\,\text{nm}$) are found. These should enable the generation of pulses with peak powers greater than $1\,\text{W}$ at room temperature with excellent spectral purity.

Chapter 3

Optical Amplification of Picosecond Pulses

3.1 Single-Pass Optical Amplification

As reported in the previous chapter, gain switched diode lasers find a wide range of applications which require variable repetition rates and low-cost compact light sources. However, pulses from gain switched ridge-waveguide lasers typically have pulse energies below 100 pJ with peak powers up to 1 W. This is not sufficient for a number of applications. In material processing, for example, peak powers of at least several hundred watts are required [58]. Furthermore, nonlinear frequency conversion of infrared pulses allows the generation of flexible picosecond laser pulses in the yellow-green gap, which are highly needed in fluorescence lifetime spectroscopy [126]. In order to generate the required pulse energies on the order of 100 pJ in the visible spectral range, infrared input peak powers of several watts are typically required [127–129].

The most established method to generate such high peak powers is the master oscillator-power amplifier (MOPA), consisting of a gain switched seed laser diode and one or more amplification stages. The choice of the most suitable setup and gain medium sensitively depends on the desired output specifications, particularly on pulse repetition rate and peak power. This section gives an introduction to laser amplifiers that are particularly suitable for the amplification of variable pulse signals and compare different active media which provide gain around 1060 nm.

3.1.1 Introduction to Laser Amplifiers

Optical power amplifiers are frequently used to separate the generation of high optical power from the compliance with more specific requirements, such as narrow linewidth [130], wavelength tunability [131], or picosecond pulsed operation [63, 127, 132–136]. These "difficult" beam characteristics can be
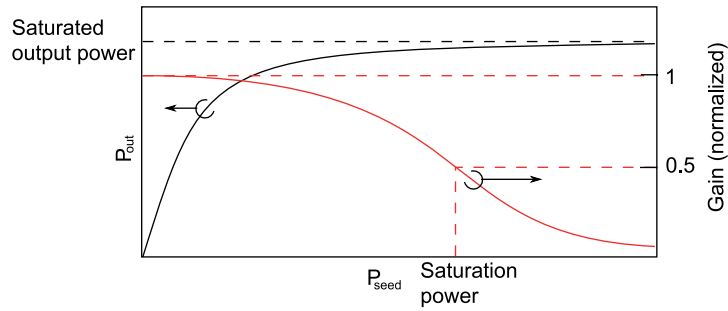
Figure 3.1: When the seed power P_{seed} of an amplifier is increased at constant pump power, a saturation of the amplified output power P_{out} is observed. This is equivalent to a decrease of the net gain $P_{\text{out}}/P_{\text{seed}}$. The input power at which the saturated gain drops to half the small signal gain is called the saturation power.

generated in a low-power seed laser, whose output is then amplified to higher power while keeping the beam characteristics unchanged.

Most optical amplifiers are *laser amplifiers* [137–140], in which amplification is based on stimulated emission. Accordingly, the same gain media as for lasers are available. In addition to laser amplifiers, there also exist *nonlinear amplifiers* such as optical parametric amplifiers [141] or Raman amplifiers [142] that generate gain from different physical mechanisms. However, these are mainly applied at wavelengths where laser gain media are unavailable, or in optical telecommunication networks, in which the transmission fiber itself can act as a Raman gain medium.

The *net gain* of an amplifier is defined as the ratio between output power P_{out} and seed power P_{seed}. If the seed power P_{seed} of a laser amplifier is small, the inversion of the gain medium remains approximately unchanged after passage of the pulse and the gain is at its maximum. This is called the *small signal gain* (Fig. 3.1). In this regime, the output power is limited by the available seed power and cannot be increased by further pumping since the energy stored in the gain medium is not extracted efficiently.

If the seed power is increased, the output power begins to saturate and the net amplifier gain decreases [132, 133, 143, 144]. The *saturation power* is defined as the seed power at which the saturated gain is half of the small signal gain. In the saturated regime, a significant fraction of the stored energy is extracted from the gain medium, and the output power depends strongly on the pump power while the influence of the seed power is low.

Technologically, it is often desirable to run an optical amplifier in saturation in order to maximize the wall-plug efficiency. However, inhomogeneous

saturation over the beam cross section can lead to a deterioration of the beam quality [145]. Similarly, if a pulsed signal is used, temporal variation of the gain saturation can distort the pulse shape (see Fig 3.9 for an experimental example).

Depending on the available seed and pump energies and the gain material, several amplifier architectures are in wide use. In *Single-pass amplifiers* [137, 138], the seed signal traverses the gain medium only once. This architecture is least sensitive in terms of alignment and is favorable for gain media with a high small signal gain and a low saturation power. In this case, gain saturation can be achieved in a single amplifier pass. Since the interaction time between seed signal and gain medium is short, single-pass amplifiers are suitable for high pulse repetition rates and CW signals, but the achievable net gain is fairly low.

Higher in complexity are *multi-pass amplifiers* [139, 141], in which a number of folding mirrors sends the signal light through the gain medium multiple times. For active media with low material gain (e.g. solid state laser crystals) this can increase the net amplifier gain for pulsed signals. For maximum gain, the pulse interval has to exceed the dwell time of one pulse in the amplifier, which typically limits multi-pass amplifiers to megahertz repetition rates.

The complexity of the optical setup limits the number of passes achievable with multi-pass amplifiers. For some applications, especially when the stimulated emission cross section is low, this does not suffice to saturate the amplifier. In this case, *regenerative amplifiers* [140] can achieve a very high net gain for pulses with repetition rates in the kilohertz range. Here, the amplifier gain medium is enclosed in an optical resonator. After pumping the amplifier for a while, one seed pulse is coupled into the resonator, typically using an electro-optical switch. The pulse is then allowed to cycle in the resonator until the gain is saturated, before it is switched out of the resonator. This amplifier architecture is popular for the amplification of femtosecond pulses with a Ti:Sapphire gain medium and allows the highest peak output powers of several $10\,\mathrm{GW}$ [140].

Especially in laser amplifiers with high single-pass gain, weak parasitic reflections can cause *self-lasing* of the amplifier. This can severely damage the amplifier components or the seed laser, especially if it occurs in the form of short laser pulses. Even without parasitic reflectances, amplified spontaneous emission (ASE) can extract a substantial amount of energy from the amplifier and frequently limits the achievable energy storage [136, 144]. If very high output powers are required, it is often favorable to use multiple amplifier stages. This allows the insertion of spectral filters or optical isolators between the stages in order to prevent self-lasing and limit ASE [63, 136].

This thesis contains a comparison two gain media that are well suited for

single-pass operation at 1060 nm, namely a semiconductor tapered amplifier and an ytterbium-doped fiber amplifier for the amplification of gain switched picosecond pulses.

3.1.2 Gain Media at 1060 nm

Laser amplification at around 1060 nm is widely used for material processing and for frequency conversion into the yellow-green spectral range. Application is facilitated by the availability of several gain materials for this wavelength. Neodymium-doped crystals such as Nd:YAG provide narrow-band gain at specific wavelengths [146]. Due to the bulk crystal geometry, their single-pass gain typically is fairly low, and they are frequently used in multi-pass setups [139].

Neodymium- or ytterbium-doped glasses, on the other hand, have inhomogeneously broadened gain spectra, providing more flexibility in the choice of the master oscillator. Moreover, they can be manufactured as single-mode fibers, whose high photon density and long interaction length leads to a high single-pass gain. Compared to neodymium, ytterbium has a lower quantum defect, which lowers the thermal load on the material. Furthermore, pump laser diodes are more efficient at the ytterbium pump wavelength of 975 nm than at the 808 nm required by Nd:glass. Therefore, ytterbium-doped fibers are the medium of choice for high-gain, high-power fiber amplifiers at 1060 nm [147].

In addition, semiconductor quantum well structures can provide high gain at around 1060 nm with high flexibility regarding the center wavelength (Sec. 2.1.1.1).

3.1.2.1 Ytterbium-doped Optical Fibers

Fiber amplifiers consist of a length of optical fiber doped with rare earth ions. At 1060 nm, the most common dopant is Yb^{3+}, which has a broad peak in its emission spectrum around 1030 nm (Fig. 3.2). Yb:glass requires optical pumping, ideally around the absorption maximum at 976 nm. It can be implemented longitudinally as either core- or cladding-pumping [148], or occasionally in a transverse geometry, using laser diodes as the pump source.

Using a multi-stage setup combining core and cladding pumping, a peak power of 250 kW has been reached at 500 kHz starting from a gain switched laser diode as seed [149]. Using an ytterbium-doped photonic crystal fiber for an even larger mode area, pulses with a duration of 110 fs and a peak power of 150 MW have been generated at 1 MHz repetition rate [150]

Figure 3.2: Absorption (solid) and emission (dotted) spectra of Yb^{3+} in germanosilicate glass. Image taken from [137].
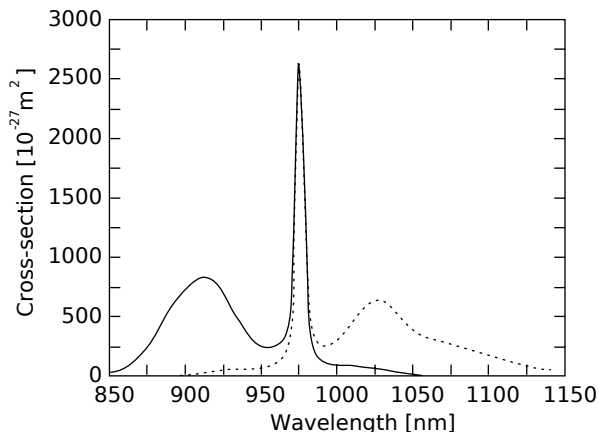
As compared to semiconductor gain media or bulk ytterbium-doped systems, fiber amplifiers can show a very high total gain of up to several tens of decibels [137,151]. This is due to the fiber geometry, which allows high photon densities over a large interaction length. In order to avoid destructive self-lasing, fiber amplifiers typically consist of a chain of lower-gain amplifiers with optical isolators and/or ASE filters in-between. In addition, many high-gain ytterbium-doped fiber amplifiers (YDFAs) contain an electronic interlock to ensure that the amplifier can only be pumped when the seed light is present.

An advantage of ytterbium doped gain media for the amplification of laser pulses is the long upper state lifetime of about 1 ms [151]. This means that large energies of several microjoule can be stored in a single-mode fiber, and long intervals between seed pulses are acceptable. However, for the megahertz repetition rates required for fluorescence lifetime spectroscopy, pulse intervals are more than four orders of magnitude smaller than the time constant of spontaneous emission. This means that the gain cannot recover completely in-between pulses and depends on the pulse repetition rate [152]. On the other hand, the ASE power generated in the pulse intervals is low, so the requirements for ASE suppression are less stringent for megahertz signals (Sec. 3.2.1).

A typical problem in highly ytterbium-doped fibers is *photodarkening*, a rise in absorption centered at visible wavelengths that is induced by the pump light. Investigation into the causes of photodarkening is ongoing, but changes in the chemical bonds in clusters of ytterbium ions seem to play a role [153, 154]. Photodarkening can be reduced by suitable fiber production processes that ensure a very homogeneous distribution of the ytterbium ions in the glass host [153]. Although reversal of photodarkening by heating [155] or illumination with ultraviolet light [156] is possible, practical fiber amplifier systems usually treat photodarkening as part of the burn-in process.

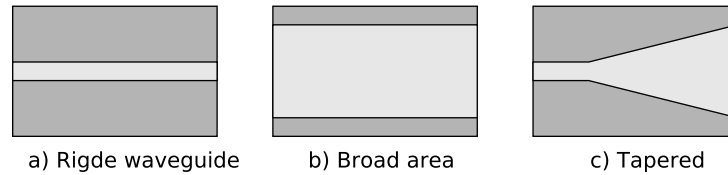a) Rigde waveguide   b) Broad area   c) Tapered

Figure 3.3: Lateral layouts of semiconductor optical amplifiers

Nonlinearities in fiber amplifiers are mainly due to self-phase modulation and stimulated Raman scattering. In single-mode fibers with a mode-field diameter of few micrometers, nonlinear processes become relevant at peak powers in the kilowatt range [157].

3.1.2.2 Semiconductor Quantum Wells

Just as for laser diodes, the gain medium of modern edge-emitting semiconductor optical amplifiers (SOAs) consists of one or more quantum wells embedded in a vertical waveguide structure (Sec. 2.1.1). In contrast to semiconductor lasers, both facets have to be anti-reflection (AR) coated and possibly cut at an angle in order to avoid parasitic feedback into the amplifier. Semiconductor amplifiers have the same advantages as laser diodes, namely a compact size, no moving parts, and the possibility for electrical pumping. They can also be produced from the same wafer as the seed laser, ensuring perfectly matched gain spectra.

Different lateral layouts are advantageous depending on the application (Fig. 3.3). *Ridge-waveguide amplifiers* guide light in a single transverse mode, so the amplified beam has a very high quality. However, due to the small active volume, only low net gains of below 10 dB can be reached [136]. Furthermore, the facet load is high and the saturation power low [133, 143, 158], limiting the maximum output power. These properties make ridge-waveguide amplifiers primarily suitable as pre-amplifiers in multi-stage systems, or for low-power applications such as telecommunications.

The active region of *broad-area amplifiers* has a lateral extension of 30–500 µm and only weak gain guiding is present in this direction. Ideally, the seed beam has to be astigmatic, such that the focus in vertical direction is on the front facet of the amplifier while the focus in lateral direction is in the center of the amplifier. This will allow the beam to be guided in the vertical waveguide and optimize the overlap with the pumped area in lateral direction. Still, large parts of the pumped area will not be depleted by the seed beam and cause ASE and device heating. The resulting thermal lensing [159, 160] and filamentation [161] leads to a degradation of the beam quality. On the

other hand, the large volume of the active zone allows for high net gains of above 20 dB if thermal problems can be avoided [162].

Semiconductor *tapered amplifiers* [138] allow a compromise between the aforementioned geometries. Similar to broad-area lasers, the active volume is large and high gains of above 20 dB [163] and saturation energies above 100 pJ can be reached [134]. Modern tapered amplifiers include an RW section that acts as a mode filter and pre-amplifier for the incoming seed. The geometry of the subsequent tapered section follows the free-space expansion of the RW mode, thus optimizing the overlap with the pumped volume. This reduces thermal load and increases the beam quality of the amplified output beam. 5.5 W of CW output power have been reached at a beam quality of $M^2 = 1.5$ [164], making tapered amplifiers an excellent high-brightness laser source.

In contrast to ytterbium-doped gain media, semiconductor optical amplifiers have a short upper-state lifetime of few nanoseconds [165]. Therefore, for seed pulse repetition rates in the megahertz range, a significant proportion of excited electrons will recombine spontaneously in the pulse intervals and produce a CW background of amplified spontaneous emission. On the other hand, the short time scale of the dynamical processes enables the amplifier to reach equilibrium within each seed pulse interval [136, 152]. For this reason, the amplified pulse energy is expected to be independent of the repetition rate and the exact pulse arrival time for repetition rates in the megahertz range.

Semiconductor amplifiers also suffer from the same nonlinearities as pulsed laser diodes when used with laser pulses, especially spectral hole burning and carrier heating. For picosecond pulses, these gain compression mechanisms typically become relevant at peak powers of a few watts [158, 166, 167].

In this section, various amplifier geometries and gain media have been presented. For high-gain materials, amplifiers in single-pass geometry are suitable and offer great flexibility for the seed signal. However, care has to be taken to suppress parasitic lasing arising from small feedback into the amplifier.

Attractive gain media in the spectral range around 1060 nm are ytterbium-doped fibers and semiconductor tapers. The former have to be optically pumped and have a long upper-state lifetime of about 1 ms. This means that the gain will depend on the signal repetition rate in the megahertz range. The semiconductor medium, on the other hand, has an upper-state lifetime of only few nanoseconds. Therefore, it should perform independently of the repetition rate, but the gain will be limited due to ASE.
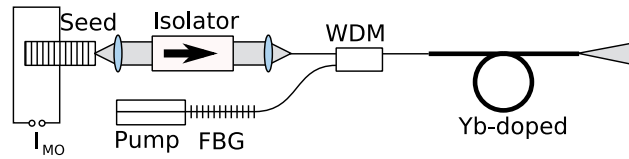
Figure 3.4: Setup of the ytterbium-doped fiber amplifier studied in this thesis

3.2 Optical Amplification of Picosecond Pulses

This section compares two amplifier technologies, an ytterbium-doped fiber and a semiconductor taper, regarding their suitability to amplify sub-100 ps pulses.

The presence of ASE in the pulse intervals makes the determination of the amplified pulse energy not straightforward. Spectral discrimination is possible, but reaches good precision only when several signal repetition rates are considered, as demonstrated for the semiconductor tapered amplifier.

3.2.1 Ytterbium-doped Fiber Amplifiers

As an example of an ytterbium-doped fiber amplifier, a single stage core-pumped design is studied (Fig. 3.4). The active medium consists of 50 cm of highly ytterbium-doped double-clad polarization-maintaining fiber, with a mode field diameter of 6 µm. To exclude the effects of photodarkening, the fiber was aged for several hours before the pulse amplification experiments.

The pump diode is a commercial Fabry-Pérot laser diode which emits a maximum of 500 mW at 975 nm in a single transverse mode. It is packaged in a butterfly housing and butt-coupled to a fiber Bragg grating (FBG) to ensure wavelength stability. The housing temperature is kept constant at 295 K. The seed pulses are generated by a laser diode from wafer C1336-6-3 at 325 K (see Sec. 2.1.3 and 2.4) at repetition rates between 2.5 MHz and 80 MHz. They have a duration of (53 ± 5) ps FWHM, an energy of (115 ± 3) pJ and a peak power of (0.71 ± 0.06) W with more than 95% of the pulse energy emitted in a single longitudinal mode at 1067.04 nm.

The pump light and the seed pulses are combined in a wavelength division multiplexer (WDM) and coupled into the active fiber in a forward-pumping scheme (Fig. 3.4). The coupled pump power reaches a maximum of (445 ± 15) mW. The seed pulses are coupled into the WDM using a free-space setup consisting of a 8 mm asphere, a two-stage optical isolator and a Schäfter-und-Kirchhoff fiber coupler. Behind the isolator, a pulse energy of 102 pJ and a
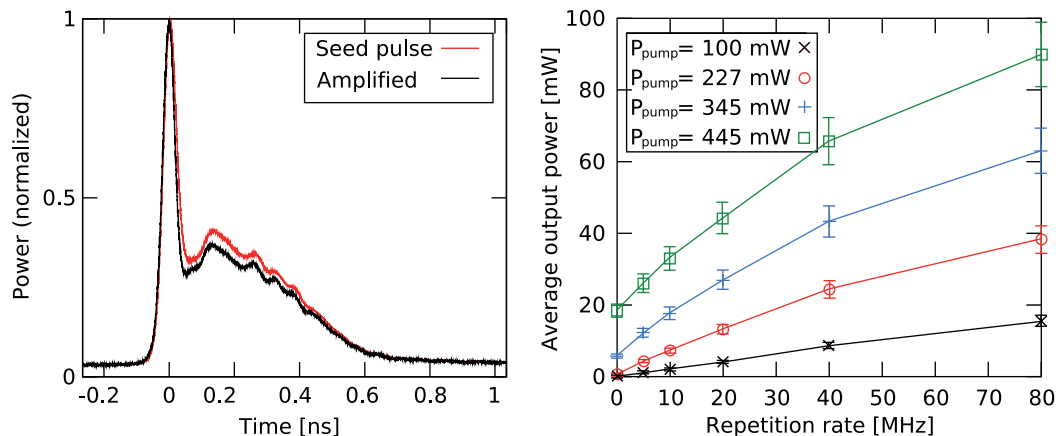
Figure 3.5: Amplification of picosecond pulses using a single-stage core-pumped YDFA. Left: Pulse shape before and after amplification with a coupled pump power $P_{pump} = 445$ mW. Right: Average output power as a function of seed pulse repetition rate for various pump powers. Repetition rate 0 corresponds to the output of the unseeded amplifier (ASE).

peak power of (0.63 ± 0.04) W were measured. The measurement equipment is described in Sec. 2.4.2.

At a repetition rate of 5 MHz and a coupled pump power of (445 ± 15) mW, this setup generates an amplified pulse energy of approximately (1.50 ± 0.05) nJ with a peak power of (8.3 ± 0.5) W. This corresponds to a net gain of 10.7 dB. The pulse shape remains nearly unchanged during amplification (Fig. 3.5, left), indicating that the amplifier is not saturated by the seed pulses. At this setting, the amplifier emits (18.6 ± 0.6) mW of ASE when left unseeded.

When the seed pulse repetition rate is increased, the average output power of the fiber amplifier rises less than linearly (Fig. 3.5, right). Here, repetition rate 0 corresponds to the unseeded amplifier. This behavior can be observed even at low pump currents at which the ASE power of the unseeded amplifier is below 1 mW. This means that the sublinear increase in total power is indeed due to a lower amplified pulse energy and not only to a decrease in ASE power. This is caused by incomplete gain recovery in the seed pulse intervals [132], as expected for a gain medium with a long upper state lifetime.

Using cladding pumping or multi-stage setups, much higher gain can be achieved in ytterbium-doped fiber amplifiers [168]. However, the qualitative features seen in this work remain valid, namely that gain recovery depends on the repetition rate in the megahertz range, and that gain switched seed pulses with peak powers below 1 W cannot saturate an ytterbium doped fiber.
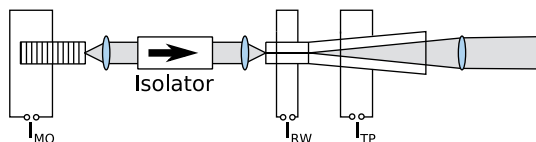
Figure 3.6: Setup of the semiconductor MOPA. The power amplifier consists of a ridge-waveguide (RW) and a taper (TP) section that can be pumped separately.

3.2.2 Semiconductor Tapered Amplifiers

Compared to fiber amplifiers, semiconductor amplifiers show the greater potential for miniaturization and their performance promises to be independent of the seed pulse repetition rate in the megahertz range due to their short upper state lifetime (Sec. 3.1.2.2).

3.2.2.1 Setup

In this work, a double quantum well InGaAs/ GaAsP traveling-wave optical amplifier (B1070-3 020312) is used. It consists of a 1 mm long ridge-waveguide (RW) part and a tapered (TP) section of 3 mm length with an taper angle of 6°. The RW and the tapered section have separate electrical contacts and can be pumped with different currents I_{RW} and I_{TP} (see Fig. 3.6). For easier access to the metalization pads, the amplifier is mounted p-side-up, which, however, leads to lower heat dissipation. To avoid thermal rollover, the amplifier was kept at a constant temperature of 293 K and a maximum taper current of 3.9 A is used. At this temperature, the gain maximum is at 1068.5 nm.

In preparation of the following miniaturization experiments (Sec. 3.3), a seed diode from wafer C1340-6-3 (Sec. 2.1.3 and 2.4) at 325 K is used with this amplifier. It generates pulses with a duration of (39 ± 5) ps, an energy of (105 ± 4) pJ and a peak power of (620 ± 30) mW. More than 99% of the pulse energy are emitted in a single longitudinal mode centered at 1063.02 nm. For comparison with the YDFA, experiments are also performed using a seed laser diode from wafer C1336-6-3 with similar results (Summary see Tab. 3.1). Again, repetition rates in the range between 2.5 MHz and 80 MHz are considered.

The cross section area of the amplifier ridge waveguide is larger than that of the seed laser diode at 2.7 μm×3.0 μm. This ensures good input coupling using a one-to-one imaging setup. The light from the master oscillator (MO) is collimated with an aspheric lens with 8 mm focal length, passed through
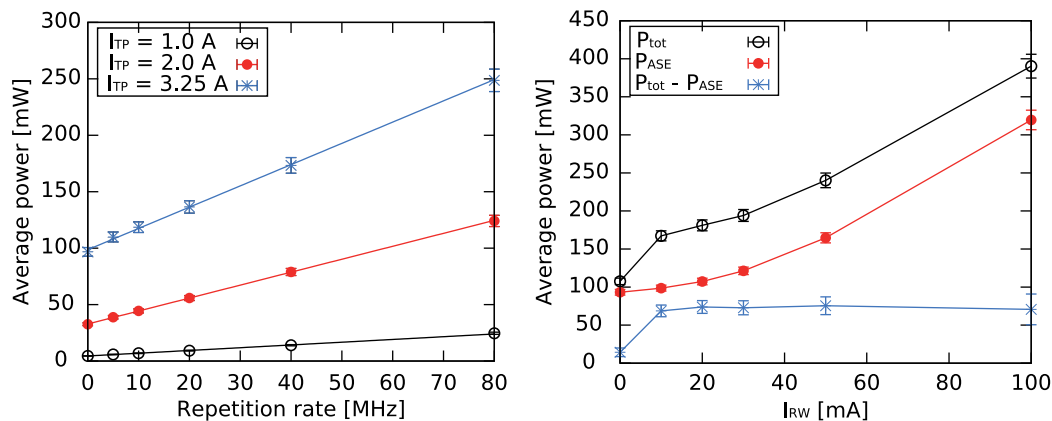
Figure 3.7: Average output power of the semiconductor MOPA using a seed diode from wafer C1340-6-3. Left: As a function of seed pulse repetition rate at $I_{\mathrm{RW}} = 10\,\mathrm{mA}$ and various taper currents. Repetition rate 0 signifies the unseeded amplifier. Solid lines are linear fits. Right: as a function of RW section current at $I_{\mathrm{TP}} = 3.25\,\mathrm{A}$ and $40\,\mathrm{MHz}$ repetition rate. The amplified pulse power saturates above transparency. Lines are guides to the eye.

a two-stage optical isolator and focused into the ridge waveguide part of the power amplifier (PA) with another $8\,\mathrm{mm}$ asphere. After passage through the optical isolator, the seed pulse energy is $(71 \pm 0.02)\,\mathrm{pJ}$ and the peak pulse power $(0.42 \pm 0.03)\,\mathrm{W}$ for the seed laser diode from wafer C1336-6-3.

Following the theoretical treatment given in [158], the saturation energy for the RW section of our amplifier is calculated to be approximately $2\,\mathrm{pJ}$, much smaller than the effective seed pulse energy of $(71 \pm 0.02)\,\mathrm{pJ}$. The tapered section has a saturation energy of approximately $120\,\mathrm{pJ}$. The measurement devices are described in Sec. 2.4.2.

3.2.2.2 Pulse Shape and Energy

Due to the short upper-state lifetime in semiconductor amplifiers (Sec. 3.1.2.2), the amplified pulse energy E_{p} is expected to be independent of the seed pulse repetition rate. Since the amplifier runs in saturation, its gain is depleted after the passage of a signal pulse, and the ASE power is reduced for a short period of time (see inset in Fig. 3.8). If this reduction ΔE_{ASE} is also independent of the repetition rate, the average amplifier output power increases linearly with the pulse repetition rate f_{rep}:

$$P_{\mathrm{out}} = P_{\mathrm{ASE}} + f_{\mathrm{rep}} \cdot (E_{\mathrm{p}} - \Delta E_{\mathrm{ASE}}),$$

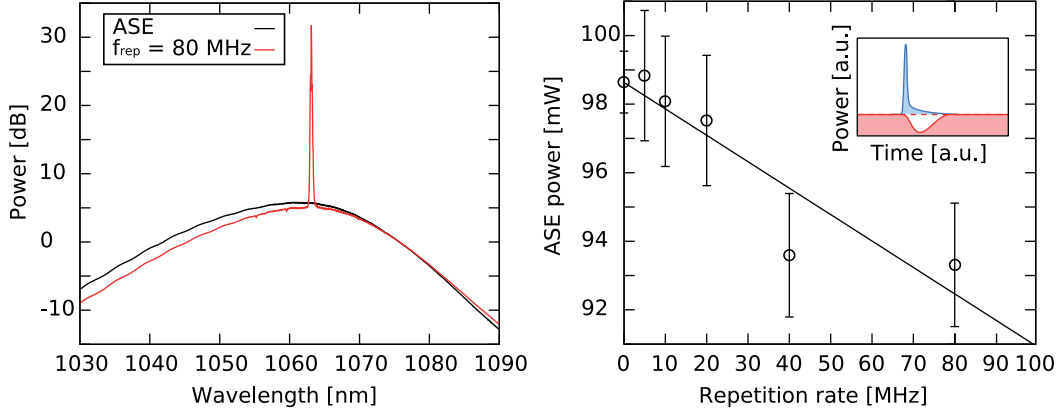where P_{ASE} is the output power of the unseeded amplifier.

Figure 3.8: Amplification of picosecond pulses (wafer C1340-6-3) using a SOA at I_{RW}=10 mA, I_{TP}=3.25 A. Left: Amplifier output spectra. Black: unseeded amplifier, red: amplifier seeded at 80 MHz. Note the decreased ASE of the seeded amplifier. Right: ASE power $P_{ASE} - f_{rep}\Delta E_{ASE}$ as a function of seed pulse repetition rate as determined by spectral integration. Inset: After passage of a seed pulse (blue) the amplifier gain is depleted and ASE power (red) decreases temporarily. Averaged ASE power is thus anti-proportional to the seed pulse repetition rate.

This is confirmed by the experiment for both seed lasers and a variety of pump currents (Fig. 3.7 left). Again, repetition rate 0 corresponds to the unseeded amplifier. The RW section current of 10 mA was chosen to be close to the transparency current. Above transparency, the amplified pulse energy saturates (Fig. 3.7 right) and the output pulse energy only depends on the taper current. This indicates that each incoming pulse fully depletes the taper section gain even if the RW section is close to transparency.

The increase in total amplifier output power for RW currents above transparency is entirely due to an undesirable increase in ASE. For RW currents above 50 mA and $I_{TP} = 3.25$A, the unseeded amplifier exhibits parasitic lasing, as observed in spectral measurements.

The slope of the amplifier output power as a function of the seed pulse repetition rate is a measure for the amplified pulse energy. Using the seed laser from wafer C1340-6-3, a slope $E_p - \Delta E_{ASE} = (1.88 \pm 0.06)$ nJ was measured for a taper current of 3.25 A. Clearly, this is only a lower bound for the true pulse energy [135]. The contribution of ΔE_{ASE} can be estimated from the amplifier output spectrum. Since the ASE has a spectral width of 22.5 nm FWHM with its peak at 1061.5 nm, its spectrum is flat over the width of the signal line (see Fig. 3.8 left). By replacing the signal peak by a horizontal

Figure 3.9: Normalized pulse shape before and after amplification with the SOA using a seed diode from wafer C1340-6-3 at I_{RW}=10 mA, I_{TP} =3.25 A. The leading peak suffices to deplete the amplifier gain and is over-represented in the amplified pulse shape.
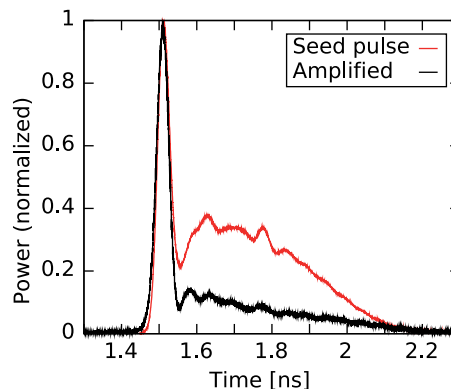
line, the ASE power can be estimated under seeded conditions. This approach neglects possible spectral hole burning, which seems justified since no dips in the ASE spectrum can be observed next to the signal line.

As expected, the ASE power of the seeded amplifier decreases linearly with the pulse repetition rate (Fig. 3.8 right). A linear fit yields a value of $\Delta E_{ASE} = (77 \pm 17)$ pJ for the reduction in ASE after amplification of one seed pulse. By adding this to the measured slope of $E_p - \Delta E_{ASE} = (1.88 \pm 0.06)$ nJ, a true pulse energy of (1.96 ± 0.06) nJ is obtained.

At $I_{RW} = 10$ mA and $I_{TP} = 3.93$ A, a record pulse energy of (3.13 ± 0.09) nJ is measured, limited by device heating. This exceeds all previous results from single-stage semiconductor MOPAs by more than a factor of two [63,127,135].

During amplification, the pulse spectrum remains unchanged, and 73% or (1.43 ± 0.07) nJ of pulse energy are contained in the central 200 pm of the spectrum.

The saturation of the amplifier leads to pulse deformation because the leading edge of the pulse experiences higher gain than the pulse tail (Sec. 3.1.1). For our gain switched seed pulses, this effectively suppresses the afterpulse (Fig. 3.9). The pulse length remains constant during amplification at about 40 ps FWHM. This results in a peak power of (28 ± 2) W at $I_{TP} = 3.93$ A, corresponding to a gain of 18.2 dB. Output pulse shapes are nearly independent of the taper pump current. Using the seed diode from wafer C1336-6-3, a pulse energy of (1.40 ± 0.04) nJ and a peak power of (16.1 ± 1.0) W are obtained at $I_{RW} = 100$ mA and $I_{TP} = 2$ A with a similar improvement of the pulse shape.

At I_{RW}=10 mA and I_{TP}=3.93 A, the ASE background of the unseeded laser is (170 ± 5) mW. This corresponds to a pulse extinction ratio of approximately 22 dB. However, for applications in time-resolved fluorescence, pulse contrast should exceed 40 dB in order to minimize noise on the fluorescence signal. This is easily achieved for SHG-based green pulse sources since the second harmonic

Amplifier	Semiconductor Taper		Yb-doped Fiber
Seed laser	C1336-6-3	C1340-6-3	C1336-6-3
Seed pulse energy	102 pJ	71 pJ	102 pJ
Seed peak power	0.63 W	0.42 W	0.63 W
Pump settings	$I_{RW} = 100\,\text{mA}$	$I_{RW} = 10\ \text{mA}$	Core pumping
	$I_{TP} = 2.0\,\text{A}$	$I_{TP} = 3.93\,\text{A}$	490 mA @ 975 nm
ASE (unseeded)	53 mW	170 mW	19 mW
Output pulse energy	1.40 nJ	3.13 nJ	1.50 nJ
Output peak power	16.1 W	28 W	8.3 W
Vert. beam quality	$M^2 = 1.5$		$M^2 < 1.2$
Horiz. beam quality	$M^2 \approx 6$		$M^2 < 1.2$
Miniaturization	Yes		Moderately
Power scaling	No		Yes, up to µJ
Pulse shape	Suppression of afterpulse		Unchanged
Gain depends on MHz rep. rate	No		Yes

Table 3.1: Overview of amplifier performance with gain switched seed

power depends on the square of the instantaneous fundamental power. Using the presented infrared pulse trains as fundamental, an extinction ratio better than 44 dB is expected for the green pulse source.

Using a bandpass filter with a transmission window of 1 nm FWHM, the beam quality of the pulsed amplifier can be measured almost independently of the ASE. Determining the beam diameter through the second moments of the beam profile, the beam propagation factor is measured to be $M^2 = 1.8$ in vertical direction, and $M^2 \approx 6$ in lateral direction. The lateral beam quality depends quite strongly on the coupling of the seed light, poor coupling not only reduces the amplified output power but also the beam quality. In contrast, the lateral beam quality of the ASE is $M^2 \approx 40$.

3.2.3 Comparison of Amplifier Technologies

In conclusion, both amplifier types have their specific advantages and disadvantages. The semiconductor tapered amplifier performs independent of the repetition rate in the megahertz range, improves the seed pulse shape and is very suitable for miniaturization. On the other hand, achievable output pulse energies are limited to few nanojoules due to the low saturation energy on the order of 100 pJ, and beam quality is often not diffraction limited.

Ytterbium-doped fiber amplifiers on the other hand are much more suitable for power scaling due to their much higher saturation energy. With multi-stage setups, pulse energies in the microjoule range have been reached [150]. However, the gain in ytterbium-doped fiber amplifiers depends on the signal repetition rate in the megahertz range, with higher output pulse energies at lower repetition rate. The signal pulse shape generally remains unchanged in the first amplifier stage.

For an overview of the properties and output parameters of the amplifiers discussed in this thesis, see Tab. 3.1.

3.3 Miniaturization

As for other technical devices, the miniaturization of laser sources has been the objective of substantial development efforts for many years [12, 13, 169, 170]. Not only do compact light sources more readily find application as parts of larger systems or as portable devices, they are also frequently mechanically and thermally more stable and cheaper to manufacture [12, 85].

Semiconductor lasers and amplifiers are particularly suitable for miniaturization because individual chips have a very small footprint. Furthermore, they can be electrically pumped, which minimizes the necessary number of optical elements. In this section, two types of compact semiconductor MOPAs are studied: the hybrid integrated semiconductor MOPA, in which microlenses are used to couple the master oscillator and the power amplifier on a micro-optical bench, and the monolithic semiconductor MOPA, which consists only of a single active element.

3.3.1 Hybrid Integrated Semiconductor Master Oscillator Power Amplifiers

Starting from a tabletop MOPA setup (Sec. 3.2.2), the most straightforward idea of miniaturization is to bring the master oscillator (MO) and the power amplifier (PA) close together and accomplish the optical coupling with microlenses. This allows the use of the same active elements as in the tabletop setup (Sec. 3.2.2) and makes the results directly comparable. Since a one-to-one imaging is necessary for good optical coupling, a single graded-index (GRIN) lens [171] is used (Fig. 3.10). Compared to an optical system consisting of multiple conventional lenses, such a setup contains fewer optical components and requires fewer assembly steps, making the finished module more robust and economical. However, an imaging system consisting of a single GRIN lens cannot contain an optical isolator. The challenge of this setup therefore is the suppression of spurious feedback using anti-reflection coatings only. In CW operation, this has been accomplished previously, and an output power of 4.5 W has been generated on a footprint of $2.5\times2.5\,\mathrm{cm}^2$ [169]. However, the suppression of parasitic reflections is more critical in pulsed operation, when the pulse intervals are long compared to the spontaneous emission lifetime (Sec. 3.1.2.2).

3.3.1.1 Setup and Assembly

For direct comparison to the tabletop setup (Sec. 3.2.2), our hybrid integrated picosecond MOPA contains the same active elements. The master oscillator
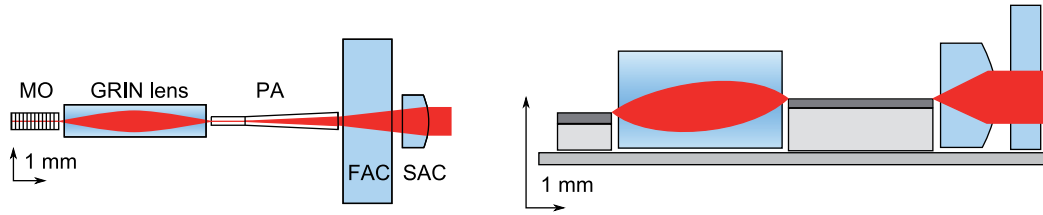
Figure 3.10: Scale drawing of the setup of the hybrid integrated semiconductor MOPA. Beam shaping optics are included on the micro-optical bench, consisting of a fast axis collimator (FAC) and a slow axis collimator (SAC).
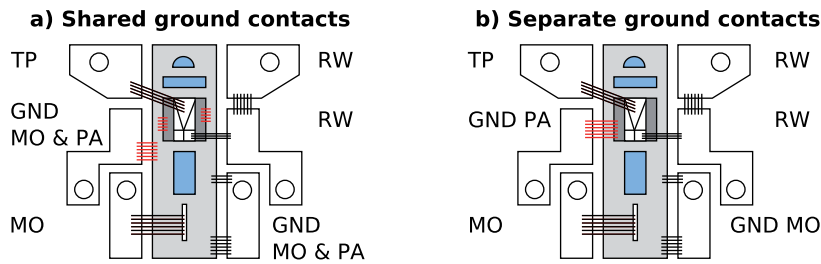

Figure 3.11: Bond schemes for the hybrid integrated MOPAs on CCP. Left: Shared ground contact for master oscillator and power amplifier. Right: Separate ground contacts for master oscillator and power amplifier.

is a 1.5 mm long DFB laser from wafer C1340-6-3, and the tapered amplifier from wafer B1070-3 has a total length of 4 mm. Different taper angles and taper lengths were studied (Tab. 3.2).

In the vertical direction, the beam heights of the active elements have to be carefully chosen. The beam height of the fast axis collimator can be varied only slightly by adjusting the glue thickness. To match its beam height of $(550 \pm 20)\,\mu$m, the tapered amplifier is mounted p-side-up on a 400 µm thick AlN submount with a gold contact layer (Fig. 3.10 b). The GRIN lens can compensate for height differences between master oscillator and amplifier, but again, the height of its optical axis is fixed at $(450 \pm 20)\,\mu$m . Accordingly, the master oscillator is mounted p-side-up on a CuW submount of 250 µm thickness. Both active elements are soldered onto a AlN micro-optical bench of size $5 \times 25\,\text{mm}^2$ using a FC150 flip-chip bonder. This way, the distance between master oscillator and power amplifier can be precisely adjusted to $(4737 \pm 1)\,\mu$m, which is the distance of the focal planes of the GRIN lens. The micro-optical bench is then mounted on a conduction cooled package (CCP).
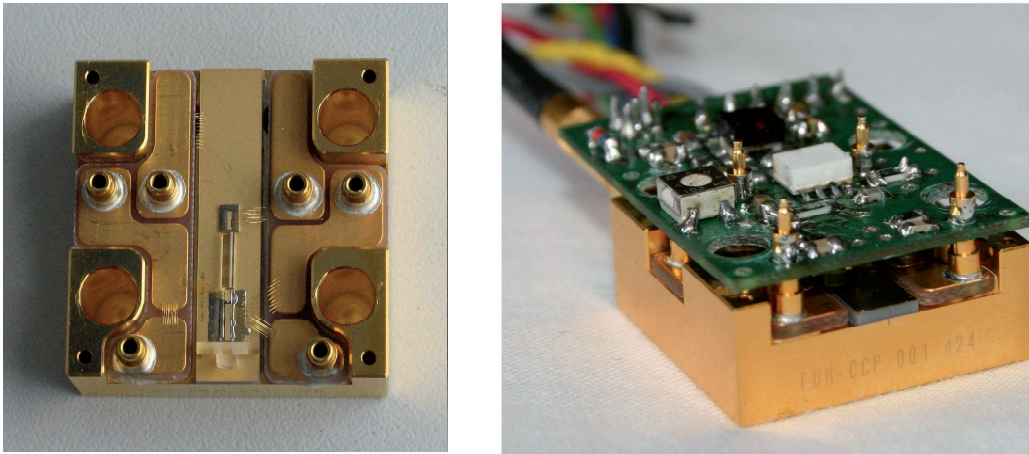
Figure 3.12: Hybrid integrated MOPA on a conductively cooled package (CCP) with an edge length of 2.5 cm. Left: Top view. From top to bottom: master oscillator, GRIN lens, power amplifier, FAC, SAC. Right: Front view including the pumping electronics on a circuit board attached to the CCP.

In a first setup, the micro-optical bench acts as a common ground contact for both active elements. In this case, the top of the AlN submount is connected to the micro-optical bench with bond wires (Fig. 3.11 left). In a second setup, the bench acts as the ground contact for the master oscillator, but the surface of the amplifier submount is connected to a separate bond pad as ground contact of the power amplifier (Fig. 3.11 right). In both cases, separate pump contacts are supplied for the master oscillator, the RW section of the amplifier, and the tapered section, similar to the tabletop setup. The gain switching pump driver is placed on a custom circuit board that can be attached to the top of the CCP (Fig. 3.12 right).

After the active elements are mounted, the passive elements can be assembled. For simpler monitoring of the amplifier output, an Ingenerics FAC08-600-XB-01 lens with a focus length of 0.6 mm is first assembled as the fast axis collimator (FAC). Since the vertical beam quality and divergence of the amplified signal and the amplifier ASE are equal, the FAC can be adjusted with reference to the unseeded amplifier output. All lenses are positioned using vacuum tweezers and a Physik Instrumente F-206.S hexapod and glued to the micro-optical bench using Norland NOA88 UV-curing glue. When positioning the lenses, the glue shrinkage has to be taken into account.

Then, an Ingenerics CYL-PL-CX lens is positioned as the slow axis collimator (SAC). Its focal length is 2.67 mm for the 3 mm long tapers and 3.0 mm for the 3.5 mm long tapers. However, the SAC is not yet glued on because the lateral divergence of the amplified signal will differ from that of the ASE.

CCP No.	Taper	M^2		max. P_{out}
		vert.	lat.	
428	3.5 mm, 6°	2.6	6.8	1.94 W
430	3 mm, 6°	2.0	5.5	2.25 W
436	3 mm, 4°	2.3	7.2	2.45 W

Table 3.2: Maximum CW output powers and beam qualities of the hybrid integrated MOPAs at 295 K.

The coupling of seed laser and amplifier is accomplished with a Grintech GT-LFRL-100-cus-50 lens with custom anti-reflection coatings for 1064 nm. It has a length of 4.417 mm and a diameter of 1 mm. The optimum working distance is 160 μm from the facets. In order to optimize the coupling, the GRIN lens has to be adjusted while both the master oscillator and the power amplifier are running. This is done in CW operation since our gain switching circuit board prevents access to the micro-optical bench. The lens position is optimized for maximum output power at narrow spectral linewidth. The required accuracy perpendicular to the optical axis is ±1 μm [169], but higher deviations are tolerable along the optical axis. This can be achieved using the hexapod mounting system. Finally, the position of the SAC is re-adjusted and it is glued to the micro-optical bench. See Fig. 3.12 for photographs of the finished modules.

During the experiments, the temperature of the CCP is kept constant. This means that the seed laser and the amplifier have the same temperature, in contrast to the table-top setup. In preparation, the performance of the table-top MOPA was evaluated with both elements at a temperature of 300 K. This yielded very similar results to those described in Sec. 3.2.2.2. The measurement setups are described in Sec. 2.4.2.

3.3.1.2 Results

Hybrid integrated MOPAs have been assembled using amplifiers with three different taper geometries (Tab. 3.2). In CW operation, all of them reach an output power of more than 1.9 W on the Bragg line. However, the beam quality is lower than that of the tabletop system, indicating non-optimum coupling.

Since the pulse intervals of our desired megahertz seed signal are much longer than the time constant of the spontaneous emission, parasitic lasing can be studied in CW operation. Therefore, the amplifier output power is measured as a function of taper current for different pump currents through
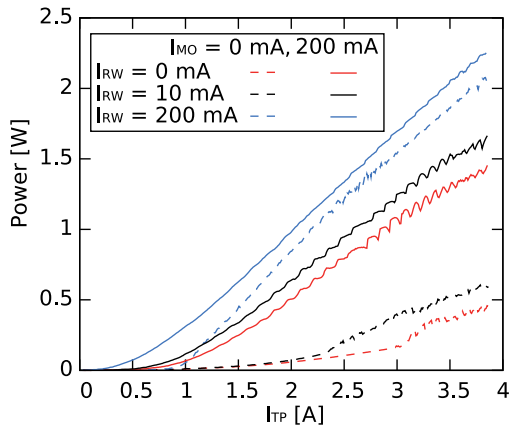
Figure 3.13: CW output power of amplifier 430 at 295 K for different RW and seed currents. The amplifier shows parasitic lasing even at $I_{MO} = I_{RW} = 0$ mA.
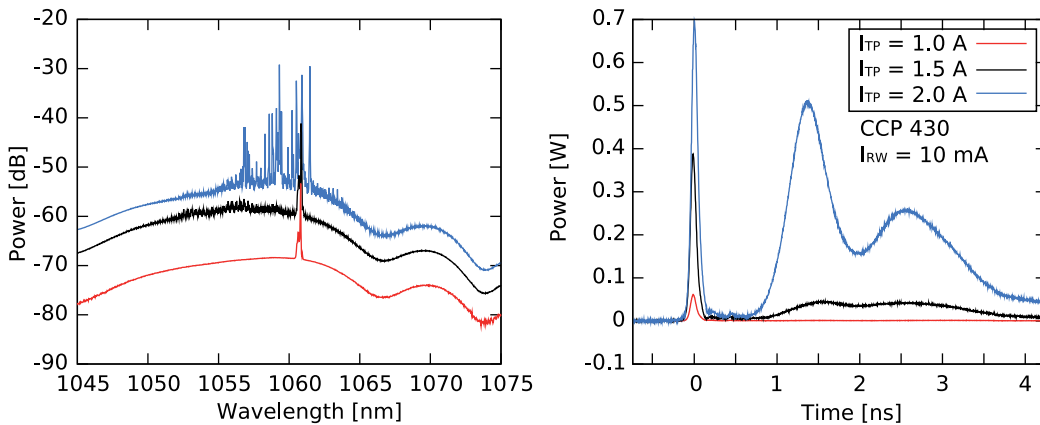
Figure 3.14: Gain switching of a hybrid integrated MOPA. Left: average output spectra. Right: pulse shape. Around the self-lasing threshold, broad afterpulses appear 1.5 ns after the signal pulse.

the seed laser and the amplifier RW section (Fig. 3.13). Unfortunately, all amplifiers show self-lasing even at $I_{MO} = I_{RW} = 0$ mA, where the RW section acts as an absorber. This means that the ASE from the tapered section is able to pump the amplifier RW section transparent and precludes the possibility to prevent self-lasing by pulsing the amplifier RW section. Even a reverse bias current applied to the RW section can not prevent self-lasing. The self-lasing threshold is not influenced by the beam shaping lenses.

The reflection from the facet of the GRIN lens can not be substantially reduced by placing the lens at an angle. An ABCD-matrix calculation [172] shows that a tilt angle of 5° still allows good coupling. At a beam divergence of 33° (half angle, $1/e^2$) in lateral direction, this reduces feedback only by 8%.

Figure 3.15: Gain-switched pulses from a hybrid integrated MOPA with two different electrical contact schemes (Fig. 3.11). A separation of the ground contacts for seed laser and amplifier suppresses the broad afterpulse observed for a shared ground contact.
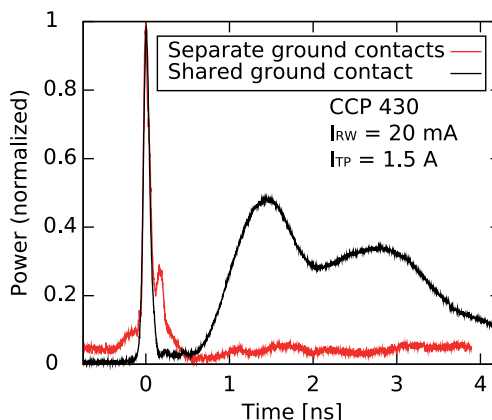
In the time-averaged amplifier output spectrum under pulsed operation, many spectral modes are visible even for moderate taper currents. For example, for amplifier 430 in configuration 1 with shared ground contacts, the output is spectrally broad for $I_{RW} = 10\,\text{mA}$ and $I_{TP} = 2\,\text{A}$ (Fig. 3.14 left). As soon as multiple modes appear in the output spectrum, the pulse shape consists of the signal pulse followed after approximately 1.5 ns by another intense pulse that is much broader (Fig. 3.14 right). If the amplitude of the gain switching pump pulse is decreased, the signal pulse disappears first, while the broad afterpulse remains. A measurement of the spectrum in this situation shows that the signal pulse is spectrally narrow while the second pulse is spectrally broad.

The broad afterpulse can be explained by electrical cross-talk from the DFB seed laser onto the amplifier RW section. If the amplifier is close to the self-lasing threshold, even a small crosstalk can trigger a gain switching pulse in the amplifier. Its broad spectrum is typical for gain switched Fabry-Pérot resonators [67, 76, 99, 121], formed here probably by the front facet of the amplifier and the front facet of the DFB laser.

The electrical crosstalk can be suppressed by separating the ground contacts for seed laser and amplifier (Fig. 3.11.2 and 3.15). However, the self-lasing threshold does not change. For separate ground contacts, the gradual switch-on of the ASE can be observed after the signal pulse (Fig. 3.15). Below the self-lasing threshold the average output spectrum is confined to the Bragg line and a maximum amplified pulse energy of only $(0.33 \pm 0.01)\,\text{nJ}$ is reached at $I_{RW} = 10\,\text{mA}$ and $I_{TP} = 1.5\,\text{A}$.

In conclusion, the hybrid integrated MOPAs coupled with a single GRIN lens have a poor performance compared to the tabletop system containing the same active elements. This is due to the lack of an optical isolator in the miniaturized setup. The resulting feedback suffices to enable parasitic lasing of the amplifier at pump currents as low as $I_{RW} = 10\,\text{mA}$ and $I_{TP} = 2\,\text{A}$.
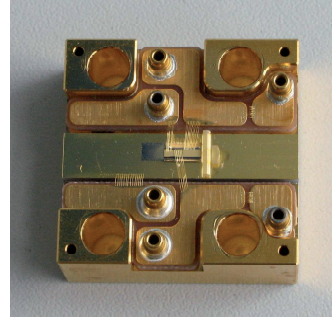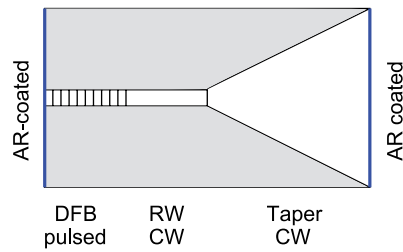
Figure 3.16: Layout of the monolithic master oscillator power amplifiers. The devices consist of three sections: DFB master oscillator (1 mm), RW pre-amplifier (1 mm) and tapered amplifier (2 mm, 6°). Both facets are anti-reflection coated. The MOPA is mounted together with the beam shaping lenses on a micro-optical bench on CCP (edge length 25 mm)

Below the self-lasing threshold, only moderate pulse energies up to 0.33 nJ can be achieved.

Since the poor performance of the hybrid integrated MOPAs is mainly due to parasitic lasing, it can probably be improved substantially by using a coupling lens system that includes a miniature optical isolator. However, good amplification performance can also be achieved with monolithically integrated master-oscillator power-amplifiers, which are additionally more robust. This is described in the following section.

3.3.2 Monolithic Semiconductor Master Oscillator Power Amplifiers

In contrast to a hybrid integrated master oscillator power amplifier, a monolithic MOPA consists only of a single semiconductor device with three sections (Fig. 3.16). The first DFB section acts as the gain switched master oscillator. The second ridge-waveguide section contains no grating and functions as a pre-amplifier and mode-filter for spurious backward-propagating light. The third section has a taper layout and is the main power amplifier. As in the table-top (Sec. 3.2.2) and hybrid integrated MOPAs (Sec. 3.3.1), the DFB section is gain switched, and the RW and tapered sections are pumped with DC current.

The devices from wafers C1737-6-3 and C1741-6-2 studied in this thesis consist of a 1 mm long DFB master oscillator section followed by a 1 mm long RW section and a 2 mm long tapered section with a taper angle of 6°. The active region consists of two compressively strained quantum wells embedded
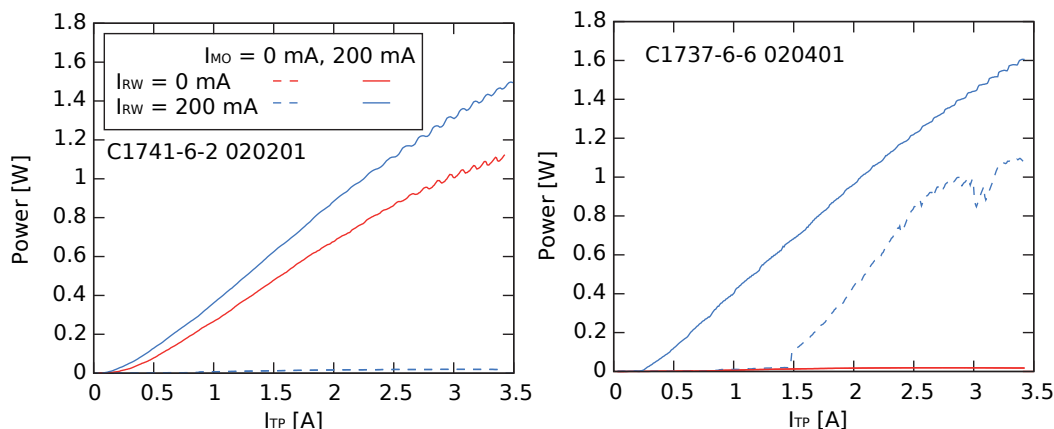
Figure 3.17: CW output power of monolithic MOPAs as a function of taper current at 295 K. Left: Wafer C1741-6-2: No parasitic lasing if $I_{\mathrm{MO}} = 0\,\mathrm{mA}$. Right: Wafer C1737-6-3: Parasitic lasing for $I_{\mathrm{MO}} = 0\,\mathrm{mA}$, $I_{\mathrm{RW}} = 200\,\mathrm{mA}$.

in a 4.8 µm thick asymmetric super-large optical cavity vertical waveguide. The ridge waveguide has a width of 4.6 µm. The wafers differ in the DFB coupling coefficient κ, which is $2.5\,\mathrm{cm}^{-1}$ for wafer C1737-6-3 and $\kappa = 10\,\mathrm{cm}^{-1}$ for wafer C1741-6-2 [173].

In contrast to a tapered laser, both facets of a monolithic MOPA are anti-reflection coated [138]. A reflectivity on the back facet would not qualitatively change the behavior of the master oscillator section, but it would provide feedback to any backward propagating light that is not confined to the ridge. Just as in the case of the hybrid integrated MOPA, the absence of any spurious reflectivities at the section interfaces or at the facets is vital for the suppression of self-lasing. This depends on details of laser layout, such as the grating phase at the facets and the quality of the anti-reflection coating.

All monolithic MOPAs are mounted on micro-optical benches on a CCP. Beam shaping optics consisting of a fast-axis collimator and a slow-axis collimator are glued in front of the amplifier output facet (Sec. 3.3.1.1). The bond scheme is analogous to that depicted in Fig. 3.11a for the hybrid integrated MOPAs, and the same driver circuit board is used (Fig. 3.12 right).

The best gain switching results have been achieved with monolithic MOPAs from wafer C1741-6-2, which have the highest self-lasing threshold. In order to determine the parameters at which self-lasing occurs, the CW output power of the monolithic MOPAs is studied(Fig. 3.17). For devices from wafer C1741-6-2, no parasitic lasing can be observed even at an RW current of 350 mA and a taper current of 4 A. If the master oscillator section is gain switched, thermal rollover occurs at lower currents than parasitic lasing. In contrast, for wafer C1737-6-3, spurious lasing occurs for an RW current as low as 50 mA.
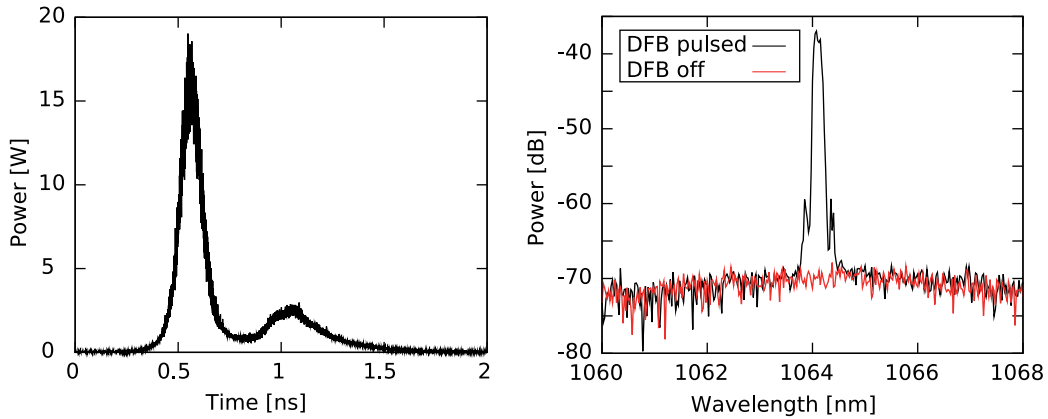
Figure 3.18: Gain-switching of monolithic MOPA C1741-6-2 020201 at 295 K. Left: Pulse shape at optimum pump settings of $I_{RW} = 350$ mA and $I_{TP} = 2.5$ A. Right: average output spectrum at $I_{RW} = 350$ mA and $I_{TP} = 4.0$ A. No self-lasing is visible if the DFB section is unpumped.

As the CW characteristics suggest, MOPAs from wafer C1741-6-2 are indeed suitable for the generation of high-power picosecond pulses with narrow spectral width (Fig. 3.18). At $I_{RW} = 350$ mA and $I_{TP} = 2.5$ A pulses with a peak power of (19 ± 1) W have been achieved. They have a pulse energy of (3.2 ± 0.1) nJ and a duration of (110 ± 5) ps, slightly longer than those generated by the table-top MOPA (Sec. 3.2.2.2). However, the lateral beam quality of the monolithic devices is significantly better, at $M^2 = 2.6$. The average side-mode suppression ratio is more than 30 dB. This makes the pulses generated by the monolithic MOPAs of wafer C1741-6-2 excellently suited for second harmonic generation (Sec. 4.3).

The monolithic MOPAs from wafer C1737-6-3, on the other hand, show qualitatively similar behavior to the hybrid integrated MOPAs (Sec. 3.3.1.2). Close to the self-lasing threshold, extra after-pulses appear, which have the typical gain switching shape. Streak-camera measurements (Sec. 2.4.2) show that the after-pulses are spectrally narrow and centered at a slightly longer wavelength than the signal pulses (Fig. 3.19). This is in contrast to the behavior of the hybrid integrated MOPAs, whose after-pulses have a broad, Fabry-Pérot-like spectrum (Sec. 3.3.1).

Still, the afterpulses of the monolithic MOPAs are most probably also caused by electrical crosstalk to the RW section. In contrast to the hybrid integrated devices, coupling from the RW pre-amplifier into the DFB laser is nearly perfect for the monolithic MOPAs. When the crosstalk pulse is gen-

Figure 3.19: Streak camera image of the gain switching pulse generated by device C1737-6-3 020402 at $I_{RW} = 100\,mA$, $I_{TP} = 3\,A$ and $300\,K$. A spurious afterpulse is generated $2\,ns$ after the signal pulse at a slightly longer wavelength.
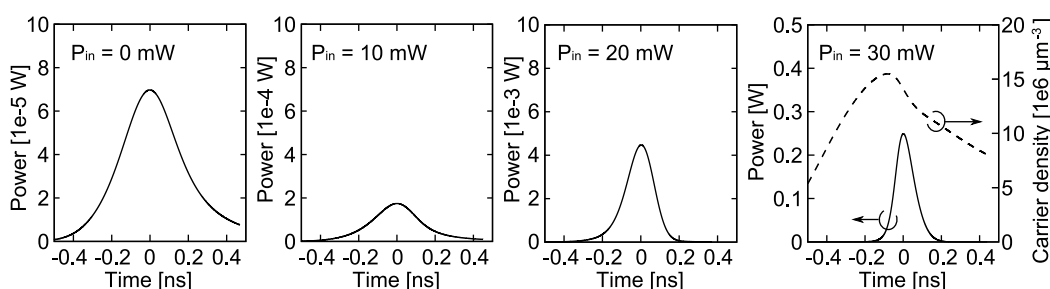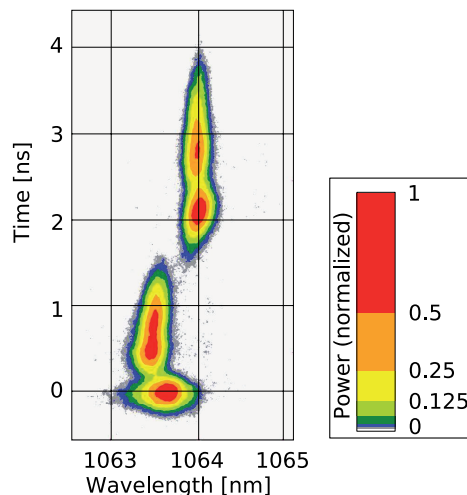

Figure 3.20: Gain-switching simulation of the DFB section of the monolithic MOPAs of wafer C1737-6-2. Due to the low reflectivity, the CW injection P_{in} from the RW section has to be taken into account and enables the generation of powerful optical pulses. Note the different power scales in the panels.

erated $2\,ns$ after the signal pulse, the DFB section is unpumped. Its grating then acts as a passive distributed Bragg reflector for the pulse generated in the RW section. Due to the low carrier density in the unpumped grating section, the refractive index now is slightly larger (Sec. 2.1.1.2) than when the signal pulse is generated. Therefore, the afterpulse has a longer wavelength than the signal pulse.

This is quantitatively confirmed by a rate-equation simulation of the gain switched DFB section (Fig. 3.20). Since both ends of the DFB section are anti-reflecting ($R_L = R_R = 10^{-3}$) and the coupling coefficient $\kappa = 2.5\,cm^{-1}$ is fairly low for wafer C1737-6-2, the lasing threshold of the DFB section is very high at approximately $500\,mW$. The available pump current pulses with an amplitude of below $1\,W$ only achieve gain switching due to the CW light injection P_{in} from the RW section, which has been included in the simulation.

At $P_{in} = 30\,mW$ and $I_{max} = 600\,mA$, the simulation yields optical pulses with a peak power of $0.25\,W$ and a duration of $112\,ps$, in good agreement with the experimental observations. The simulated peak carrier density is $1.6 \cdot 10^{19}\,cm^{-3}$. This corresponds to a change of the refractive index in the active zone of approximately 0.16 [174]. Multiplication with the confinement factor $\Gamma = 0.013$ gives the change in the effective refractive index, $\Delta n = 2.1 \cdot 10^{-3}$. At a total refractive index of 3.29, this yields a wavelength shift of $0.68\,nm$. This is in excellent agreement with the measured wavelength difference of $0.6\,nm$ between the signal pulse and the after pulse.

In contrast to the hybrid integrated MOPAs, a separation of the ground contacts of master oscillator and power amplifier is not possible in the monolithic setup. The use of capacitors in parallel to the RW section has been evaluated in order to shunt the crosstalk. However, this did not improve the device performance, which may be due to excessive parasitic inductances in the shunt.

At higher device temperatures, the self-lasing threshold is increased and higher pump currents can be used for amplification. However, simultaneously, the device efficiency decreases. Spectrally narrow picosecond pulses with a peak power close to $10\,W$ can be generated by MOPAs from wafer C1737-6-3 at $310\,K$, $I_{RW} = 100\,mA$ and $I_{TP} = 3\,A$.

In conclusion, several methods for the miniaturization of semiconductor master-oscillator power amplifiers have been investigated. None of them includes an optical isolator, so suppression of reflectivities inside the device is critical. For the hybrid integrated MOPA design, consisting of a seed laser and a tapered amplifier coupled by a GRIN rod lens, the required low level of feedback could not be achieved, and spurious lasing occurs even for $I_{RW} = 0\,mA$. However, the inclusion of a miniature isolator is possible using slightly more complex coupling optics.

Monolithic MOPAs, on the other hand, consist of a single semiconductor device only. Its first section is the gain switched master oscillator while the second and third section act as the power amplifier. The internal reflectivity here depends on details of the device layout, such as the Bragg coupling coefficient. Devices from wafer C1741-6-2 did not exhibit spurious amplifier lasing, and picosecond pulses with a peak power of $(19 \pm 1)\,W$ and narrow spectral width could be generated.

Close to the self-lasing threshold, both hybrid integrated and monolithic MOPAs become susceptible to electric crosstalk from the gain switched master oscillator to the RW pre-amplifier. This leads to the generation of spurious afterpulses 1.5–2 ns after the signal pulse. For the hybrid integrated MOPAs, the crosstalk could be suppressed by using separate ground contacts for master oscillator and power amplifier.

Chapter 4

Second Harmonic Generation of Green Picosecond Pulses

4.1 Introduction and Theoretical Background

Second harmonic generation (SHG) is a process in which an incoming (fundamental) light wave generates another wave with doubled frequency in a medium with nonlinear susceptibility. It finds widespread application in the generation of visible light, especially in the yellow-green gap [128, 129, 175–178]. For example, green laser pointers typically contain an Nd:YAG microchip laser generating 1064 nm infrared light and a nonlinear crystal for frequency doubling.

Second harmonic generation and the related nonlinear processes such as sum-frequency generation and difference-frequency generation, require *phase matching* for efficient wavelength conversion. This means that all participating waves have to retain a fixed phase relationship over the whole interaction length, in spite of chromatic dispersion.

While its foundations have been laid in the 1960s [179–184], the accurate theoretical description of nonlinear frequency conversion in the most general case of a non-Gaussian multimode fundamental beam with depletion is fairly complex and requires the full characterization of the input beam for example via the Wigner distributions [185]. In this section, the theoretical treatment is sketched for various special cases which allow important practical insights.

4.1.1 Second Harmonic Generation with Plane Waves

In crystals with non-centrosymmetric structure, the electrical susceptibility tensor χ_{ij} can depend on the electrical field strength $\vec{E}$,

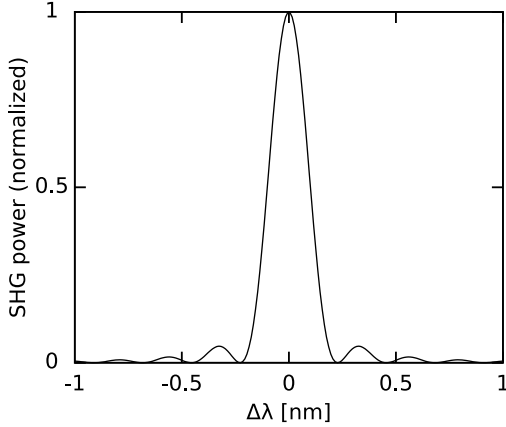$$\chi_{ij} = \chi_{ij}^{(1)} + \sum_k \chi_{ijk}^{(2)} E_k + \cdots .$$

Figure 4.1: Theoretical phase matching curve for plane waves in $1\,\mathrm{cm}$ of LiNbO$_3$. The normalized acceptance bandwidth is $340\,\mathrm{GHz\,cm} = 200\,\mathrm{pm\,cm}$ at $1060\,\mathrm{nm}$.

This produces a quadratic term in the electric polarization,

$$P_i = \varepsilon_0 \left(\sum_j \chi^{(1)}_{ij} E_j + \sum_{j,k} \chi^{(2)}_{ijk} E_k E_j \right) =: P_i^{\mathrm{L}} + P_i^{\mathrm{NL}},$$

where $d_{ijk} := \frac{1}{2}\varepsilon_0 \chi^{(2)}_{ijk}$ is defined as the nonlinear tensor. Due to crystal symmetries, this tensor usually has only a few independent elements and many elements vanish for a given crystal structure [179]

The nonlinear polarization P^{NL} contains frequency components that are not present in the incoming electrical field. In particular, if the input (fundamental) field is a monochromatic wave with frequency ω_{fun}, the polarization includes a component with twice the input frequency. According to Maxwell's equations, this nonlinear polarization wave is the source of an electromagnetic wave with frequency $2\omega_{\mathrm{fun}}$.

The calculation of the properties and intensity of this second harmonic wave typically starts from the inhomogeneous wave equation [181]

$$\vec{\nabla} \times \vec{\nabla} \times \vec{E} + \frac{1}{c_0^2} \frac{\mathrm{d}\partial^2(\varepsilon\vec{E})}{\mathrm{d}\partial t^2} = -\frac{4\pi}{c_0^2} \frac{\partial^2 \vec{P}^{\mathrm{NL}}}{\partial t^2}, \tag{4.1}$$

where the linear polarization is included in the $\varepsilon\vec{E}$ term on the left-hand side.

For plane waves, one now makes an ansatz for the electrical field as a superposition of the fundamental wave and the second harmonic wave:

$$\vec{E} = \vec{e_x} \Re \left\{ E_{\mathrm{fun}}(z) \exp\left(i(\omega_{\mathrm{fun}}t + k_{\mathrm{fun}}z)\right) + E_{\mathrm{SHG}}(z) \exp\left(i(2\omega_{\mathrm{fun}}t + k_{\mathrm{SHG}}z)\right) \right\}.$$

Generally, $k_{\mathrm{SHG}} \neq 2k_{\mathrm{fun}}$, due to dispersion. Plugging this ansatz into the wave equation 4.1 and collecting terms with equal frequency yields equations
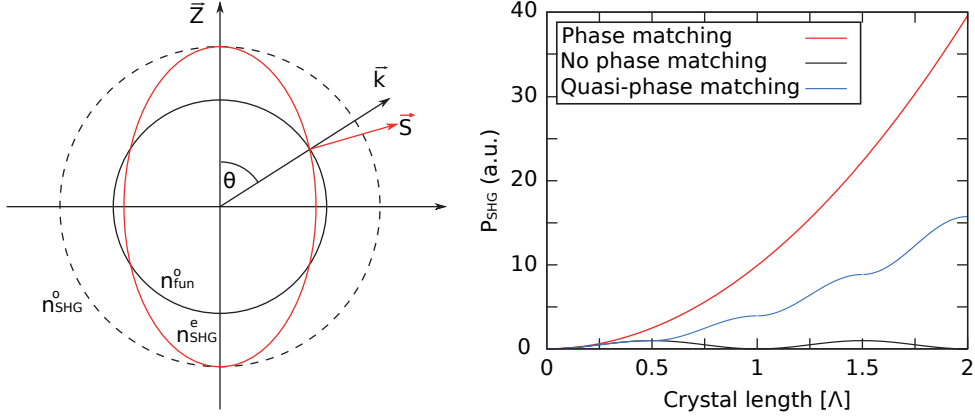
Figure 4.2: Left: Ordinary and extraordinary index of refraction in a negative uniaxial crystal as a function of propagation angle θ. Phase matching can be achieved if $n_{\text{fun}}^{\text{o}} = n_{\text{SHG}}^{\text{e}}(\theta)$. Right: Second-harmonic power as a function of crystal length for plane waves and various phase matching conditions.

of motion for the complex amplitudes [181]:

$$\frac{\text{d}E_{\text{fun}}}{\text{d}z} = i\chi^{(2)}\frac{\omega_{\text{fun}}}{c_0}2E_{\text{fun}}^{*}E_{\text{SHG}}\exp(i\Delta kz),$$
$$\frac{\text{d}E_{\text{SHG}}}{\text{d}z} = i\chi^{(2)}\frac{2\omega_{\text{fun}}}{c_0}|E_{\text{fun}}|^2\exp(-i\Delta kz), \tag{4.2}$$

where $\Delta k = k_{\text{SHG}} - 2k_{\text{fun}} = \frac{2\omega_{\text{fun}}}{c_0}(n_{\text{SHG}} - n_{\text{fun}})$ is the *phase matching factor*. If $\Delta k \neq 0$, the amplitude of the second harmonic wave oscillates periodically as energy is transferred back and forth between it and the fundamental (Fig. 4.2 right). In order to efficiently convert the fundamental into the second harmonic, *phase matching* has to be achieved ($\Delta k = 0$). This corresponds to momentum and energy conservation.

If perfect phase matching is present for a wavelength ω_0, second harmonic intensity decreases for neighboring wavelengths $\omega_0 \pm \Delta\omega$. Integration of Eq. 4.2 shows that the second harmonic power P_{SHG} follows [179, 186]

$$P_{\text{SHG}} \sim \text{sinc}^2\left(\frac{\Delta kL}{2}\right)L^2P_{\text{fun}}^2. \tag{4.3}$$

The full width at half maximum of the wavelength tuning curve (Fig. 4.1), the *acceptance bandwidth*, is inversely proportional to the crystal length and is an important material parameter of the nonlinear crystal (Sec. 4.1.2).

4.1.2 Nonlinear Optical Crystals and Phase Matching

In optically isotropic materials, phase matching is prevented by dispersion. However, $n_{\text{fun}} = n_{\text{SHG}}$ can be achieved in anisotropic crystals by taking advantage of birefringence. This is most easily understood for the case of uniaxial crystals, which have one distinguished crystallographic axis $\vec{Z}$, the *optical axis*. Any light wave whose polarization is perpendicular to the principal plane spanned by $\vec{Z}$ and its propagation vector $\vec{k}$ is called *ordinary*, while in-plane polarization is called *extraordinary*. These two wave types generally experience different indexes of refraction n^{o} and n^{e}. The extraordinary index additionally depends on the angle θ between $\vec{k}$ and $\vec{Z}$ (Fig. 4.2 left). For phase matching, the ordinary index of refraction at the fundamental wavelength has to coincide with the extraordinary index of refraction at the second harmonic wavelength, $n^{\text{o}}_{\text{fun}} = n^{\text{e}}_{\text{SHG}}(\theta)$, or vice versa.

In practice, there are two ways to achieve phase matching between an ordinary and an extraordinary beam. In the first, called *critical phase matching*, the propagation angle θ of the fundamental beam through the crystal is adjusted. This changes the index of refraction for the extraordinary beam, but not for the ordinary one. At a certain angle, phase matching may be achieved [179] (Fig. 4.2 left).

However, in general, the Poynting vector $\vec{S}_{\text{SHG}}$ of the extraordinary second harmonic beam is not parallel to its wave vector $\vec{k}_{\text{SHG}}$ but perpendicular to the index surface at the intersection of index surface and $\vec{k}$ [187]. As $\vec{k}_{\text{fun}}$ and $\vec{k}_{\text{SHG}}$ are parallel, this *spatial walk-off* reduces the spatial overlap between the fundamental and the second harmonic beam, particularly at oblique propagation angles θ. The angle between $\vec{k}_{\text{fun}}$ and $\vec{S}_{\text{SHG}}$ is referred to as the *walk-off angle ϱ*.

In *noncritical phase matching*, on the other hand, all beams propagate along the optical axis of the crystal, which means that spatial walk-off is absent. Phase matching between ordinary and extraordinary waves may then be achieved by changing the device temperature.

Since phase matching can only be achieved with specific propagation directions and polarizations of both the fundamental and the second harmonic beam, the choice of a phase matching scheme influences the effective nonlinear coefficient, since only a certain element of the nonlinear tensor can produce a phase-matched transition.

In the non-phase-matched case, the SHG output power as a function of the crystal length oscillates with a period of $2\pi/\Delta k$ (Eq. 4.3) and does not grow to macroscopic values. However, if the sign of the nonlinear susceptibility switches with the period $\Lambda = \pi/\Delta k$, the energy transfer back to the fundamental wave can be prevented and the SHG power can grow as L^2 with

material	MgO:PPLN	PPLT	PPKTP
$d_{\text{eff}}[pm/V]$	16.0 [191]	8.8 [191]	9.3 [191]
$\Delta\lambda$ [nm cm]	0.2 [192]	0.15 [193]	0.25 [194]
damage threshold [MW cm^{-2}]	120 [195]	240 [195]	9000 [196]

Table 4.1: Parameters of periodically poled crystals for SHG 1060 nm $\rightarrow$ 530 nm

a reduced effective nonlinearity of $d_{\text{eff}} = \frac{\pi}{2}d$ (Fig. 4.2 right). This method is called *quasi phase matching* [181, 186]. The required *periodic poling* of the crystal susceptibility can be achieved technologically by a variety of methods [188]. It is most popular for ferro-electric crystals, in which periodic poling can be initiated by the application of a strong electric field via narrow metal stripe electrodes [189, 190]. This is possible for example in lithium niobate (LiNbO_3) and potassium titanyl phosphate (KTiOPO_4, KTP).

Quasi-phase matching offers several advantages: Often, it is possible to achieve quasi-phase matching for wavelength combinations at which regular phase matching is not possible for a given crystal material. Furthermore, quasi-phase matching frequently allows to use the same polarization direction for all interacting waves, which often corresponds to using a larger element of the nonlinear tensor. Therefore, the effective nonlinearity for a phase-matched crystal can in fact be higher than for true phase matching at the same wavelengths. Also, quasi-phase matching offers free choice of the propagation angle, so that spatial walk-off is usually absent for quasi-phase matched crystals.

Crystal materials differ in many parameters, most importantly the effective nonlinearity d_{eff} and the normalized acceptance bandwidth $\Delta\lambda$. Another technologically relevant parameter is the damage threshold. Lithium triborate (LiB_3O_5, LBO), for example, is not suitable for periodic poling and has a moderate nonlinearity of 1 pm/V, but a very high damage threshold of $45\,\text{GW cm}^{-2}$ [197]. Therefore, it is widely used for high-power applications. For moderate peak powers as discussed in this thesis, periodically poled materials are advantageous. Popular choices with good availability for the second harmonic generation 1060 nm $\rightarrow$ 530 nm are lithium niobate (PPLN), lithium tantalate (PPLT) and potassium titanyl phosphate (PPKTP) (Tab. 4.1). PPLN is used in this work since it has the highest nonlinear coefficient and expected peak power densities are on the order of only $1\,\text{MW cm}^{-2}$.

4.1.3 Second Harmonic Generation with Gaussian Beams

While the assumption of plane waves is valid for waveguides and very short crystals, this thesis focuses on second harmonic generation in long bulk crystals. While SHG in waveguides allows for higher total conversion efficiencies [177, 178, 189], a high alignment precision is required, and coupling losses can be quite high for fundamental beams with non-diffraction-limited beam quality. With view to integration of the SHG crystal with a monolithic MOPA (Sec. 3.3.2) on a micro-optical bench, a bulk crystal for the picosecond SHG experiments.

When performing second harmonic generation with Gaussian beams, it is important to optimize the focus position and the Rayleigh length z_R of the fundamental beam in addition to the phase matching parameter. Again, the second harmonic power can be obtained from the coupled wave equations 4.2, but for a Gaussian beam this requires the propagation and integration of the second harmonic waves radiated from each infinitesimal slab of material along the optical axis. Even without pump depletion, the theory of Gaussian SHG is significantly more complex than for a plane wave fundamental, and no closed form for the second harmonic power can be given [184]. For a description of quasi-phase matching, birefringence and spatial walk-off can be neglected. Furthermore, absorption is neglected, which is weak at 1060 nm and 530 nm in $LiNbO_3$. The result for the second harmonic power in the end can be cast into a similar form as for plane waves,

$$P_{SHG} = \frac{9 \cdot 10^9}{16\pi^2} \frac{128\pi^2 \omega_{fun}^2}{c_0^3 n_{fun}^2 n_{SHG}} d_{eff}^2 P_{fun}^2 L k_{fun} h(\sigma, \xi, \mu), \qquad (4.4)$$

where the dependence on all the optimizable parameters is contained in the function

$$h(\sigma, \xi, \mu) = \frac{1}{4\xi} \int_{-\xi(1-\mu)}^{\xi(1+\mu)} d\tau \int_{-\xi(1-\mu)}^{\xi(1+\mu)} d\tau' \frac{\exp\left(i\sigma(\tau' - \tau)\right)}{(1 + i\tau')(1 - i\tau)}.$$

Here, $\sigma = z_R \Delta k$ describes the phase matching, $\xi = L/(2z_R)$ the Rayleigh length, and $\mu = (L - 2f)/L$ the focus position. Unsurprisingly, for perfect phase matching, the optimum focus position is in the center of the crystal [180]. The *Boyd-Kleinman-factor h* then takes a single maximum of 1.068 for a value of $\xi = 2.84$ [184]. This can be easily be set experimentally by choosing the appropriate focusing lens.

Note that in contrast to the plane-wave case, the second harmonic power for a Gaussian fundamental beam increases only linearly with the crystal length

(Eq. 4.4), even when ξ is kept at its optimum value. This is due to the fact that the Rayleigh length can only be increased by enlarging the beam waist. This in turn decreases the peak light intensity in the beam waist, lowering the SHG efficiency.

Modern experiments with a high total conversion efficiency require the inclusion of pump depletion in the theoretical treatment. This requires numerical simulation and has become feasible only since the availability of sufficient computing power. If substantial pump depletion is present, maximum conversion is achieved under substantially weaker focusing than for the no-depletion case studied by Boyd and Kleinman. Furthermore, both the fundamental and the second harmonic beam quality may be degraded by inhomogeneous conversion [187, 198].

4.1.4 Second Harmonic Generation with Non-Gaussian Beams

The use of edge-emitting semiconductor lasers or amplifiers as fundamental light sources for second harmonic generation is attractive due to their compactness, high efficiency, high reliability, and low cost. However, high-power edge emitters, especially of the broad area and tapered geometry, typically do not generate diffraction-limited beams (Sec. 3.1.2.2 and 3.2.2). Therefore, a description of second harmonic generation for partially coherent beams with a non-diffraction-limited beam quality is required.

Experimentally, the SHG efficiency for non-diffraction-limited beams is lower than for Gaussian beams when all other parameters are optimized [57, 199, 200]. The focusing parameter $\xi = L/(2z_{\mathrm{R}})$ for maximum output power is reduced for a partially coherent beam. For a tapered laser with a vertical beam quality of $M^2 = 1.9$ and a lateral beam quality of $M^2 = 2.4$, the optimum focusing parameter is $\xi = 1.4$ [57], only half of the value $\xi = 2.8$ for Gaussian beams (Sec. 4.1.3).

The theoretical description has so far focused on the Gauss-Schell model [57, 201, 202], which assumes a Gaussian transverse envelope consisting of a superposition of Gaussian coherence regions whose width is smaller than the beam diameter. This leads to a non-diffraction-limited beam quality. Furthermore, the beams can be astigmatic and elliptic. With this model, the optimum focusing parameter ξ can be successfully predicted as a function of beam quality [57], while the agreement of the maximum efficiency is moderate.

By using a Gauss-Schell model, one neglects the complex lateral beam profiles typical for edge-emitting diode lasers. Broad-area devices, for example, generate beams with nearly top-hat profile, while tapered lasers typically show

a beam waist with an intense central lobe and weak satellites. Both beams can have the same second-moment M^2, but the latter will achieve much higher SHG efficiencies. Generally, a high SHG efficiency is achieved for a good beam quality or at least a pronounced central beam lobe.

4.1.5 Second Harmonic Generation with Multi-Mode Beams

The gain switched picosecond pulses studied in this thesis have time-averaged spectral envelopes with a width of 0.1–0.3 nm (Sec. 3.2.2). This is similar to the normalized acceptance bandwidth of $LiNbO_3$ (Tab. 4.1). Therefore, a description of second harmonic generation for a fundamental with an arbitrary spectral envelope $P_{fun}(\omega)$ is needed.

Key insights about this situation can be gained from the plane wave case without pump depletion [186]. Starting from the coupled wave equations 4.2, one now makes a discrete multi-mode ansatz for the fundamental electrical field

$$E(z,t) = \sum_{q=-Q}^{Q} E_{fun}^q \exp(i\omega_{fun}^q t - k_{fun}^q z + \varphi^q),$$

where $\omega_{fun}^q = \omega_{fun}^0 + q\Delta\omega$ is the frequency for mode number q, k_{fun}^q is the corresponding propagation constant and E_{fun}^q the electrical field amplitude.

This immediately gives differential equations for the second harmonic modes, which also include mixed terms describing sum-frequency generation:

$$\frac{dE_{SHG}^{2r}}{dz} = \frac{i\omega_{fun}^0 d}{n_{SHG}c_0} \Bigg\{ (E_{fun}^r)^2 \exp\left(i(k_{SHG}^{2r} - 2k_{fun}^r)z + 2i\varphi^r\right)$$

$$+ 2\sum_{q=1}^{Q-|r|} E_{fun}^{r+q} E_{fun}^{r-q} \exp\left(i(k_{SHG}^{2r} - k_{fun}^{r+q} - k_{fun}^{r-q}z + i(\varphi^{r+q} + \varphi^{r-q}))\right) \Bigg\},$$

$$\frac{dE_{SHG}^{2r+1}}{dz} = \frac{i\omega_{fun}^0 d}{n_{SHG}c_0} \Bigg\{ 2\sum_{q=0}^{Q-|r|-1} E_{fun}^{r+q+1} E_{fun}^{r-q} \exp\left(i(k_{SHG}^{2r+1} - k_{fun}^{r+q+1} - k_{fun}^{r-q})z\right)$$

$$\times \exp\left(i(\varphi^{r+q+1} + \varphi^{r-q})\right) \Bigg\}.$$

This causes the SHG spectrum to have twice as many modes as the fundamental spectrum. The phase mismatch is approximately equal for the terms in each sum, and the phase matching parameter $\Delta k^m = k_{SHG}^m - k_{fun}^{m-n} - k_{fun}^n$ can be defined independently of n.

After normalization of fundamental and second harmonic fields, the differential equations can be integrated and the second harmonic power in each mode can be estimated by taking the square of the absolute value.

For the treatment of a nearly continuous spectrum, the odd and even second harmonic modes can then be approximated by one expression. Replacing the discrete spectrum by a continuous one and the sums by frequency integrals, one finds that the second harmonic spectral power density is given by a convolution of the input spectrum [186],

$$P_{\text{SHG}}(\omega) = 2F\big(\Delta k(\omega)\big) \int_{-\infty}^{\infty} P_{\text{fun}}(\omega - \omega') P_{\text{fun}}(\omega') d\omega', \qquad (4.5)$$

where $F(\Delta k(2\omega))$ is the sinc^2 factor from Eq. 4.3 and ω is measured relative to the fundamental central frequency ω_{fun}^0.

Interestingly, a calculation for an infinite number of modes that all fit inside the crystal acceptance bandwidth shows a twofold increase in conversion efficiency compared to the single-mode case [186]. This has in fact been verified experimentally in an elegant experiment with a HeNe laser whose number of longitudinal modes could be manually tuned [203].

However, if the fundamental spectrum exceeds the crystal acceptance bandwidth, SHG efficiency decreases. Therefore, a narrow fundamental spectrum is essential for high SHG efficiency.

This section has given an introduction to the theoretical description of second harmonic generation. Starting from the single-frequency plane-wave case, phase matching and quasi-phase matching have been discussed, and it has been shown that the second harmonic power increases with the square of the fundamental power if depletion is neglected.

In the case of a focused fundamental beam, the optimization of the focus position and Rayleigh length in the SHG crystal is important. For the case of a Gaussian beam, the optimum Rayleigh length has been calculated by Boyd and Kleinman to $z_R = 0.175L$, where L is the crystal length. For non-diffraction-limited beams from edge-emitting diode lasers, the optimum focusing can be adequately predicted using a Gauss-Schell model. For higher M^2 values, the optimum Rayleigh length is increased by up to a factor of two while the SHG efficiency is decreased.

In the case of a multi-longitudinal-mode beam, the efficiency can either increase if the fundamental laser has many modes well inside the crystal acceptance bandwidth, or decrease if the fundamental spectral width exceeds the acceptance bandwidth.

4.2 Second Harmonic Generation using Picosecond Pulses

Picosecond pulses in the green spectral range have important applications in time-resolved fluorescence spectroscopy and related methods [126]. They enable tracking of single molecules in living cells [61] and microscopy with sub-wavelength resolution. Scanning imaging methods typically require pulse energies on the order of 100 pJ at variable repetition rates in the MHz range in order to avoid fluorophore bleaching. For wavelengths in the blue and red spectral range, such pulse trains can be readily provided by gain switched laser diodes in very compact and robust setups [12]. There is great interest in green picosecond sources, as well, but there are no laser diodes commercially available near 530 nm. Therefore, second harmonic generation (SHG) is the method of choice to realize a green picosecond source [127, 129, 175]. Using multi-stage solid-state setups as the fundamental, green picosecond pulses with energies of several 100 nJ have been obtained at fixed repetition rates [175]. At variable repetition rates, pulse energies of 80 pJ with a peak power below 0.5 W have been demonstrated at 530 nm [127]. Higher peak powers would make existing imaging methods more versatile and enable new applications, e.g. wide-field microscopy. However, their generation at flexible repetition rates remains a challenge.

Using the bench-top semiconductor MOPA (Sec. 3.2.2) as a fundamental source, intense green picosecond pulses are generated by frequency doubling. The resulting green pulse source has a variable repetition rate and a high potential for miniaturization (Sec. 4.3). Compared to the gain switched DFB master laser, the green pulses have a significantly improved pulse shape due to the nonlinear nature of amplification (Sec. 3.2.2) and second harmonic generation.

4.2.1 Differences to Continuous-Wave Operation

In addition to applications in which green picosecond pulses are specifically required, pulsed fundamental sources are often used in second harmonic generation in order to obtain a high conversion efficiency while keeping the average fundamental power low [204].

In a pulsed fundamental signal, the instantaneous peak power exceeds the average power by far, especially if the duty cycle is low (Fig. 4.3). Since SHG is a nearly instantaneous process, the second harmonic peak power depends on the square of the fundamental peak power.
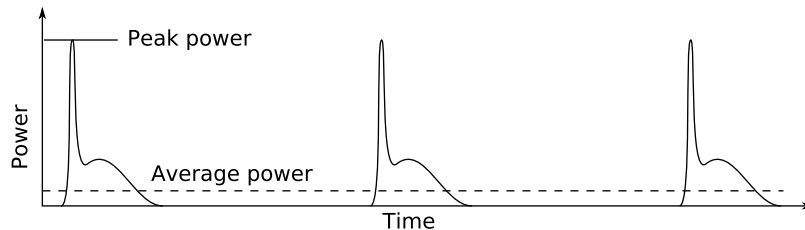
Figure 4.3: Illustration of average and peak power for a train of gain switched pulses.

When comparing the normalized conversion efficiency

$$\eta = \frac{P_{\mathrm{SHG}}}{P_{\mathrm{fun}}^2 L} \tag{4.6}$$

of SHG in pulsed and cw mode, it is important to distinguish between time-averaged and instantaneous conversion efficiency. The instantaneous normalized conversion efficiency

$$\eta(t) = P_{\mathrm{SHG}}(t) / \left(P_{\mathrm{fun}}^2(t) L \right)$$

is independent of the fundamental signal shape if spectrum and beam quality are equal. The normalized conversion efficiency of the average power

$$\bar{\eta} = \frac{\frac{1}{T} \int_0^T P_{\mathrm{SHG}}(t) dt}{\left(\frac{1}{T} \int_0^T P_{\mathrm{fun}}(t) dt \right)^2 L},$$

on the other hand, can be much higher in pulsed operation. This allows the efficient generation of high green average powers without high thermal load to the crystal. However, the conversion efficiency of the average power cannot be directly compared to other SHG results if the signal shape is not known.

4.2.2 Experimental Setup

In this work, picosecond pulses at 531 nm are generated using a bench-top all-semiconductor master oscillator-power-amplifier (MOPA) as the fundamental source. This design enables miniaturization [169] and allows the green laser to share the advantages of the gain switched master oscillator (MO), particularly the possibility to generate arbitrary pulse sequences by electrical triggering. The setup of the light source is described in detail in Sec. 3.2.2.

As the master oscillator, a 1.5 mm long triple quantum well RW DFB laser diode is used. It is pumped with short current pulses without DC bias at
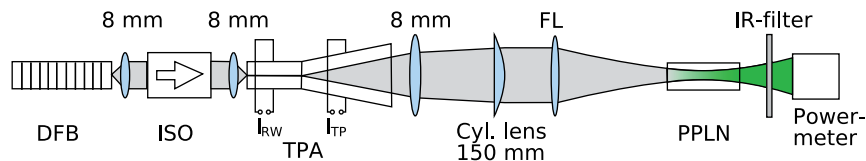
Figure 4.4: Experimental setup for the bench-top generation of green picosecond pulses. Focusing lens FL has focal length 35 mm for crystal 1 and 150 mm for crystal 2. The MOPA fundamental source is describe in detail in Sec 3.2.2.

repetition rates of up to 80 MHz. The emitted light pulses reach an energy of (385 ± 12) pJ and a peak power of (770 ± 50) mW with a significant pulse tail. The pulse duration is less than 700 ps FWHM. The average spectral width is less than 30 pm FWHM with a center wavelength of (1062.03 ± 0.1) nm. However, the spectrum changes dynamically during each pulse, as discussed below.

Measurement setups are described in Sec. 2.4.2. Unless otherwise noted, pulse lengths and peak powers stated in this paper are as measured without deconvolution with the instrument response function (IRF).

Using two aspheric lenses, the pulsed seed light is collimated and focused into the SOA. This double quantum well power amplifier consists of a 1 mm long RW section and a 3 mm long tapered (TP) section with a taper angle of $6°$. In order to prevent lasing of the power amplifier in the intervals between the seed pulses, a -30 dB optical isolator is used between the master oscillator and the amplifier (Fig. 4.4).

Pumping the amplifier RW section with a DC current of 10 mA and the tapered section with a DC current of 3.93 A, the amplified light pulses reach an energy of (3.13 ± 0.09) nJ and a peak power of (28 ± 2) W, independent of the repetition rate. In the intervals between the seed pulses, the amplifier emits (170 ± 5) mW of amplified spontaneous emission (ASE), which forms a spectrally broad continuous-wave (CW) background to the amplified pulse signal. For the measurement of the amplified pulse energy, see Sec. 3.2.2. The amplified IR signal is collimated using an aspheric lens and an additional cylindrical lens for the slow axis. This yields a nearly symmetric beam with a beam quality of $M^2 \approx 5$ (second moments) in the lateral direction [134].

For second harmonic generation, two MgO-doped bulk PPLN crystals have been available which both have a poling period of 6.92 μm and are anti-reflection coated for both 1064 nm and 532 nm. Crystal 1 has a length of 5 mm, corresponding to a spectral acceptance bandwidthof approximately

400 pm FWHM (Tab. 4.1). Due to the broad spectral acceptance, this crystal shows high normalized conversion efficiency in pulsed operation, as discussed below. Crystal 2 has a length of 25 mm, resulting in an acceptance bandwidth of 80 pm FWHM, and enables higher green output powers.

4.2.3 Green Pulse Shape and Energy

In order to determine the conversion efficiency of the crystals for the given beam quality of $M^2 \approx 5$, SHG is first performed with the MOPA in CW operation. In this operating mode, the MOPA has a clean single-mode spectrum. For both crystals, a normalized conversion efficiency of $\eta_{cw} = (0.67 \pm 0.04)\,\%/(\text{W cm})$ is obtained. Optimum focusing is achieved with a $f = 35\,\text{mm}$ lens for crystal 1 and a $f = 150\,\text{mm}$ lens for crystal 2.

To study pulsed SHG, the same setup was used. With crystal 2, a maximum pulse energy of $(250 \pm 8)\,\text{pJ}$ at 531 nm and a peak power of $(5.7 \pm 0.4)\,\text{W}$ is achieved at all repetition rates between 5 and 80 MHz. The measured pulse length is $(31 \pm 5)\,\text{ps}$, deconvolution with the IRF suggests a real pulse length of only 18 ps at a peak power of approximately 10 W. This exceeds previous green picosecond sources at variable repetition rate by more than an order of magnitude. The ASE present in the amplified IR signal is reduced to less than 0.2 mW, corresponding to an extinction ratio of at least 44 dB for the green signal. This makes our light source ideally suited for applications in fluorescence spectroscopy. Crystal 1 generates a lower peak power of $(2.0 \pm 0.1)\,\text{W}$, but a higher normalized conversion efficiency, as discussed in Sec 4.2.4.

During amplification and SHG, the signal pulse shape improves. In a typical feature of gain switching, the seed laser pulses have a significant pulse tail following the pulse peak (Fig. 4.5 left, for three different pump levels). While the optical peak power is mainly given by the laser dynamics and only weakly depends on the pump current pulse, the energy in the pulse tail strongly depends on the peak pump current [67] (Sec. 2.2).

During amplification, the pulse peak experiences strong gain and depletes the amplifier. This leaves less gain for trailing pulse regions, effectively suppressing the pulse tail (Fig. 4.5 center, Sec. 3.2.2). During SHG, the high-power peak undergoes higher absolute conversion than the less powerful after-pulse. As a result, the power level of the latter is suppressed to less than 10% of the pulse peak power, and the green pulse shape is almost independent of the pump level of the gain switched master oscillator (Fig. 4.5 right).
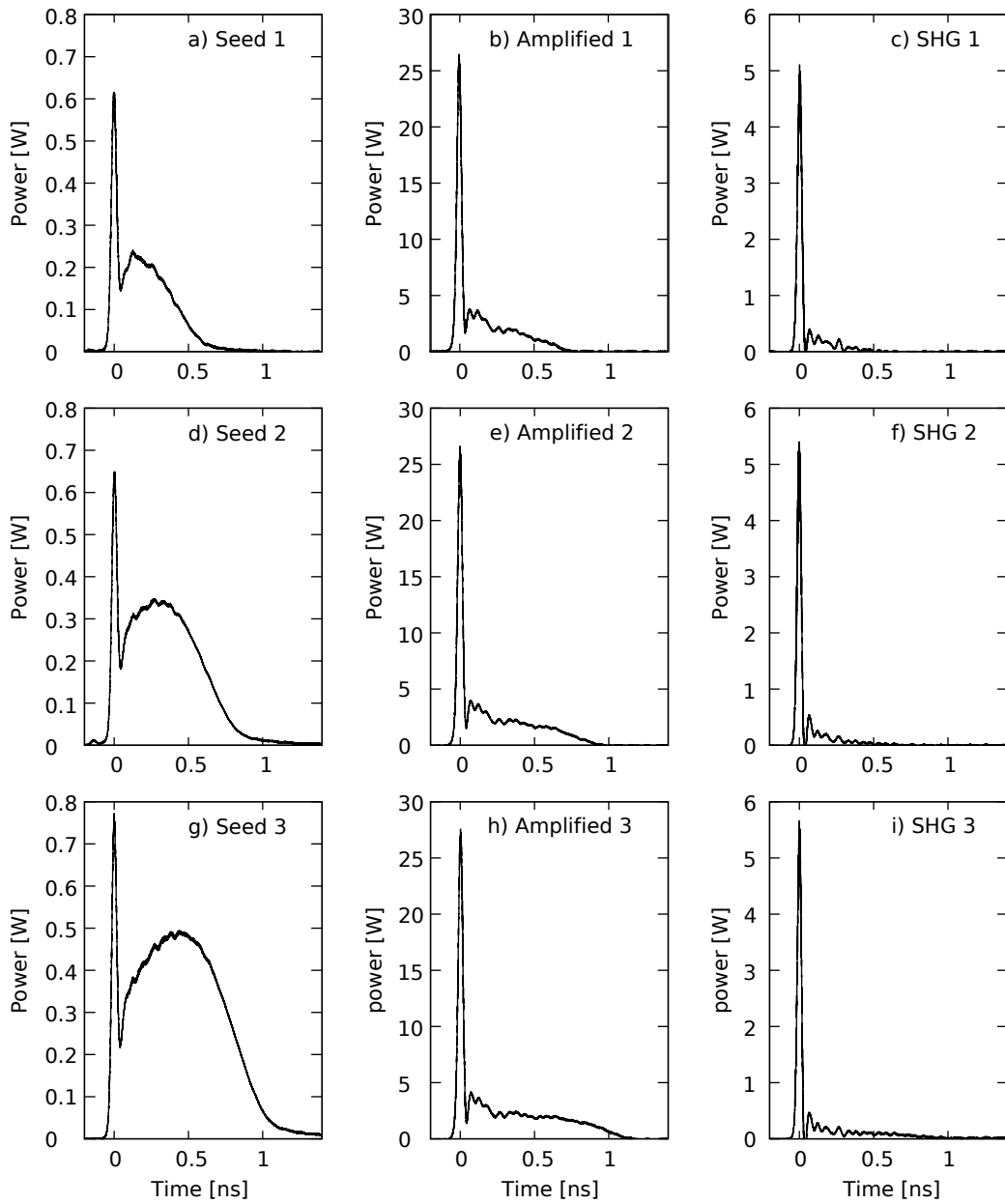
Figure 4.5: Pulse shapes of seed, amplified signal, and SHG signal using crystal 2. The peak seed pump current increases from setting "1" through "3". The resulting green pulse shapes are nearly independent of the initial seed pulse shape.
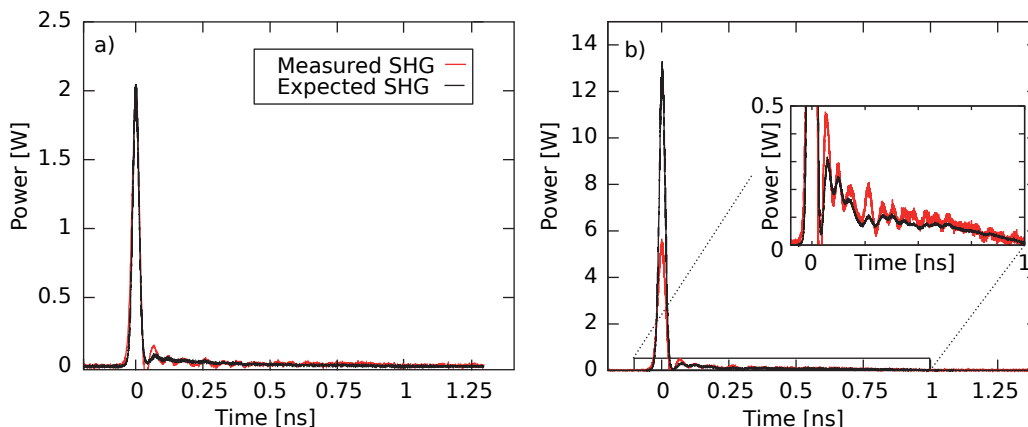
Figure 4.6: Measured SHG pulse shape and expected SHG pulse shape calculated from the measured amplified IR signal with a conversion efficiency of 0.67%/(W cm) for (a) crystal 1 and (b) crystal 2.

4.2.4 Dynamic Normalized Conversion Efficiency

As shown in Sec. 2.4.3, DFB lasers tend to have a broader spectrum during the leading relaxation peak than during the pulse tail. This is true even when the time averaged side-mode suppression ratio is above 30 dB and the residual Fabry-Pérot modes are strongly suppressed. The spectral broadening at the pulse onset is due to both mode competition between modes close to the stopband and chirp caused by the strong carrier fluctuations [205]. This broader spectrum can influence the SHG efficiency during the leading relaxation peak.

In order to compare the instantaneous normalized conversion efficiency for gain switched operation with η_{cw}, the expected SHG signal is calculated from the fundamental pulse shape as $P_{fun}^2(t)L\eta_{cw}$. For crystal 1, the expected SHG pulse shape and the measured signal are in good agreement (Fig. 4.6 a). Higher fluctuations in the measured pulse shape are due to the non-Gaussian instrument response function. On the other hand, for crystal 2, the measured SHG peak power is significantly lower than expected for conversion with η_{cw} (Fig. 4.6 b). The instantaneous normalized conversion efficiency at the pulse peak is reduced to $\eta_{peak} = (0.30 \pm 0.05)\%/(\text{W cm})$, while during the pulse tail it equals the cw conversion efficiency, $\eta(t) = \eta_{cw}$. This effect persists if the instrument response is taken into account and can be observed at all seed pump powers.

The reduced η_{peak} for crystal 2 originates from the spectral dynamics of the IR pulses. For a long crystal with narrow spectral acceptance bandwidth, the fundamental spectrum during the pulse peak is broader than the crystal
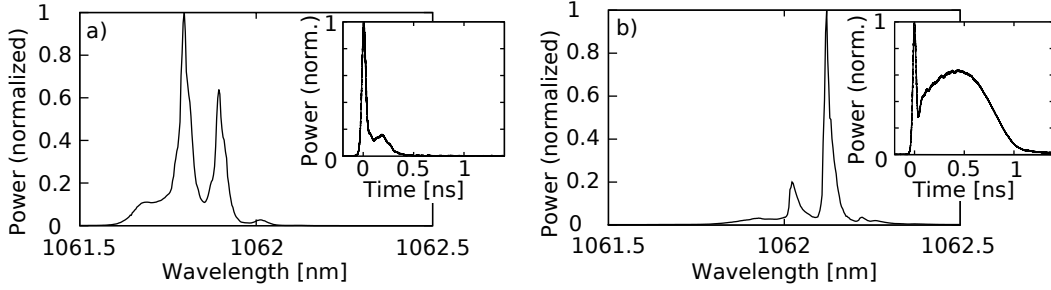
Figure 4.7: Averaged amplified pulse spectra at (a) low seed pump current and (b) high seed pump current (setting "3"). Inset: seed pulse shapes.

acceptance bandwidth, leading to a reduced η_{peak}. This effect is absent for crystal 1, which has a broader spectral acceptance. A quantitative understanding can be gained from the time-averaged spectrum of the MOPA at seed setting "3" (Fig. 4.7 b). It contains contributions of both the relaxation peak and the after-pulse. Calculating the SHG power for this fundamental spectrum (Sec. 4.1.5 and an acceptance bandwidth of 80 pm FWHM, the normalized conversion efficiency is calculated to be 0.55%/(W cm). This is in good agreement with the weighted average of the measured instantaneous conversion efficiency for crystal 2,

$$\frac{\int P(t)\eta(t)dt}{\int P(t)dt} \approx 0.56\%/(\text{W cm}).$$

At low seed pump power, the MOPA spectrum is dominated by the relaxation peak (Fig. 4.7 a) and shows a lower side mode-suppression ratio. For this fundamental spectrum, an effective normalized conversion efficiency of 0.34%/(W cm) is calculated, which agrees well with the measured peak conversion efficiency of $(0.30 \pm 0.05)\%/(\text{W cm})$ for crystal 2.

In conclusion, a detailed study of SHG using gain switched laser pulses has been performed, including for the first time the time-dependence of the conversion efficiency. Due to the spectral dynamics of the fundamental pulse, its pulse peak is converted less efficiently than the pulse tail in SHG crystals with narrow acceptance bandwidth. A picosecond laser pulse source at 531 nm with a pulse energy of (250 ± 8) pJ is demonstrated. The green laser pulses can be electrically triggered and their shape is nearly independent of repetition rate and seed pump power. Their peak power of more than 5.7 W exceeds that of previous green picosecond lasers with variable repetition rate by at least an order of magnitude. Combined with the excellent extinction ratio of more than 44 dB, the presented green picosecond laser is an ideal light source for time-resolved fluorescence spectroscopy.
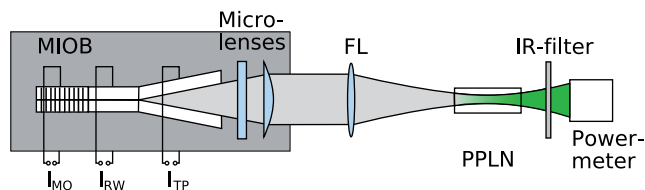
Figure 4.8: Setup for SHG using a monolithic MOPA (Sec. 3.3.2) as the fundamental source.

4.3 Miniaturization

In order to fully harness the advantages of a semiconductor-based green picosecond pulse source in biological experiments, a robust and compact package is required. On the path toward full hybrid integration of the fundamental light source and the nonlinear crystal on a micro-optical bench, picosecond SHG experiments are performed using a monolithic MOPA (Sec. 3.3.2) as the fundamental source.

The fundamental IR source is a monolithic MOPA from wafer C1741-6-2 mounted on a micro-optical bench on CCP (Sec. 3.3.2). The first 1 mm long DFB section acts as the master oscillator and is gain switched to generate picosecond pulses. The subsequent RW section of 1 mm length and the tapered section of 2 mm length are pumped with DC current. At $I_{RW} = 225$ mA and $I_{TP} = 3.25$ A, it emits laser pulses with a peak power of (16 ± 1) W, an energy of (3.01 ± 0.09) nJ at a central wavelength of 1063.86 nm. Although these pulses have a lower peak power than those emitted by the bench-top MOPA (Sec. 3.2.2), they have a better beam quality of $M^2 = 2.6$ in lateral direction. This increases the normalized SHG efficiency (Sec. 4.1.4), so that a similar second harmonic output power can be achieved in spite the lower peak power.

The infrared light emitted by the monolithic MOPA is collimated by microlenses on the micro-optical bench (Sec. 3.3.2) and focused into the 25 mm long PPLN crystal with an external focusing lens (Fig. 4.8). The optimum focus length of 100 mm was determined experimentally.

In this way, green picosecond pulses with an energy of up to (275 ± 0.8) pJ are generated at variable repetition rates (Fig 4.9). This exceeds the second harmonic pulse energy generated with the bench-top MOPA as the fundamental source (Sec.4.2.3). The pulses are, however, longer, with a duration of (112 ± 5) ps FWHM. They have a peak power of (2.3 ± 0.1) W and a CW background of less than 0.01 mW, corresponding to an extinction ratio of at least 54 dB. Although the peak power of the green pulses generated from the monolithic MOPA does not match that of the bench-top setup, the important specification for fluorescence lifetime spectroscopy is pulse energy, as long as
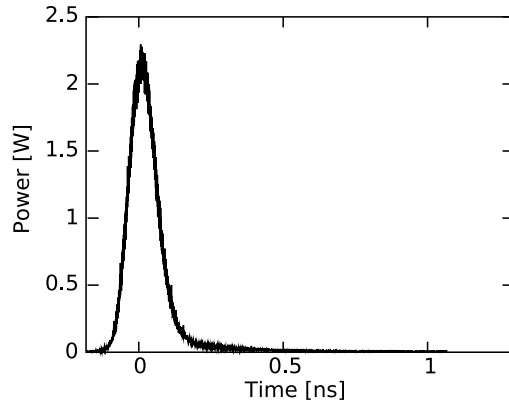
Figure 4.9: Second harmonic pulse shape generated using a monolithic MOPA as fundamental source. $I_{\mathrm{RW}} = 225\,\mathrm{mA}$, $I_{\mathrm{TP}} = 3.25\,\mathrm{A}$, $295\,\mathrm{K}$

it is delivered within less than $200\,\mathrm{ps}$ [7]. Therefore, the green pulse source based on the monolithic MOPA is excellently suited for fluorescence lifetime spectroscopy.

A peak normalized conversion efficiency of $0.36\%/(\mathrm{W\,cm})$ is reached, 20% higher than the peak conversion efficiency for the bench-top MOPA.

Chapter 5

Conclusion and Outlook

5.1 Summary and Conclusion

The objective of this thesis was the development of a reliable and intense green picosecond laser source for fluorescence lifetime spectroscopy. This application requires pulses with a duration of less than 200 ps and a pulse energy of around 100 pJ at variable repetition rates in the megahertz range [7]. In the red and blue spectral range, such pulses can be readily generated by gain switching of single ridge-waveguide laser diodes [12]. However, green emitting laser diodes so far exist only as laboratory samples with limited lifetime [206]. Therefore, second harmonic generation is the method of choice for the generation of green picosecond pulses.

In a first step toward a compact, reliable green picosecond source, gain switching of single DFB laser diodes was studied(Sec. 2.4). Detailed experimental and numerical studies showed that the grating coupling coefficient is a crucial design parameter that influences not only the spectral purity of the gain switched signal, but also the amplitude of the first relaxation oscillation. A higher coupling coefficient provides a higher net gain to the Bragg mode, but also causes less efficient out-coupling and higher radiative losses in the case of a higher-order grating. This results in a reduction of the gain switched pulse peak power.

If the coupling coefficient is too weak, on the other hand, mode competition between the Bragg mode and the residual Fabry-Pérot modes is slow and takes up to several hundred picoseconds. This leads to a multimode laser spectrum of the first high-power relaxation peak, rendering the pulses unsuitable for second harmonic generation.

In order to obtain high spectral purity and high pulse peak power, the gain of the Bragg mode has to be maximized by other means, most prominently by choosing the optimum detuning between gain maximum and Bragg wavelength. This optimization has to take into account the shape of the gain spectrum and its dependence on carrier density and device temperature.

While in CW-operation, the center wavelength of the gain is primarily determined by internal device heating, this effect is irrelevant for pulsed operation at low duty cycles. On the other hand, for gain switched operation, the carrier density during the first relaxation peak significantly exceeds the steady state value, leading to a blue-shift of the gain spectrum. Therefore, at low carrier density, the Bragg wavelength ideally is several nanometers shorter than the wavelength of the gain maximum. Under these conditions, gain switched pulses with a peak power in excess of 1 W and more than 95% of the pulse energy emitted in the Bragg mode were generated.

In a next step, the optical amplification of these pulses to peak powers above 10 W was investigated (Chap. 3). In order to study the suitability of different amplifier gain materials, a semiconductor tapered amplifier was compared with a single-stage core-pumped ytterbium-doped fiber amplifier. Both technologies allowed amplifications of above 10 dB. However, the gain materials differ greatly in their upper-state lifetime, which is approximately 1 ms for Yb:glass, but only few nanoseconds in the semiconductor amplifier. Consequently, large energies on the order of microjoule can be stored in a ytterbium-doped fiber while the saturated output energy of semiconductor amplifiers is in the lower nanojoule range.

On the other hand, the long upper-state lifetime means that the ytterbium-doped fiber amplifier does not reach equilibrium within the pulse intervals of a megahertz seed signal. Therefore, the pulse gain decreases at higher repetition rates. Furthermore, the seed pulse energy of about 100 pJ coming from the gain switched DFB laser diode does not suffice to saturate the fiber gain. This leads to a low pump efficiency, and the pulse shape remains unchanged during amplification.

The gain of the semiconductor amplifier with its short upper-state lifetime is independent of the repetition rate in the megahertz range. However, the suppression of feedback into the amplifier is critical in order to avoid parasitic lasing in the pulse intervals. Due to the low saturation energy, the signal pulse is distorted during amplification. For gain switched seed pulses, this is advantageous, since the characteristic pulse tail is effectively suppressed, leading to a cleaner and more symmetric pulse shape. With a bench-top semiconductor MOPA, picosecond pulses with a peak power of 28 W and a pulse energy of 3.1 nJ were generated. This exceeds previous realizations by more than a factor of two.

Furthermore, semiconductor tapered amplifiers offer superior opportunities for miniaturization. Two miniaturized MOPA setups were investigated, a hybrid integrated version using the same active elements as the bench-top system, and a monolithic version consisting of a single semiconductor device

only. Both systems were assembled on micro-optical benches of $5 \times 25\,\text{mm}$, including beam shaping optics.

In the hybrid integrated MOPAs, a single GRIN lens was used to couple the light from the seed laser into the amplifier. Unfortunately, this setup, which did not contain an optical isolator, was found to introduce excessive reflectivities, causing parasitic amplifier lasing at pump currents as low as $1.5\,\text{A}$ and severely limiting the available gain.

In the monolithic MOPAs, on the other hand, spurious reflectivities could be avoided and high-intensity picosecond pulses with a peak power of up to $19\,\text{W}$ and a good lateral beam quality of $M^2 = 2.6$ could be generated. These devices consist first of a master oscillator DFB section that is operated in gain switched mode, followed by a ridge-waveguide pre-amplifier and a tapered main amplifier which are both pumped with DC current. Since these monolithic MOPAs do not contain any movable parts, they have excellent mechanical and thermal robustness and do not require elaborate assembly, in contrast to the hybrid integrated devices.

Having obtained high-intensity infrared picosecond pulses both from a bench-top and from a miniaturized system, these were used as a fundamental source for second harmonic generation (Sec. 4.2). With both fundamental sources, green picosecond pulses with an energy above $250\,\text{pJ}$ and a duration of below $110\,\text{ps}$ were obtained, which are ideally suited for fluorescence lifetime spectroscopy.

The infrared pulses from the bench-top MOPA are shorter and show stronger spectral dynamics in the vicinity of the Bragg line. This led to a detailed study of the temporal dynamics of the normalized SHG conversion efficiency. However, even with a long crystal with narrow acceptance bandwidth, the pulse shape improved during second harmonic generation, and the generated green pulses are very insensitive to the pump conditions of the master oscillator. They had a deconvoluted peak power of $10\,\text{W}$, exceeding previous green picosecond pulses with variable repetition rate by more than an order of magnitude.

In conclusion, this thesis contains a systematic study of the generation of green picosecond pulses starting from a gain switched infrared laser diode as the master oscillator. The design parameters of the master oscillator and the power amplifier were optimized and the additional challenges connected with miniaturization were identified and solved. Finally, the infrared fundamental pulses were frequency doubled to obtain high-intensity green picosecond pulses, and an investigation of the influence of the fundamental spectral dynamics on the conversion efficiency was made. The resulting green pulse source is excellently suited for fluorescence lifetime spectroscopy.
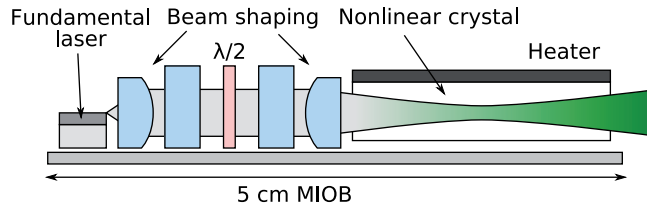
Figure 5.1: Design of a micro-optical bench with hybrid integration of fundamental IR laser diode and nonlinear crystal

5.2 Future Directions

As a next step of miniaturization, the nonlinear crystal can be hybridly integrated with a monolithic MOPA on a 5 cm long micro-optical bench (Fig. 5.1). This has previously been accomplished in CW operation so that the technical aspects of the optical coupling and separate thermal management can be considered solved. Over 1 W optical output power at 490 nm has been demonstrated at a fundamental power of 9.5 W [207].

In this prototype, the fundamental beam was collimated with two cylindrical micro-lenses and focused into the bulk PPLN crystal with another two cylindrical micro-lenses. A λ/2-plate was placed in the collimated beam in order to adjust the polarization direction. The nonlinear crystal was heated by a resistive heater placed on top of the crystal and mounted between two mounting rails along the side of the micro-optical bench.

In gain switched operation, even less optical feedback into the amplifier can be tolerated than in CW operation. Therefore, it seems advisable to place a miniature optical isolator into the collimated beam for a pulsed SHG source.

In a further step, the concept can be generalized to other wavelengths. While the blue spectral range is readily accessible by second harmonic generation of semiconductor lasers [57, 136, 200, 205], it also faces competition from directly blue emitting GaN laser diodes [208] at the power level required for fluorescence lifetime spectroscopy. Therefore, a generation of yellow or orange wavelengths between 550 nm and 630 nm seems most attractive.

This can be achieved in a variety of ways, for example by sum-frequency generation [209] or by second harmonic generation of a Raman laser [129] or a longer-wavelength semiconductor laser [210]. While the first two approaches can both profit from the high-power gain switched DFB lasers developed in this work, the latter enables a direct application of the compact semiconductor MOPA technology presented in this thesis. Periodically poled lithium niobate also offers a high nonlinearity for fundamental wavelengths around 1200 nm, with a normalized spectral acceptance bandwidth of 360 pm cm [192]. There-

fore, dynamic spectral purity is less crucial for SHG to the yellow-orange wavelength range.

However, quantum well diode lasers with gain around 1200 nm are harder to fabricate than those emitting around 1060 nm, because the lattice mismatch between the InGaAs quantum wells and the GaAs substrate becomes very large. However, in addition to quantum-dot devices, various groups have successfully demonstrated quantum well laser diodes around 1200 nm [210–213], so that the construction of tapered semiconductor amplifiers and DFB lasers in this wavelength range seems feasible.

In addition, sum frequency mixing between the green second harmonic pulses and the residual IR fundamental pulses makes the ultraviolet spectral range accessible. Particularly picosecond pulses around 290 nm can be used for fluorescence lifetime spectroscopy of auto-fluorescent biological samples.

On the other hand, the compact, flexible, high-brightness picosecond MOPA developed in this thesis can serve as a seed laser for further amplifier stages in order to realize intense pulse bursts for material processing. The further amplification stages most likely should be based on ytterbium-doped fibers with their high energy storage. The nanojoule pulses emitted by the semiconductor MOPA should saturate the fiber amplifier, allowing a high wall-plug efficiency.

As these examples show, the infrared MOPA and the green picosecond pulse source presented in this work find a number of interesting applications, and can serve as a starting point for the development of further high-performance flexible light sources.

List of Publications

The following scientific publications have been prepared in connection with this thesis:

Articles

S. M. Riecke, S. Schwertfeger, K. Lauritsen, K. Paschke, R. Erdmann, and G. Tränkle, "23 W peak power picosecond pulses from a single-stage all-semiconductor master oscillator power amplifier," *Appl. Phys. B*, vol. 98, no. 2, pp. 295–299, 2010.

S. M. Riecke, K. Lauritsen, R. Erdmann, M. Uebernickel, K. Paschke, and G. Erbert, "Pulse-shape improvement during amplification and second-harmonic generation of picosecond pulses at 531 nm," *Opt. Lett.*, vol. 35, no. 10, pp. 1500–1502, 2010.

S. M. Riecke, K. Posilovic, T. Kettler, S. Seidlitz, V. A. Shchukin, N. N. Ledentsov, K. Lauritsen, and D. Bimberg, "10.7 W peak power picosecond pulses from a high-brightness photonic band crystal laser diode," *Electron. Lett.*, vol. 20, 2010.

S. M. Riecke, H. Wenzel, S. Schwertfeger, K. Lauritsen, K. Paschke, R. Erdmann, and G. Erbert, "Picosecond spectral dynamics of gain-switched DFB lasers," *J. Quant. Electron.*, accepted, 2010.

Conference Talks

K. Lauritsen, S. M. Riecke, M. Langkopf, D. Klemme, C. M. Kaleva, C. Pallassis, S. McNeil, and R. Erdmann, "Fiber amplified and frequency doubled diode lasers as a highly flexible pulse source at 532 nm," in *Proc. SPIE*, vol. 6871, 2008, p. 68711L.

S. M. Riecke, K. Lauritsen, H. Thiem, K. Paschke, and R. Erdmann, "Comparison of a Yb-doped fiber and a semiconductor taper for amplification of picosecond laser pulses," in *Proc. SPIE*, vol. 7212, 2009, p. 72120O.

S. M. Riecke, T. Eckhardt, S. Schwertfeger, A. Klehr, H. Wenzel, and G. Tränkle, "Temperature dependence of picosecond pulse spectra of a DFB laser," in *CLEO Europe – EQEC*, OSA, 2009, p. CB14-5.

S. M. Riecke, K. Lauritsen, R. Erdmann, M. Uebernickel, K. Paschke, and G. Erbert, "Second-harmonic generation of picosecond pulses at 530 nm in bulk PPLN at variable repetition rates," in *CLEO/QELS*. OSA, 2010, p. CWE7.

D. Bimberg, K. Posilovic, V. Kalosha, T. Kettler, D. Seidlitz, V. A. Shchukin, N. N. Ledentsov, S. Riecke, K. Lauritsen, F. Bugge, and M. Weyers, "Tilted waveguide and PBC lasers: Novel cavity designs for narrow far-fields and high brightness," in *Proc. 23rd Annual Meet. IEEE Phot. Soc.*, 2010.

T. Schönau, S. M. Riecke, K. Lauritsen, R. Erdmann, "Amplification of ps-pulses from freely triggerable gain-switched laser diodes at 1062 nm and second harmonic generation in periodically poled lithium niobate," in *Proc. SPIE*, vol. 7917, 2011, p. 7917-6.

Conference Posters

S. M. Riecke, S. Schwertfeger, H. Wenzel, K. Lauritsen, and G. Tränkle, "Temperature dependence of the picosecond pulse performance of a DFB laser," in *Int. Nano-Optoelectron. Workshop*, 2009, p. P88.

Bibliography

[1] T. H. Maiman, "Stimulated optical radiation in ruby," *Nature*, vol. 187, pp. 493–494, 1960.

[2] M. W. Steen, "Laser material processing – an overview," *J. Opt. A*, vol. 5, pp. S3–S7, 2003.

[3] G. P. Agrawal, *Fiber-Optic Communication Systems*. Wiley, 2002.

[4] A. Messica, A. Greenstein, A. Katzir, U. Schiessl, and M. Tacke, "Fiber-optic evanescent wave sensor for gas detection," *Opt. Lett.*, vol. 19, no. 15, pp. 1167–1169, 1994.

[5] J. G. Dunne, "Laser-based speed measuring device," U.S. Patent 5 521 696, 1996.

[6] A. Periasamy and R. M. Clegg, Eds., *FLIM microscopy in biology and medicine*. CRC Press, 2010.

[7] J. R. Lakowicz, *Principles of Fluorescence Spectroscopy*, 3rd ed. Springer, 2006, ch. 4.

[8] K. Carlsson, A. Liljeborg, , R. M. Andersson, and H. Brismar, "Confocal pH imaging of microscopic specimens using fluorescence lifetimes and phase fluorometry: Influence of parameter choice on system performance," *J. Microscopy*, vol. 199, pp. 106–114, 2000.

[9] J. R. Lakowicz, *Principles of Fluorescence Spectroscopy*, 3rd ed. Springer, 2006, ch. 13–15.

[10] W. M. Shih, Z. Gryczynski, J. R. Lakowicz, and J. A. Spudich, "A FRET-based sensor reveals large ATP hydrolysis-induced conformational changes and three distinct states of the molecular motor myosin," *Cell*, vol. 102, no. 5, pp. 683–694, 2000.

[11] S. Rüttinger, R. Macdonald, B. Krämer, F. Koberling, M. Roos, and E. Hildt, "Accurate single-pair Förster resonant energy transfer through

combination of pulsed interleaved excitation, time correlated single-photon counting, and fluorescence correlation spectroscopy," *Journal of Biomedical Optics*, vol. 11, no. 2, p. 024012, 2006.

[12] J. A. Tatum, J. W. Jennings, III, and D. L. MacFarlane, "Compact, inexpensive, visible diode laser source of high repetition rate picosecond pulses," *Rev. Sci. Instrum.*, vol. 63, no. 5, pp. 2950–2953, 1992.

[13] M. Maiwald, H. Schmidt, B. Sumpf, G. Erbert, H.-D. Kronfeldt, and G. Tränkle, "Microsystem 671 nm light source for shifted excitation Raman difference spectroscopy," *Appl. Opt.*, vol. 48, no. 15, pp. 2789–2792, 2009.

[14] M.-C. Lin, T.-T. Shih, P.-H. Tseng, K.-M. Chu, C. Hu, and W.-H. Cheng, "High-performance and low-cost 40-Gb/s CWDM optical modules," *IEEE Trans. Adv. Packaging*, vol. 32, no. 3, pp. 644–649, 2009.

[15] R. N. Hall, G. E. Fenner, J. D. Kingsley, T. J. Soltys, and R. O. Carlson, "Coherent light emission from GaAs junctions," *Phys. Rev. Lett.*, vol. 9, no. 9, pp. 366–368, 1962.

[16] S. M. Sze, *Physics of Semiconductor Devices*, 2nd ed.   Wiley, 1981, ch. 2.4.1.

[17] W. W. Chow, S. W. Koch, and M. Sargent III, *Semiconductor-Laser Physics*.   Springer, 1994, ch. 1-2–1-3.

[18] P. Unger, "Introduction to power diode lasers," in *High-Power Diode Lasers: Fundamentals, Technology, Applications*, R. Diehl, Ed., 2000.

[19] R. D. Dupuis, P. D. Dapkus, R. Chin, J. N. Holonyak, and S. W. Kirchoefer, "Continuous 300 K laser operation of single-quantum-well $Al_xGa_{1-x}As$-GaAs heterostructure diodes grown by metalorganic chemical vapor deposition," *Appl. Phys. Lett.*, vol. 34, no. 4, pp. 265–267, 1979.

[20] J. Davies, *The Physics of Low-Dimensional Semiconductors*.   Cambridge University Press, 1998, ch. 3.6.2.

[21] W. W. Chow, S. W. Koch, and M. Sargent III, *Semiconductor-Laser Physics*.   Springer, 1994, ch. 6.

[22] G. Morthier and P. Vankwinkelberge, *Handbook of Distributed Feedback Laser Diodes*.   Artech House, Inc., 1997, ch. 2.

[23] J. H. Davies, *The Physics of Low-Dimensional Semiconductors.* Cambridge University Press, 1998, ch. 1.7.

[24] W. W. Chow, S. W. Koch, and M. Sargent III, *Semiconductor-Laser Physics.* Springer, 1994, ch. 3-3–3-5.

[25] J. I. Pankove, *Optical Processes in Semiconductors.* Dover Science Books, 1971, p. 392 ff.

[26] G. Erbert, A. Bärwolff, J. Sebastian, and J. Tomm, "High-power broad-area diode lasers and laser bars," in *High-Power Diode Lasers: Fundamentals, Technology, Applications*, R. Diehl, Ed., 2000.

[27] H. Wenzel, B. Sumpf, and G. Erbert, "High-brightness diode lasers," *Comptes Rentus Physique*, vol. 4, no. 6, pp. 649–661, 2003.

[28] H. Wenzel, F. Bugge, M. Dallmer, F. Dittmar, J. Fricke, K. H. Hasler, and G. Erbert, "Fundamental-lateral mode stabilized high-power ridge-waveguide lasers with a low beam divergence," *IEEE Phot. Technol. Lett.*, vol. 20, no. 3, pp. 214–216, 2008.

[29] P. Ressel, G. Erbert, U. Zeimer, K. Hausler, G. Beister, B. Sumpf, A. Klehr, and G. Tränkle, "Novel passivation process for the mirror facets of Al-free active-region high-power semiconductor diode lasers," *IEEE Phot. Technol. Lett.*, vol. 17, no. 5, pp. 962–964, 2005.

[30] T. Takeshita, M. Okayasu, and S. Uehara, "High-output power and fundamental transverse mode InGaAs/GaAs strained-layer laser with ridge waveguide structure," *Japan. J. Appl. Phys.*, vol. 30, no. 6, pp. 1220–1224, 1991.

[31] G. Morthier and P. Vankwinkelberge, *Handbook of Distributed Feedback Laser Diodes.* Artech House, Inc., 1997, ch. 3.5.1–3.5.2.

[32] R. G. Hunsperger, *Integrated Optics – Theory and Technology*, 5th ed. Springer, 2002, ch. 15.

[33] M. Fleming and A. Mooradian, "Spectral characteristics of external-cavity controlled semiconductor lasers," *IEEE J. Quant. Electron.*, vol. 17, no. 1, pp. 44–59, 1981.

[34] D. J. L. Birkin, E. U. Rafailov, W. Sibbett, L. Zhang, Y. Liu, and I. Bennion, "Near-transform-limited picosecond pulses from a gain-switched InGaAs diode laser with fiber Bragg gratings," *Appl. Phys. Lett.*, vol. 79, no. 2, pp. 151–152, 2001.

[35] K. T. Vu, A. Malinowski, M. A. F. Roelens, and D. J. Richardson, "Detailed comparison of injection-seeded and self-seeded performance of a 1060-nm gain-switched Fabry-Pérot laser diode," *IEEE J. Quant. Electron.*, vol. 44, no. 7, pp. 645–651, 2008.

[36] J. Fricke, H. Wenzel, M. Matalla, A. Klehr, and G. Erbert, "980-nm DBR lasers using higher order gratings defined by i-line lithography," *Semicon. Sci. Technol.*, vol. 20, no. 11, pp. 1149–1152, 2005.

[37] M. Achtenhagen, N. V. Amarasinghe, L. Jiang, J. Threadgill, and P. Young, "Spectral properties of high-power distributed Bragg reflector lasers," *J. Lightwave Technol.*, vol. 27, no. 16, pp. 3433–3437, 2009.

[38] J. Fricke, F. Bugge, A. Ginolas, W. John, A. Klehr, M. Matalla, P. Ressel, H. Wenzel, and G. Erbert, "High-power 980-nm broad-area lasers spectrally stabilized by surface Bragg gratings," *IEEE Phot. Technol. Lett.*, vol. 22, no. 5, pp. 284–286, 2010.

[39] F. Koyama, Y. Suematsu, S. Arai, and T.-E. Tawee, "1.5–1.6µm GaInAsP/InP dynamic-single-mode (DSM) lasers with distributed Bragg reflector," *IEEE J. Quant. Electron.*, vol. 19, no. 6, pp. 1042–1051, 1983.

[40] G. Morthier and P. Vankwinkelberge, *Handbook of Distributed Feedback Laser Diodes.* Artech House, Inc., 1997, ch. 4.1.

[41] B.-G. Kim, S.-C. Cho, and A. Shakouri, "The symmetry of the amplified spontaneous emission spectrum in complex coupled DFB lasers," *J. Lightwave Technol.*, vol. 16, no. 6, pp. 1088–1094, 1998.

[42] H. Wenzel, A. Klehr, M. Braun, F. Bugge, G. Erbert, J. Fricke, A. Knauer, P. Ressel, B. Sumpf, M. Weyers, and G. Tränkle, "Design and realization of high-power DFB lasers," in *Proc. SPIE*, vol. 5594, 2004, pp. 110–123.

[43] L. A. Coldren and S. W. Corzine, *Diode Lasers and Photonic Integrated Circuits.* Wiley, 1995, ch. 3.7.

[44] J. E. A. Whiteaway, G. H. B. Thompson, A. J. Collar, and C. J. Armistead, "The design and assessment of λ/4 phase-shifted DFB laser structures," *IEEE J. Quant. Electron.*, vol. 25, no. 6, pp. 1261–1279, 1989.

[45] R. Güther, S. Polze, and G. Korn, "Mit dem Lloydspiegel hergestellte korrigierte holographische Konkavgitter," *Optik*, vol. 72, no. 2, pp. 71–74, 1985.

[46] A. Knauer, G. Erbert, R. Staske, B. Sumpf, H. Wenzel, and M. Weyers, "High-power 808-nm lasers with a super-large optical cavity," *Semicond. Sci. Technol.*, vol. 20, pp. 621–624, 2005.

[47] A. Klehr, J. Fricke, A. Knauer, G. Erbert, M. Walther, R. Wilk, M. Mikulics, and M. Koch, "High-power monolithic two-mode DFB laser diodes for the generation of THz radiation," *IEEE J. Sel. Top. Quant. Electron.*, vol. 14, no. 2, pp. 289–294, 2008.

[48] G. B. Stringfellow, *Organometallic Vapor-Phase Epitaxy – Theory and Practice*, 2nd ed.   Academic Press, 1999.

[49] O. Brox, J. Wiedmann, F. Scholz, F. Bugge, J. Fricke, A. Klehr, T. Laurent, P. Ressel, H. Wenzel, G. Erbert, and G. Tränkle, "Integrated 1060 nm MOPA pump source for high-power light emitters in display technology," in *Proc. SPIE*, vol. 6909, 2008, p. 69091G.

[50] A. Maaßdorf and M. Weyers, "In-situ etching of GaAs/Al$_x$Ga$_{1-x}$As by CBr$_4$," *J. Cryst. Growth*, vol. 310, pp. 4754–4756, 2008.

[51] H. Ito and T. Ishibashi, "Selective and nonselective chemical etching of InGa(As)P/GaAs heterostructures," *J. Electrochem. Soc.*, vol. 142, no. 10, pp. 3383–3386, 1995.

[52] R. E. Williams, *Gallium Arsenide Processing Techniques.*   Artech House, 1984, ch. 9.3.

[53] M. Okai, M. Suzuki, and T. Taniwatari, "Strained multiquantum-well corrugation-pitch-modulated distributed feedback laser with ultranarrow (3.6 kHz) spectral linewidth," *Electron. Lett.*, vol. 29, no. 19, pp. 1696–1697, 1993.

[54] S. Spießberger, M. Schiemangk, A. Wicht, H. Wenzel, O. Brox, and G. Erbert, "Narrow linewidth DFB lasers emitting near a wavelength of 1064 nm," *IEEE J. Lightwave Technol.*, vol. 28, no. 17, pp. 2611–2616, 2010.

[55] H. Wenzel, J. Fricke, A. Klehr, A. Knauer, and G. Erbert, "High-power 980-nm DFB RW lasers with a narrow vertical far field," *IEEE Phot. Technol. Lett.*, vol. 18, no. 6, pp. 737–739, 2006.

[56] J. Eichler, L. Dünkel, and B. Eppich, "Die Strahlqualität von Lasern – Wie bestimmt man Beugungsmaßzahl und Strahlduchmesser in der Praxis?" *Laser Technik Journal*, vol. 1, no. 2, pp. 63–66, 2004.

[57] M. Uebernickel, R. Güther, G. Blume, C. Fiebig, K. Paschke, and G. Erbert, "Study of the properties of the SHG with diode lasers," *Appl. Phys. B*, vol. 99, no. 3, pp. 457–464, 2010.

[58] Z. Yang, Y. Zhao, and X. Zhu, "Transition between nonthermal and thermal ablation of metallic targets under the strike of high-fluence ultrashort laser pulses," *Appl. Phys. Lett.*, vol. 88, p. 094101, 2006.

[59] B. Sallé, O. Gobert, P. Meynadier, M. Perdrix, G. Petite, and A. Semerok, "Femtosecond and picosecond laser microablation: ablation efficiency and laser microplasma expansion," *Appl. Phys. A*, vol. 69, pp. S381–S383, 1999.

[60] J. P. Colombier, P. Combis, A. Rosenfeld, I. V. Hertel, E. Audouard, and R. Stoian, "Optimized energy coupling at ultrafast laser-irradiated metal surfaces by tailoring intensity envelopes: Consequences for material removal from Al samples," *Phys. Rev. B*, vol. 74, p. 224106, 2006.

[61] M. Wahl, F. Koberling, M. Patting, H. Rahn, and R. Erdmann, "Time-resolved confocal fluorescence imaging and spectroscopy system with single molecule sensitivity and sub-micrometer resolution," *Curr. Pharmaceut. Biotechnol.*, vol. 5, pp. 299–308, 2004.

[62] M. Kress, T. Meier, R. Steiner, F. Dolp, R. Erdmann, U. Ortmann, and A. Rück, "Time-resolved microspectrofluometry and fluorescence lifetime imaging of photosensitizers using picosecond pulsed diode lasers in laser scanning microscopes," *J. Biomed. Opt.*, vol. 8, no. 1, pp. 26–32, 2003.

[63] M. Kuramoto, N. Kitajima, H. Guo, Y. Furushima, M. Ikeda, and H. Yokoyama, "Two-photon fluorescence bioimaging with an all-semiconductor laser picosecond pulse source," *Opt. Lett.*, vol. 32, no. 18, pp. 2726–2728, 2007.

[64] P. R. Herman, S. Rezaei, D. Esser, A. Hosseini, and J. Li, "Ablation dynamics in burst-train femtosecond laser machining of high aspect ratio holes in glass," in *CLEO/QELS*. OSA, 2010, p. JTuC2.

[65] D. Bimberg, K. Ketterer, E. H. Böttcher, and E. Schöll, "Gain modulation of unbiased semiconductor lasers: ultrashort light-pulse generation in the $0.8\,\mu m$ – $1.4\,\mu m$ wavelength range," *Int. J. Electron.*, vol. 60, no. 1, pp. 23–45, 1986.

[66] P. Torphammar and S. T. Eng, "Picosecond pulse generation in semiconductor lasers using resonance oscillation," *Electron. Lett.*, vol. 16, no. 15, pp. 587–589, 1980.

[67] B. Lanz, S. Vainshtein, and J. Kostamovaara, "High power gain-switched laser diode using a superfast GaAs avalanche transistor for pumping," *Appl. Phys. Lett.*, vol. 89, no. 081122, 2006.

[68] J. AuYeung, "Picosecond optical pulse generation at gigahertz rates by direct modulation of a semiconductor laser," *Appl. Phys. Lett.*, vol. 38, no. 5, pp. 308–310, 1981.

[69] P. Paulus, R. Langenhorst, and D. Jäger, "Generation and optimum control of picosecond optical pulses from gain-switched semiconductor lasers," *IEEE J. Quant. Electron.*, vol. 24, no. 8, pp. 1519–1523, 1988.

[70] E. Schöll, D. Bimberg, H. Schumacher, and P. Landsberg, "Kinetics of picosecond pulse generation in semiconductor lasers with bimolecular recombination at high current injection," *IEEE J. Quant. Electron.*, vol. 20, no. 4, pp. 394–399, 1984.

[71] K. Petermann, *Diode modulation and noise.* Kluwer Academic Publishers, 1991, ch. 4.

[72] S. Tarucha and K. Otsuka, "Response of semiconductor laser to deep sinusoidal injection current modulation," *IEEE J. Quant. Electron.*, vol. 17, no. 5, pp. 810–816, 1981.

[73] E. U. Rafailov, D. Birkin, E. A. Avrutin, and W. Sibbett, "Short-pulse generation from single-mode InGaAs/GaAs laser diodes by large-signal RF modulation," *Microwave Opt. Technol. Lett.*, vol. 18, no. 5, pp. 354–356, 1998.

[74] P. Downey, J. Bowers, R. Tucker, and E. Agyekum, "Picosecond dynamics of a gain-switched InGaAsP laser," *IEEE J. Quant. Electron.*, vol. 23, no. 6, pp. 1039–1047, 1987.

[75] N. Onodera, H. Ito, and H. Inaba, "Fourier-transform-limited, single-mode picosecond optical pulse generation by a distributed feedback InGaAsP diode laser," *Appl. Phys. Lett.*, vol. 45, no. 8, pp. 843–845, 1984.

[76] T. Sogawa and Y. Arakawa, "Picosecond lasing dynamics of gain-switched quantum well lasers and its dependence on quantum well structures," *IEEE J. Quant. Electron.*, vol. 27, no. 6, pp. 1648–1654, 1991.

[77] G. J. Aspin, J. E. Carrol, and R. G. Plumb, "The effect of cavity length on picosecond pulse generation with highly RF modulated AlGaAs double heterostructure lasers," *Appl. Phys. Lett.*, vol. 39, no. 11, pp. 860–861, 1981.

[78] D. J. Derickson, R. J. Helkey, A. Mar, J. R. Karin, J. G. Wasserbauer, and J. E. Bowers, "Short pulse generation using multisegment mode-locked semiconductor-lasers," *IEEE J. Quant. Electron.*, vol. 28, no. 10, pp. 2186–2202, 1992.

[79] D. Z. Tsang, J. N. Walpole, Z. L. Liau, S. H. Groves, and V. Diadiuk, "Q-switching of low-threshold buried-heterostructure diode lasers at 10 GHz," *Appl. Phys. Lett.*, vol. 45, no. 3, pp. 204–206, 1984.

[80] Y. Arakawa, A. Larsson, J. Paslaski, and A. Yariv, "Active Q-switching in a GaAs/AlGaAs multiquantum well laser with an intracavity monolithic loss modulator," *Appl. Phys. Lett.*, vol. 48, no. 9, pp. 561–563, 1986.

[81] E. L. Portnoi, G. B. Venus, A. A. Khazan, I. M. Gadjiev, A. Y. Shmarcev, J. Frahm, and D. Kuhl, "Superhigh-power picosecond optical pulses from Q-switched diode laser," *IEEE J. Sel. Top. Quant. Electron.*, vol. 3, no. 2, pp. 256–260, 1997.

[82] D. S. Yee, Y. A. Leem, D. C. Kim, Y. S. Baek, S. B. Kim, and K. H. Park, "Self-pulsations in a multi-section distributed feedback laser diode," *J. Korean Phys. Soc.*, vol. 42, pp. S212–S215, 2004.

[83] P. P. Vasil'ev, "Ultrashort pulse generation in diode lasers," *Opt. Quant. Electron.*, vol. 24, no. 8, pp. 801–824, 1992.

[84] M. C. Wu, Y. K. Chen, T. Tanbun-Ek, R. A. Logan, M. A. Chin, and G. Raybon, "Transform-limited 1.4 ps optical pulses from a monolithic colliding-pulse mode-locked quantum well laser," *Appl. Phys. Lett.*, vol. 57, no. 8, pp. 759–761, 1990.

[85] R. Kaiser and B. Hüttl, "Monolithic 40-GHz mode-locked MQW DBR lasers for high-speed optical communication systems," *IEEE J. Sel. Top. Quant. Electron.*, vol. 13, no. 1, pp. 125–135, 2007.

[86] A. Olsson and C. Tang, "Active mode locking of linear and ring external-cavity semiconductor lasers," *IEEE J. Quant. Electron.*, vol. 17, no. 10, pp. 1977–1978, 1981.

[87] M. G. Davis and R. F. O'Dowd, "A new large-signal dynamic model for multielectrode DFB lasers based on the transfer matrix method," *IEEE Phot. Technol. Lett.*, vol. 4, no. 8, pp. 838–840, 1992.

[88] A. J. Lowery, "New dynamic model for multimode chirp in DFB semiconductor lasers," *IEE Proc. Optoelectron.*, vol. 137, no. 5, pp. 293–300, 1990.

[89] L. M. Zhang and J. E. Carroll, "Large-signal dynamic model of the DFB laser," *IEEE J. Quant. Electron.*, vol. 28, no. 3, pp. 604–611, 1992.

[90] W. Fang, A. Hsu, S. L. Chuang, T. Tanbun-Ek, and A. M. Sergent, "Measurement and modeling of distributed-feedback lasers with spatial hole burning," *IEEE J. Quant. Electron.*, vol. 3, no. 2, pp. 547–554, 1997.

[91] H. Kogelnik and C. V. Shank, "Coupled-wave theory of distributed feedback lasers," *J. Appl. Phys.*, vol. 43, no. 5, pp. 2327–2335, 1972.

[92] A. M. Shams-Zadeh-Amiri, J. Hong, X. Li, and W.-P. Huang, "Second- and higher-order resonant gratings with gain or loss – part 1: Green's function analysis," *IEEE J. Quant. Electron.*, vol. 36, no. 12, pp. 1421–1430, 2000.

[93] R. G. Baets, K. David, and G. Morthier, "On the distinctive features of gain coupled DFB lasers and DFB lasers with second-order grating," *IEEE J. Quant. Electron.*, vol. 29, no. 6, pp. 1792–1798, 1993.

[94] T. Makino and J. Glinski, "Effects of radiation loss on the performance of second-order DFB semiconductor lasers," *IEEE J. Quant. Electron.*, vol. 24, no. 1, pp. 79–82, 1988.

[95] W. Streifer, R. D. Burnham, and D. R. Scifres, "Effect of external reflectors on longitudinal modes of distributed feedback lasers," *IEEE J. Quant. Electron.*, vol. 11, no. 4, pp. 154–161, 1975.

[96] M. Radziunas, H.-J. Wünsche, B. Sartorius, O. Brox, D. Hoffmann, K. R. Schneider, and D. Marcenac, "Modeling self-pulsating DFB lasers with an integrated phase-tuning section," *IEEE J. Quant. Electron.*, vol. 36, no. 9, pp. 1026–1034, 2000.

[97] C. Henry, "Theory of spontaneous emission noise in open resonators and its application to lasers and optical amplifiers," *J. Lightwave Technol.*, vol. 4, no. 3, pp. 288–297, 1986.

[98] N. Dorgu, "Gain switching characteristics of quantum well laser in two level rate equations," *J. Optoelectron. Adv. Mat.*, vol. 9, no. 8, pp. 2400–2403, 2007.

[99] D. Marcuse and T.-P. Lee, "On approximate analytical solutions of rate equations for studying transient spectra of injection lasers," *IEEE J. Quant. Electron.*, vol. 19, no. 9, pp. 1397–1406, 1983.

[100] B. J. Thedrez and C. H. Lee, "A reassessment of standard rate equations for low facet reflectivity semiconductor lasers using traveling wave rate equations," *IEEE J. Quant. Electron.*, vol. 28, no. 12, pp. 2706–2713, 1992.

[101] J. P. Loehr, *Physics of Strained Quantum Well Lasers.* Kluwer Academic Publishers, 1998, ch. 6.5.

[102] A. Einstein, "Strahlungs-emission und -absorption nach der quantentheorie," *Verhandlungen der Deutschen Phys. Ges.*, vol. 18, pp. 318–323, 1916.

[103] L. A. Coldren and S. W. Corzine, *Diode Lasers and Photonic Integrated Circuits*, ser. Wiley Series in Microwave and Optical Engineering. Wiley, 1995, ch. A6.

[104] ——, *Diode Lasers and Photonic Integrated Circuits*, ser. Wiley Series in Microwave and Optical Engineering. Wiley, 1995, ch. 4.5.

[105] B. Tromborg, H. E. Lassen, and H. Olesen, "Traveling wave analysis of semiconductor lasers: modulation responses, mode stability and quantum mechanical treatment of noise spectra," *IEEE J. Quant. Electron.*, vol. 30, no. 4, pp. 939–956, 1994.

[106] H. Wenzel, P. Crump, A. Pietrzak, C. Roder, X. Wang, and G. Erbert, "The analysis of factors limiting the maximum output power of broad-area laser diodes," *Opt. Quant. Electron.*, vol. 41, no. 9, pp. 645–652, 2010.

[107] D. J. Channin, "Effect of gain saturation on injection laser switching," *J. Appl. Phys.*, vol. 50, no. 6, pp. 3858–3860, 1979.

[108] J. Wang and H. C. Schweizer, "A quantitative comparison of the classical rate-equation model with the carrier heating model on dynamics of the quantum-well laser: The role of carrier energy relaxation, electron-hole interaction, and Auger effect," *IEEE J. Quant. Electron.*, vol. 33, no. 8, pp. 1350–1359, 1997.

[109] J. E. Bowers, B. R. Hemenway, A. H. Gnauck, and D. P. Wilt, "High-speed InGaAsP constricted-mesa lasers," *IEEE J. Quant. Electron.*, vol. 22, no. 6, pp. 833–844, 1986.

[110] J. Huang and L. W. Casperson, "Gain and saturation in semiconductor lasers," *Opt. Quant. Electron.*, vol. 25, pp. 369–390, 1993.

[111] J. P. Loehr, *Physics of Strained Quantum Well Lasers.* Kluwer Academic Publishers, 1998, ch. 2.6.

[112] ——, *Physics of Strained Quantum Well Lasers.* Kluwer Academic Publishers, 1998, ch. 1.2.

[113] P. Enders, A. Bärwolff, M. Woerner, and D. Suisky, "k·p theory of energy bands, wave functions, and optical selection rules in strained tetrahedral semiconductors," *Phys. Rev. B*, vol. 51, no. 23, pp. 16 695–16 704, 1995.

[114] U. Bandelow, R. Hunlich, and T. Koprucki, "Simulation of static and dynamic properties of edge-emitting multiple-quantum-well lasers," *IEEE J. Sel. Top. Quant. Electron.*, vol. 9, no. 3, pp. 798–806, 2003.

[115] W. W. Chow, P. M. Smowton, P. Blood, A. Girndt, F. Jahnke, and S. W. Koch, "Comparison of experimental and theoretical GaInP quantum well gain spectra," *Appl. Phys. Lett.*, vol. 71, no. 2, pp. 157–159, 1997.

[116] P. M. Enders, "Enhancement and spectral shift of optical gain in semiconductors from non-Markovian intraband relaxation," *IEEE J. Quant. Electron.*, vol. 33, no. 4, pp. 580–588, 1997.

[117] J. Hader, J. V. Moloney, S. W. Koch, and W. W. Chow, "Microscopic modeling of gain and luminescence in semiconductors," *IEEE J. Sel. Top. Quant. Electron.*, vol. 9, no. 3, pp. 688–697, 2003.

[118] M. Yamada, S. Ogita, M. Yamagishi, K. Tabata, N. Nakaya, M. Asada, and Y. Suematsu, "Polarization-dependent gain in GaAs/AlGaAs multi-quantum-well lasers: Theory and experiment," *Appl. Phys. Lett.*, vol. 45, no. 4, pp. 324–325, 1984.

[119] H. Wenzel, G. Erbert, and P. M. Enders, "Improved theory of the refractive-index change in quantum-well lasers," *IEEE J. Sel. Top. Quant. Electron.*, vol. 5, no. 3, pp. 637–642, 1999.

[120] R. Zimmermann, *Many-Particle Theory of Highly Excited Semiconductors.* Teubner, 1987.

[121] S. N. Vainshtein, G. S. Simin, and J. T. Kostamovaara, "Deriving of single intensive picosecond optical pulses from a high-power gain-switched laser diode by spectral filtering," *J. Appl. Phys.*, vol. 84, no. 8, pp. 4109–4113, 1998.

[122] K. Kamite, H. Ishikawa, and H. Imai, "Single-longitudinal-mode operation of DFB lasers in gain-switched operating conditions," *Electron. Lett.*, vol. 24, no. 15, pp. 933–934, 1988.

[123] M. Nakazawa, K. Suzuki, and Y. Kimura, "Transform-limited pulse generation in the gigahertz region from a gain-switched distributed-feedback laser diode using spectral windowing," *Opt. Lett.*, vol. 15, no. 12, pp. 715–717, 1990.

[124] T. Niemi, J.-G. Zhang, and H. Ludvigsen, "Effect of optical filtering on pulses generated with a gain-switched DFB-laser," *Opt. Comm.*, vol. 192, pp. 339–345, 2001.

[125] U. Bandelow, R. Schatz, and H.-J. Wünsche, "A correct single-mode photon rate equation for multisection lasers," *IEEE Phot. Technol. Lett.*, vol. 8, no. 5, pp. 614–616, 1996.

[126] R. N. Day, "Visible fluorescent proteins for FRET-FLIM," in *FLIM Microscopy in Biology and Medicine*, A. Periasamy and R. M. Clegg, Eds. CRC Press, 2010, ch. 3.

[127] R. Häring, T. Schmitt, A.-R. Bellancourt, F. Lison, K. Lauritsen, R. Erdmann, and W. Kaenders, "10 W peak power from a gain-switched picosecond all-semiconductor laser," in *Proc. SPIE*, vol. 5707, no. 1, 2005, pp. 302–308.

[128] K. Lauritsen, S. Riecke, M. Langkopf, D. Klemme, C. M. Kaleva, C. Pallassis, S. McNeil, and R. Erdmann, "Fiber amplified and frequency doubled diode lasers as a highly flexible pulse source at 532 nm," in *Proc. SPIE*, vol. 6871, 2008, p. 68711L.

[129] D. A. Chestnut, S. V. Popov, J. R. Taylor, and T. D. Roberts, "Second-harmonic generation to the green and yellow using picosecond fiber pump sources and periodically poled waveguides," *Appl. Phys. Lett.*, vol. 88, p. 071113, 2006.

[130] C. Alegria, Y. Jeong, C. Codemard, J. K. Sahu, J. A. Alvarez-Chavez, L. Fu, M. Ibsen, and J. Nilsson, "83-W single-frequency narrow-linewidth MOPA using large-core erbium-ytterbium co-doped fiber," *IEEE Phot. Technol. Lett.*, vol. 16, no. 8, pp. 1825–1827, 2004.

[131] N. Laurand, S. Calves, M. D. Dawson, S. Bouchoule, J.-C. Harmand, and J. Decobert, "Tunable doped-fibre vertical cavity surface emitting laser," *Electron. Lett.*, vol. 45, no. 17, pp. 887–888, 2009.

[132] P. B. Hansen, J. M. Wiesenfeld, G. Eisenstein, R. S. Tucker, and G. Raybon, "Repetition-rate dependence of gain compression in InGaAsP optical amplifiers using picosecond optical pulses," *IEEE J. Quant. Electron.*, vol. 25, no. 12, pp. 2611–2620, 1989.

[133] H. Ghafouri-Shiraz, P. W. Tan, and T. Aruga, "Picosecond pulse amplification in tapered-waveguide laser-diode amplifiers," *IEEE J. Sel. Top. Quant. Electron.*, vol. 3, no. 2, pp. 210–217, 1997.

[134] S. Riecke, S. Schwertfeger, K. Lauritsen, K. Paschke, R. Erdmann, and G. Tränkle, "23 W peak power picosecond pulses from a single-stage all-semiconductor master oscillator power amplifier," *Appl. Phys. B*, vol. 98, no. 2, pp. 295–299, 2010.

[135] M. Poelker, "High power gain-switched diode laser master oscillator and amplifier," *Appl. Phys. Lett.*, vol. 67, no. 19, pp. 2762–2764, 1995.

[136] D. Woll, J. Schumacher, A. Robertson, M. A. Tremont, R. Wallenstein, M. Katz, D. Eger, and A. Englander, "250 mW of coherent blue 460-nm light generated by single-pass frequency doubling of the output of a mode-locked high-power diode laser in periodically poled KTP," *Opt. Lett.*, vol. 27, no. 12, pp. 1055–1057, 2002.

[137] R. Paschotta, J. Nilsson, A. C. Tropper, and D. C. Hanna, "Ytterbium-doped fiber amplifiers," *IEEE J. Quant. Electron.*, vol. 33, no. 7, pp. 1049–1056, 1997.

[138] J. N. Walpole, "Semiconductor amplifiers and lasers with tapered gain regions," *Optical and Quantum Electronics*, vol. 28, no. 6, pp. 623–645, 1996.

[139] T. J. Kane, W. J. Kozlovsky, and R. L. Byer, "62-dB-gain multiple-pass slab geometry Nd:YAG amplifier," *Opt. Lett.*, vol. 11, no. 4, pp. 216–218, 1986.

[140] J. Kawanaka, K. Yamakawa, H. Nishioka, and K. Ueda, "30-mJ, diode-pumped, chirped-pulse Yb:YLF regenerative amplifier," *Opt. Lett.*, vol. 28, no. 21, pp. 2121–2123, 2003.

Bibliography

[141] Y. Stepanenko and C. Radzewicz, "High-gain multipass noncollinear optical parametric chirped pulse amplifier," *Appl. Phys. Lett.*, vol. 86, p. 211120, 2005.

[142] M. N. Islam, "Raman amplifiers for telecommunications," *IEEE J. Sel. Top. Quant. Electron.*, vol. 8, no. 3, pp. 548–559, 2002.

[143] J. M. Tang and K. A. Shore, "Strong picosecond optical pulse propagation in semiconductor optical amplifiers at transparency," *IEEE J. Quant. Electron.*, vol. 34, no. 7, pp. 1263–1269, 1998.

[144] M. J. Conelly, "Wideband semiconductor optical amplifier steady-state numerical model," *IEEE J. Quant. Electron.*, vol. 37, no. 3, pp. 439–447, 2001.

[145] E. Gehrig and O. Hess, "Spatio-temporal dynamics of light amplification and amplified spontaneous emission in high-power tapered semiconductor laser amplifiers," *IEEE J. Quant. Electron.*, vol. 37, no. 10, pp. 1345–1355, 2001.

[146] S. Kück, L. Fornasiero, E. Mix, and G. Huber, "Excited state absorption and stimulated emission of Nd^{3+} in crystals. Part I: $Y_3Al_5O_{12}$, $YAlO_3$, and Y_2O_3," *Appl. Phys. B*, vol. 67, no. 2, pp. 151–156, 1998.

[147] H. M. Pask, R. J. Carman, D. C. Hanna, A. C. Tropper, C. J. Mackechnie, P. R. Barber, and J. M. Dawes, "Ytterbium-doped silica fiber lasers: versatile sources for the 1–1.2 µm region," *IEEE J. Sel. Top. Quant. Electron.*, vol. 1, no. 1, pp. 2–13, 1995.

[148] J. Limpert, A. Liem, T. Gabler, H. Zellmer, A. Tünnermann, S. Unger, S. Jetschke, and H.-R. Müller, "High-average-power picosecond Yb-doped fiber amplifier," *Opt. Lett.*, vol. 26, no. 23, pp. 1849–1851, 2001.

[149] S. Kanzelmeyer, private communication, 2010, Laser Zentrum Hannover e.V.

[150] X.-H. Fang, M.-L. Hu, B.-W. Liu, C.-Y. Wang, and A. M. Zheltikov, "Generation of 150 MW, 110 fs pulses by phase-locked amplification in multicore photonic crystal fiber," *Opt. Lett.*, vol. 35, no. 15, pp. 2326–2328, 2010.

[151] G. L. Bourdet, "Comparison of pulse amplification performances in longitudinally pumped ytterbium doped materials," *Opt. Comm.*, vol. 200, pp. 331–342, 2001.

110

[152] C.-H. Lee and P. J. Delfyett, "Limits on amplification of picosecond pulses by using semiconductor laser traveling-wave amplifiers," *IEEE J. Quant. Electron.*, vol. 27, no. 5, pp. 1110–1114, 1991.

[153] K. E. Mattsson, "Photo darkening of ytterbium fiber lasers and amplifiers," in *CLEO/QELS*. OSA, 2010, p. CMGG1.

[154] S. Jetschke, S. Unger, U. Röpke, and J. Kirchhof, "Photodarkening in Yb-doped fibers: Experimental evidence of equilibrium states depending on the pump power," *Opt. Expr.*, vol. 15, no. 22, pp. 14 838–14 843, 2007.

[155] M. J. Söderlund, J. J. Montiel i Ponsoda, J. Koplow, and S. Honkanen, "Thermal bleaching of photodarkening-induced loss in ytterbium-doped fibers," *Opt. Lett.*, vol. 34, no. 17, pp. 2637–2639, 2009.

[156] N. Inoue, A. Shirakawa, and K. Ueda, "Photo-darkening and photo-bleaching of Yb-doped fibers by laser diodes," in *CLEO/QELS*. OSA, 2010, p. CMGG5.

[157] P. Dupriez, A. Piper, A. Malinowski, J. K. Sahu, M. Ibsen, B. C. Thomsen, Y. Jeong, L. M. B. Hickey, M. N. Zervas, J. Nilsson, and D. J. Richardson, "High average power, high repetition rate, picosecond pulsed fiber master oscillator power amplifier source seeded by a gain-switched laser diode at 1060 nm," *IEEE Phot. Technol. Lett.*, vol. 18, no. 9, pp. 1013–1015, 2006.

[158] A. Uskov, J. Mørk, and J. Mark, "Theory of short-pulse gain saturation in semiconductor laser amplifiers," *IEEE Phot. Technol. Lett.*, vol. 4, no. 5, pp. 443–446, 1992.

[159] D. C. Hall, M. R. Surette, L. Goldberg, and D. Mehuys, "Carrier-induced lensing in broad-area and tapered semiconductor amplifiers," *IEEE Phot. Technol. Lett.*, vol. 6, no. 2, pp. 186–188, 1994.

[160] A. I. Bawamia, B. Eppich, K. Paschke, H. Wenzel, F. Schnieder, G. Erbert, and G. Tränkle, "Experimental determination of the thermal lens parameters in a broad area semiconductor laser amplifier," *Appl. Phys. B*, vol. 97, no. 1, pp. 95–101, 2009.

[161] R. J. Lang, D. Mehuys, D. F. Welch, and L. Goldberg, "Spontaneous filamentation in broad-area diode laser amplifiers," *IEEE J. Quant. Electron.*, vol. 30, no. 3, pp. 685–694, 1994.

[162] L. Goldberg, D. Mehuys, M. R. Surette, and D. C. Hall, "High-power, near-diffraction-limited large-area traveling-wave semiconductor amplifiers," *IEEE J. Quant. Electron.*, vol. 29, no. 6, pp. 2028–2043, 1993.

[163] S. Schwertfeger, J. Wiedmann, B. Sumpf, A. Klehr, F. Dittmar, A. Knauer, G. Erbert, and G. Tränkle, "7.4 W continuous-wave output power of master oscillator power amplifier system at 1083 nm," *Electron. Lett.*, vol. 42, no. 6, pp. 346–347, 2006.

[164] K. Sakai, N. Shimada, K. Shibata, Y. Hanmaki, S. Itakura, M. Imaki, T. Yagi, and Y. Hirano, "High-power 1.06 μm near-diffraction-limited planar tapered amplifier injected with seed light through a fiber biconical microlens," *J. Lightwave Technol.*, vol. 26, no. 6, pp. 710–718, 2008.

[165] W. Susaki, S. Ukawa, and M. Tanaka, "Carrier lifetime in compressively strained InGaAs quantum well lasers with InGaAsP barrier/waveguide layers grown on GaAs," *physica status solidi (c)*, vol. 3, no. 3, pp. 683–687, 2006.

[166] T. Saitoh and T. Mukai, "Gain saturation characteristics of traveling-wave semiconductor laser amplifiers in short optical pulse amplification," *IEEE J. Quant. Electron.*, vol. 26, no. 12, pp. 2086–2094, 1990.

[167] A. Mecozzi and J. Mørk, "Saturation induced by picosecond pulses in semiconductor optical amplifiers," *J. Opt. Soc. Am. B*, vol. 14, no. 4, pp. 761–770, 1997.

[168] T. Schönau, K. Lauritsen, and R. Erdmann, "Amplification of ps-pulses from freely triggerable gain-switched laser diodes at 1062 nm and second harmonic generation in periodically poled lithium niobate," in *Proc. SPIE*, vol. 7917, 2011.

[169] A. Sahm, H. Thiem, K. Paschke, J. Fricke, A. Knauer, and G. Erbert, "4.5 W hybrid integrated master-oscillator power-amplifier at 976 nm on micro-optical bench," in *Proc. SPIE*, vol. 7221, 2009, p. 72210W.

[170] K. Kubodera and K. Otsuka, "Diode-pumped miniature solid-state laser: design considerations," *Appl. Opt.*, vol. 16, no. 10, pp. 2747–2752, 1977.

[171] C. Gomez-Reino, M. V. Perez, and C. Bao, *Gradient-Index Optics.* Springer, 2002.

[172] D. Kühlke, *Optik.* Verlag Harri Deutsch, 2007, ch. 7.2.

[173] D. Jedrzejczyk, O. Brox, F. Bugge, J. Fricke, A. Ginolas, K. Paschke, H. Wenzel, and G. Erbert, "High-power distributed-feedback tapered master oscillator power amplifiers emitting at 1064 nm," in *Proc. SPIE*, vol. 7583, 2010, p. 758317.

[174] J. G. Mendoza-Alvarez, F. D. Nunes, and N. B. Patel, "Refractive index dependence on free carriers for GaAs," *J. Appl. Phys.*, vol. 51, no. 8, pp. 4365–4367, 1980.

[175] R. Peng, L. Guo, X. Zhang, F. Li, Q. Cui, Y. Bo, Q. Peng, D. Cui, Z. Xu, and L. Tang, "34 W picosecond laser and second-harmonic generation experiment," *Opt. Comm.*, vol. 282, pp. 611–613, 2009.

[176] S. M. Riecke, K. Lauritsen, R. Erdmann, M. Uebernickel, K. Paschke, and G. Erbert, "Pulse-shape improvement during amplification and second-harmonic generation of picosecond pulses at 531 nm," *Opt. Lett.*, vol. 35, no. 10, pp. 1500–1502, 2010.

[177] H. K. Nguyen, M. H. Hu, N. Nishiyama, N. J. Visovsky, Y. Li, K. Song, X. Liu, J. Gollier, J. L. C. Hughes, R. Bhat, and C.-E. Zah, "107-mW low-noise green-light emission by frequency doubling of a reliable 1060-nm DFB semiconductor laser diode," *IEEE Phot. Technol. Lett.*, vol. 18, no. 5, pp. 682–684, 2006.

[178] M. Achtenhagen, W. D. Bragg, J. O'Daniel, and P. Young, "Efficient green-light generation from waveguide crystal," *Electron. Lett.*, vol. 44, no. 16, pp. 985–986, 2008.

[179] P. A. Franken and J. F. Ward, "Optical harmonics and nonlinear phenomena," *Rev. Mod. Phys.*, vol. 35, no. 1, pp. 23–39, 1963.

[180] D. A. Kleinman and R. C. Miller, "Dependence of second-harmonic generation on the position of the focus," *Phys. Rev.*, vol. 148, no. 1, pp. 302–312, 1966.

[181] J. A. Armstrong, N. Bloembergen, J. Ducuing, and P. S. Pershan, "Interactions between light waves in a nonlinear dielectric," *Phys. Rev.*, vol. 127, no. 6, pp. 1918–1939, 1962.

[182] D. A. Kleinman, A. Ashkin, and G. D. Boyd, "Second-harmonic generation of light by focused laser beams," *Phys. Rev.*, vol. 145, pp. 338–379, 1966.

Bibliography

[183] P. A. Franken, A. E. Hill, C. W. Peters, and G. Weinreich, "Generation of optical harmonics," *Phys. Rev. Lett.*, vol. 7, no. 4, pp. 118–119, 1961.

[184] G. D. Boyd and D. A. Kleinman, "Parametric interaction of focused Gaussian light beams," *J. Appl. Phys.*, vol. 39, no. 80, pp. 3597–3639, 1968.

[185] S. Lavi, R. Prochaska, and E. Keren, "Generalized beam parameters and transformation laws for partially coherent light," *Appl. Opt.*, vol. 27, no. 17, pp. 3696–3703, 1988.

[186] S. Helmfrid and G. Arvidsson, "Second-harmonic generation in quasi-phase-matching waveguides with a multimode pump," *J. Opt. Soc. Am. B*, vol. 8, no. 11, pp. 2326–2330, 1991.

[187] M. A. Dreger and J. K. McIver, "Second-harmonic generation in a non-linear, anisotropic medium with diffraction and depletion," *J. Opt. Soc. Am. B*, vol. 7, no. 5, pp. 776–784, 1990.

[188] M. Houe and P. D. Townsend, "An introduction to methods of periodic poling for second-harmonic generation," *J. Phys. D: Appl. Phys.*, vol. 28, no. 9, pp. 1747–1763, 1995.

[189] M. Yamada, N. Nada, M. Saitoh, and K. Watanabe, "First-order quasi-phase matched $LiNbO_3$ waveguide periodically poled by applying an external field for efficient blue second-harmonic generation," *Appl. Phys. Lett.*, vol. 62, no. 5, pp. 435–436, 1993.

[190] K. Nakamura, J. Kurz, K. Parameswaran, and M. M. Fejer, "Periodic poling of magnesium-oxide-doped lithium niobate," *J. Appl. Phys.*, vol. 91, no. 7, pp. 4528–4534, 2002.

[191] I. Shoji, T. Kondo, A. Kitamoto, M. Shirane, and R. Ito, "Absolute scale of second-order nonlinear-optical coefficients," *J. Opt. Soc. Am. B*, vol. 14, no. 9, pp. 2268–2294, 1997.

[192] D. H. Jundt, "Temperature-dependent Sellmeier equation for the index of refraction, n_e, in congruent lithium niobate," *Opt. Lett.*, vol. 22, no. 20, pp. 1553–1555, 1997.

[193] A. Bruner, D. Eger, M. B. Oron, P. Blau, and M. Katz, "Temperature-dependent Sellmeier equation for the refractive index of stoichiometric lithium tantalate," *Opt. Lett.*, vol. 28, no. 3, pp. 194–196, 2003.

114

[194] K. Fradkin, A. Arie, A. Skliar, and G. Rosenman, "Tunable midinfrared source by difference frequency generation in bulk periodically poled KTiOPO$_4$," *Appl. Phys. Lett.*, vol. 74, no. 7, pp. 914–916, 1999.

[195] G. M. Zverev, E. A. Levchuk, V. A. Pashkov, and Y. D. Poryadin, "Laser-radiation-induced damage to the surface of lithium niobate and tantalate single crystals," *Soviet J. Quant. Electron.*, vol. 2, no. 2, p. 167, 1972.

[196] C.-L. Zhang, L.-X. Huang, W.-N. Zhou, G. Zhang, H.-D. Hou, Q.-F. Ruan, W. Lei, S.-J. Qin, F.-H. Lu, Y.-B. Zuo, H.-Y. Shen, and G.-F. Wang, "Growth of KTP crystals with high damage threshold by hydrothermal method," *J. Cryst. Growth*, vol. 292, no. 2, pp. 364–367, 2006.

[197] Y. Furukawa, S. A. Markgraf, M. Sato, H. Yoshida, T. Sasaki, H. Fujita, T. Yamanaka, and S. Nakai, "Investigation of the bulk laser damage of lithium triborate, LiB$_3$O$_5$, single crystals," *Appl. Phys. Lett.*, vol. 65, no. 12, pp. 1480–1482, 1994.

[198] T. Kasamatsu, H. Kubomura, and H. Kan, "Numerical simulation of conversion efficiency and beam quality factor in second harmonic generation with diffraction and pump depletion," *Jap. J. Appl. Phys.*, vol. 44, no. 12, pp. 8495–8497, 2005.

[199] R. G. Batchko, M. M. Fejer, R. L. Byer, D. Woll, R. Wallenstein, V. Y. Shur, and L. Erman, "Continuous-wave quasi-phase-matched generation of 60 mW at 465 nm by single-pass frequency doubling of a laser diode in backswitch-poled lithium niobate," *Opt. Lett.*, vol. 24, no. 18, pp. 1293–1295, 1999.

[200] L. Goldberg, L. E. Busse, and D. Mehuys, "High power continuous wave blue light generation in KNbO$_3$ using semiconductor amplifier seeded by a laser diode," *Appl. Phys. Lett.*, vol. 63, no. 17, pp. 2327–2329, 1993.

[201] N. A. Ansari and M. S. Zubairy, "Second-harmonic generation by a Gaussian Schell-model source," *Optics Communications*, vol. 59, no. 5–6, pp. 385–390, 1986.

[202] Y. Cai and U. Peschel, "Second-harmonic generation by an astigmatic partially coherent beam," *Opt. Expr.*, vol. 15, no. 23, pp. 15 480–15 492, 2007.

Bibliography

[203] Y. Qu and S. Singh, "Second-harmonic generation and photon bunching in multimode laser beams," *Phys. Rev. A*, vol. 47, no. 4, pp. 3259–3263, 1993.

[204] V. Pruneri, S. D. Butterworth, and D. C. Hanna, "Highly efficient green-light generation by quasi-phase-matched frequency doubling of picosecond pulses from an amplified mode-locked Nd:YLF laser," *Opt. Lett.*, vol. 21, no. 6, pp. 390–392, 1996.

[205] J. Ohya, G. Tohmon, K. Yamamoto, T. Taniuchi, and M. Kume, "Generation of picosecond blue light pulse by frequency doubling of a gain-switched GaAlAs laser diode having saturable absorber," *IEEE J. Quant. Electron.*, vol. 27, no. 8, pp. 2050–2058, 1991.

[206] T. Miyoshi, S. Masui, T. Okada, T. Yanamoto, T. Kozaki, S.-I. Nagahama, and T. Mukai, "510–515 nm InGaN-based green laser diodes on c-plane GaN substrate," *Appl. Phys. Expr.*, vol. 2, no. 6, p. 062201, 2009.

[207] C. Fiebig, A. Sahm, M. Uebernickel, G. Blume, B. Eppich, K. Paschke, and G. Erbert, "Compact second-harmonic generation laser module with 1 W optical output power at 490 nm," *Opt. Expr.*, vol. 17, no. 25, pp. 22 785–22 790, 2009.

[208] S. Nakamura, M. Senoh, S.-I. Nagahama, N. Iwasa, T. Yamada, T. Matsushita, H. Kiyoku, and Y. Sugimoto, "InGaN-based multi-quantum-well-structure laser diodes," *Japan. J. Appl. Phys.*, vol. 35, pp. L74–L76, 1996.

[209] E. Mimoun, L. De Sarlo, J.-J. Zondy, J. Dalibard, and F. Gerbier, "Sum-frequency generation of 589 nm light with near-unit efficiency," *Opt. Expr.*, vol. 16, no. 23, pp. 18 684–18 691, 2008.

[210] M. Fallahi, L. Fan, Y. Kaneda, C. Hessenius, J. Hader, H. Li, J. V. Monolney, B. Kunert, W. Stolz, S. W. Koch, M. J., and R. Bedford, "5-W yellow laser by intracavity frequency doubling of high-power vertical-external-cavity surface-emitting laser," *IEEE Phot. Technol. Lett.*, vol. 20, no. 20, pp. 1700–1702, 2008.

[211] C. Coldren, M. Larson, S. Spruytte, and J. Harris, "1200 nm GaAs-based vertical cavity lasers employing GaInNAs multiquantum well active regions," *Electron. Lett.*, vol. 36, no. 11, pp. 951–952, 2000.

116

[212] N. Tansu, J.-Y. Yeh, and L. J. Mawst, "Extremely low threshold-current-density InGaAs quantum-well lasers with emission wavelength of 1215–1233 nm," *Appl. Phys. Lett.*, vol. 82, no. 23, pp. 4038–4040, 2003.

[213] L. Fan, C. Hessenius, M. Fallahi, J. Hader, H. Li, J. V. Moloney, W. Stolz, S. W. Koch, J. T. Murray, and R. Bedford, "Highly strained InGaAs/GaAs multiwatt vertical-external-cavity surface-emitting laser emitting around 1170 nm," *Appl. Phys. Lett.*, vol. 91, p. 131114, 2007.

Innovationen mit Mikrowellen und Licht
Forschungsberichte aus dem Ferdinand-Braun-Institut
Leibniz-Institut für Höchstfrequenztechnik

Herausgeber: Prof. Dr. G. Tränkle, Prof. Dr.-Ing. W. Heinrich